The electrode-electrolyte interface in CO2 reduction and H2 evolution: a multiscale approach

Cecilio de Oliveira Monteiro, M

A

Scanning Electrochemical Microscopy (SECM):

setup, methods, and supporting information to Chapters 3 and 4

A.1 Scanning Electrochemical Microscopy (SECM) setup

SECM experiments were performed in a home-built system equipped with x-y-z stepper motors (C-863 Mercury, PI) and piezo positioners (E-665, PI). A schematic representation of the cell and the configuration of the electrodes can be seen in Fig. A.1. A glass cell (5 ml capacity) with a 0.8 mm diameter opening at the bottom is pressed against a base plate with the help of 4 screws. An O-ring (Viton) is placed between the sample and the glass to assure a good sealing. A copper plate (0.5 mm thick, MaTeck) is used to make the electrical contact to the sample. As depicted in the figure, the system is operated by two distinct potentiostat channels. All the SECM measurements reported in this work were performed using a Bio-Logic 2-channel potentiostat/galvanostat/EIS (SP-300). The sample counter electrode is a ring carefully positioned around the sample in order to assure a homogeneous electric field and the tip reference electrode is placed as close as possible to the tip. Prior to experiments the glass SECM cell and gas bubblers are cleaned by immersion in potassium permanganate solution for 24 h (1 g L^{-1} KMnO$_4$ dissolved in 0.5 M H$_2$SO$_4$) followed by immersion in dilute piranha in order to remove residues of manganese oxide and permanganate anions. The glassware is further cleaned by boiling at least five times in ultrapure water. The cell and positioning system are mounted on a steady base plate and enclosed in a Faradaic cage to minimize the noise and vibration interference in the measurements.

A.2 Capacitive approach system

The mediator-free approach of the modified gold microelectrode to the gold working electrode was performed in air by applying a 10 kHz AC voltage with an amplitude of 4 V$_{pp}$ (1.41 V$_{RMS}$) to the sample using a function generator (33210A, Keysight). The gold microelectrode was connected to a low noise current preamplifier (SR570, Stanford Research) operated at high-bandwidth with a gain of 2·10^8 V A^{-1}. The capacitive tip current was obtained using a virtual lock-in amplifier (LabView).

A.3 SECM pH sensor fabrication

Gold ultramicroelectrodes (Au-UMEs) were fabricated by sealing a gold wire (50 μm diameter, H. Drijfhout en Zoon's Edelmetaalbedrijven B.V.) in a glass capillary (0.4 mm i.d., Drummond Scientific Co.) and exposing a cross section by grinding the electrode with a silicon carbide paper (grit size 600, MaTeck). The

A

surface was prepared by polishing with a 1, 0.25 and 0.05 µm diamond suspension (MetaDi, Buehler) for 2 min. In between each polishing step the electrode was sonicated (Bandelin SONOREX RK 52H) in ultrapure water (>18.2 MΩ cm, Millipore Milli-Q) for 5 minutes and after the last step 5 minutes in ethanol followed by 15 minutes in water. After surface preparation the electrode was characterized by cyclic voltammetry in 0.1 M H_2SO_4, recorded in a one compartment cell (20 ml) using a gold wire (0.5 mm diameter, MaTeck, 99.9%) as counter electrode and a Ag/AgCl (LowProfile, Pine Research Instrumentation) reference electrode. The gold ultramicroelectrode (Au-UME) blank voltammetry shows a broad oxide peak starting at 1.0 V vs. Ag/AgCl and a sharp reduction peak in the cathodic scan. The low double layer charging current demonstrates that the electrode preparation leads to a smooth surface. This, and the surface cleanliness are very important for the subsequent functionalization of the Au-UME with a self-assembled monolayer. The Au-UMEs were modified with 4-nitrothiophenol (4-NTP, Merck, 80%) by immersion in a 1 mM 4-NTP/ethanol solution. After 20 min the electrode was thoroughly rinsed with ethanol and ultrapure water in order to remove weakly adsorbed species. The functionalized electrode was transferred back to a 0.1 M H_2SO_4 solution in order to convert the organic molecule by polarization from 0.1 to -0.25 V vs. Ag/AgCl (100 mV s^{-1}). Calibrations of the pH sensor was performed by cyclic voltammetry in 0.1 M Li_2SO_4 (Alfa Aesar, anhydrous, 99.99% metal basis) solutions saturated with different gases at various pH. The pH was adjusted by the addition of appropriate amounts of 1 M H_2SO_4 (Merck, Suprapur, 96%) or 1 M LiOH (Merck, monohydrate, 99.995% trace metals basis). The pH of the calibration solutions was determined with a glass-electrode pH meter (Lab 855, SI Analytics) calibrated with standard buffer solutions (Radiometer Analytical). The functionalized gold UME was calibrated in 0.1 M Li_2SO_4 solutions of various pH as this is the electrolyte used for the hydrogen evolution experiments shown in this work. The calibration was performed with the electrolyte saturated with either argon or hydrogen, as these are also the gases present during the experiments. The tip voltammetry can be seen in Fig. A.3 and clearly the different gases do not have any influence thereof.
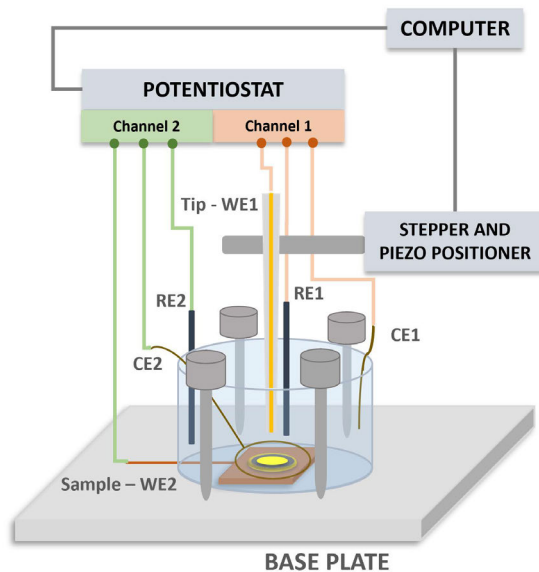
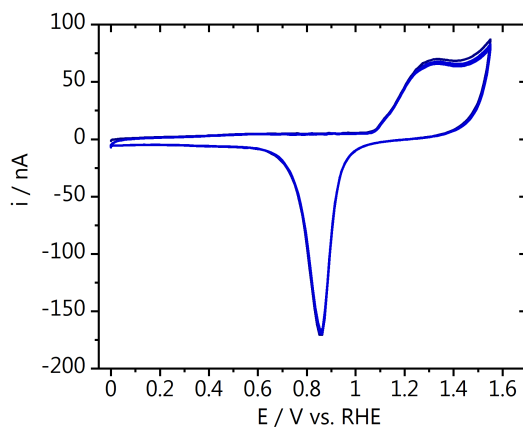**Fig. A.1.** Schematic representation of the home built SECM setup.

Fig. A.2. Blank voltammetry of the Au-UME in 0.1 M H_2SO_4 taken at 100 mV s^{-1}. The figure shows 5 subsequent cycles.

a)

b)

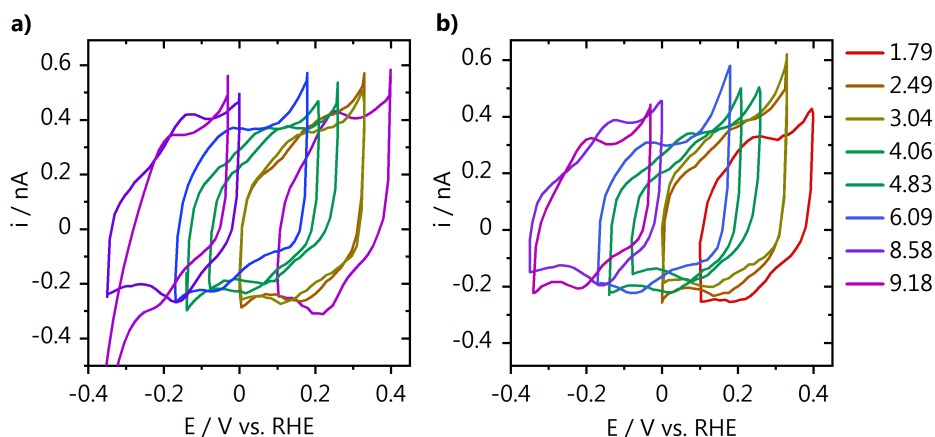|	
—	1.79
—	2.49
—	3.04
—	4.06
—	4.83
—	6.09
—	8.58
—	9.18

Fig. A.3. Calibration of the functionalized Au-UME in 0.1M Li_2SO_4 saturated with **a)** argon or **b)** hydrogen at various pH. The CVs were taken at 100 mV s^{-1}.

A.4   pH measurements

To perform the pH measurements, the SECM electrochemical cell is filled with 4 ml of electrolyte. For the measurements described in Chapter 3 and Chapter 4 the sample is a gold disc (0.5 mm thick, MaTeck, 99.995%) cleaned and polished with diamond suspension using the protocol described in Chapter 7. Two gold wires and two Ag/AgCl electrodes are used as counter and reference electrodes, respectively. Gases (argon or CO_2) are purged through and above the solution throughout the whole experiment to avoid oxygen diffusion into the electrolyte. Measurements are performed with the pH sensor at a constant distance from the surface and the tip voltammetry is constantly recorded at a scan rate of 200 mV s^{-1} (5 seconds per cycle) while the sample potential is varied.

A.5   Local pH during hydrogen evolution (Chapter 3)

The sample chronoamperometry is recorded and can be seen in Fig. A.4. Initially the sample is held at 0 V vs. Ag/AgCl and subsequently different negative potentials where hydrogen evolution is taking place are applied. In between measurements the sample potential is again set to 0 V for long enough that the measured pH is equal to the bulk pH, demonstrating the recovery of the diffusion
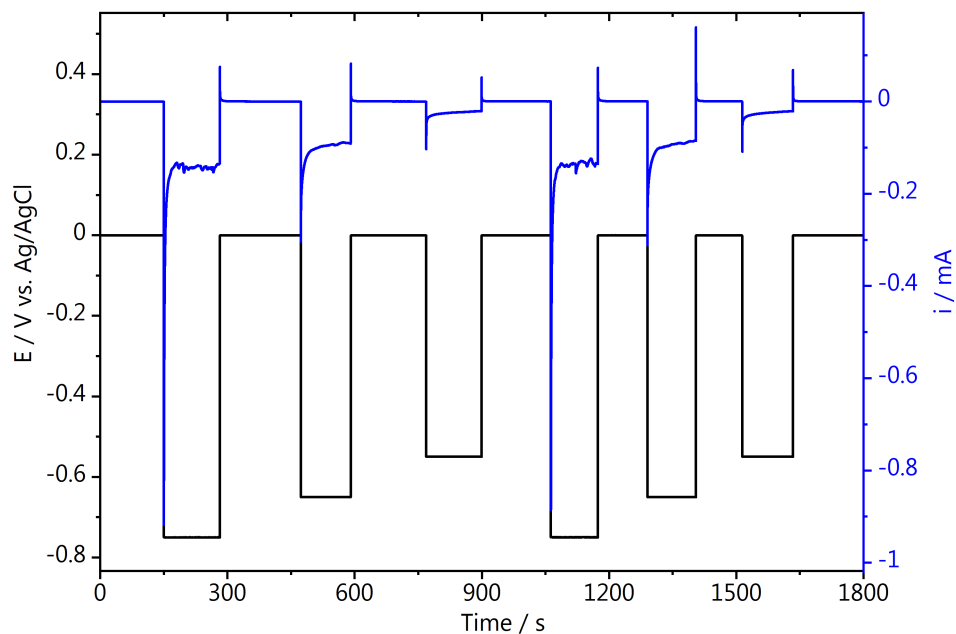
Fig. A.4. Chronoamperometry recorded at the gold sample during the pH measurements (0.1 M Li$_2$SO$_4$, pH = 3.2).
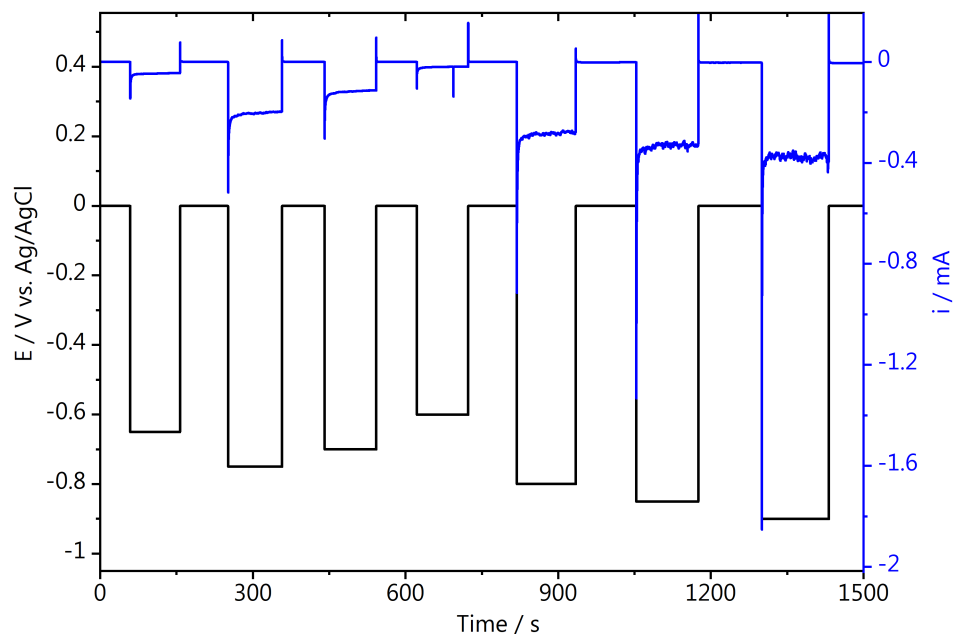

Fig. A.5. Chronoamperometry recorded at the gold sample during the pH measurements (0.1 M Li$_2$SO$_4$, pH = 3).

layer gradient. A second set of experiments was performed changing the sample potential in smaller steps to show not only the sensitivity of the pH sensor but also that it can be used in a wide pH range. The chronoamperometry can be found in Fig. A.5.

A.6 Data processing from pH measurements

The pH probe is positioned at a constant distance from the surface with the sample potential held at 0 V vs. Ag/AgCl. In Chapter 3 for example, hydrogen evolution reaction (HER) is turned "on" and "off" at the substrate and the tip voltammetry is measured in time. An example of the peak shift monitored at the tip can be found in Fig. A.6, for HER turned "on" at the sample at –0.75 V vs. Ag/AgCl. The data processing is performed by fitting the tip voltammetry with a Gaussian function with a linear background (Eq. A.1) to extract the anodic mid-peak position. The fitted data for –0.75 , –0.65 and –0.55 V vs. Ag/AgCl (two runs) can be found in Fig. A.7.

$$f(x) = y_0 + a_1 * x + a_2 * exp(-((x - x_0)/width)^2) \qquad \text{Eq. A.1}$$

The mid-peak potential for each cycle was obtained by fitting the tip voltammetry (see SI) and converted to pH using the calibration curve.
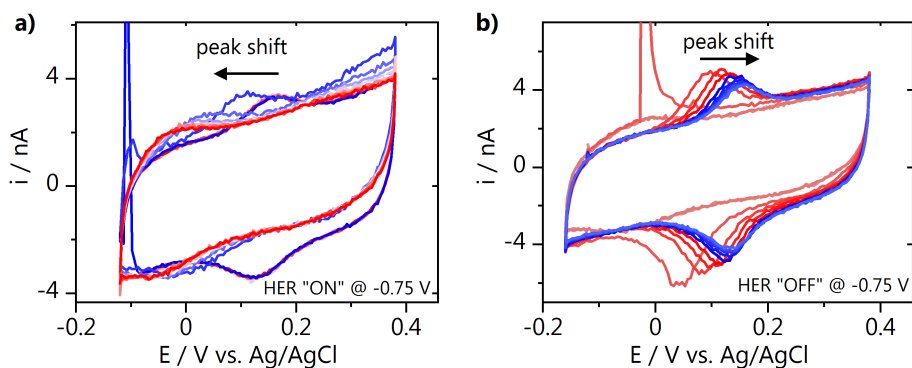

Fig. A.6. Mid-peak potential shift of the pH probe when hydrogen evolution is turned **a)**"on" and **b)**"off" at the gold sample at –0.75 V vs. Ag/AgCl.
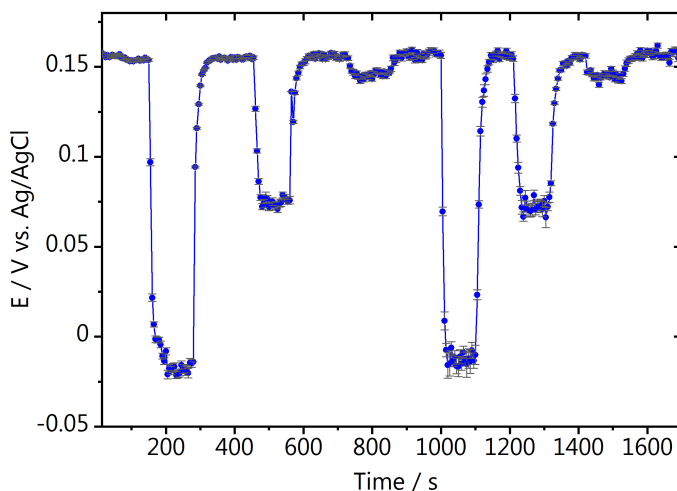
Fig. A.7. Data points obtained by fitting the tip voltammetry.

A.7 Finite Element Method (FEM) simulation methods (Chapter 4)

The experimental system from Chapter 4 is represented by a 2D axisymmetric cylindrical SECM tip and a planar working electrode at the bottom of a cylindrical cell. Geometric parameters[1] are listed in Table A.1 with a graphical depiction of the geometry in Fig. A.8.

Table A.1. Geometric parameters

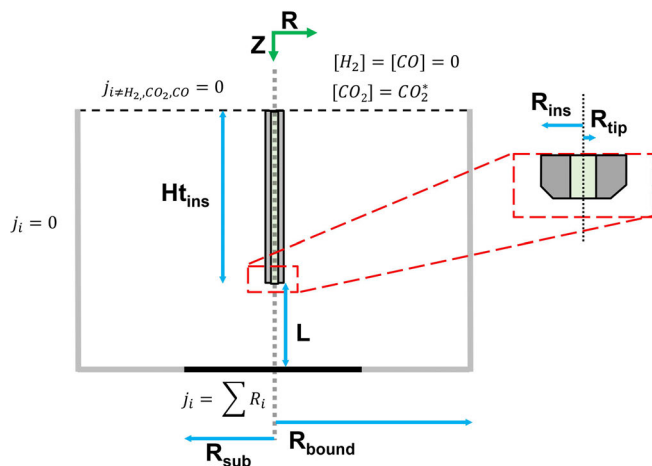| Parameter	Value
Tip Radius (R_{tip}, μm)	25
Insulation Radius (R_{ins}, μm)	500
Working Electrode Radius (R_{sub}, mm)	5
Boundary Radius (R_{bound}, mm)	8
Normalized tip-surface separation (L)	3.4
Tip electrode height (h_{ins}, mm)	7.4

Fig. A.8. Geometric description of the experimental system with simulation boundary conditions used for hydrogen evolution and CO_2 reduction.

Migration is neglected and transport is governed by Fick´s second law of diffusion. Proton-hydroxide ion recombination is included as a homogeneous reaction along with the carbon dioxide reversible reactions (Eq. 4.4-4.7 in Chapter 4). The governing equations are:
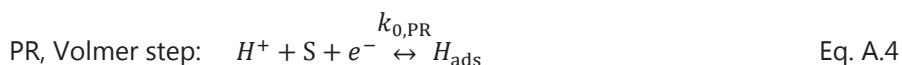
$$\frac{dC_i}{dt} = D_i \nabla^2 C_i + \sum R_{ij} \qquad \text{Eq. A.2}$$

where C_i is the concentration of each species in solution (H$^+$, OH$^-$, H$_2$O, H$_2$, Li$^+$, and SO$_4^{2-}$), D_i is the species diffusion coefficient, and the reversible reaction rates, R_{ij}, for each species, i, are summed for each reversible reaction , j.
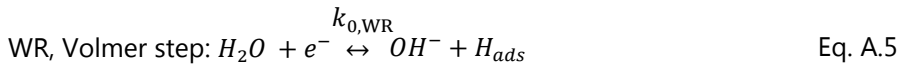
The boundary conditions, visually represented in Fig. A.8, are as follows: at the WE surface ($z = 0$), a flux balance is applied using the electrode reaction:

$$-D\nabla C_i \cdot \bar{n} = \sum_j r_{ij} \qquad \text{Eq. A.3}$$

where $\bar{n}$ is the surface normal. The summation is over all surface reactions, j, and r_{ij} is the rate of production of species i due to reaction j; $\sum r_{ij}$ is the summation of the reactions involving a given species, i. Proton reduction (PR), water reduction (WR) and carbon dioxide reduction (CO$_2$RR, Eq. A.6) are considered at the substrate. Proton reduction and water reduction rates are assumed to be limited by Volmer adsorption of hydrogen (Eq. A.4 and A.5, respectively, E_{app} is an arbitrary reference potential for the first reaction step).[2,3]

PR, Volmer step: $\quad H^+ + S + e^- \overset{k_{0,\text{PR}}}{\leftrightarrow} H_{\text{ads}} \qquad$ Eq. A.4

$$E_{app} = 0\,V\ vs.\ SHE\ at\ pH = 0$$

$$\text{WR, Volmer step: } H_2O + e^- \overset{k_{0,\text{WR}}}{\leftrightarrow} OH^- + H_{ads} \qquad\qquad \text{Eq. A.5}$$

$$E_{app} = 0\,V\ vs\ SHE\ at\ pH = 0$$

$$\text{CO}_2\text{RR: } CO_2 + H_2O + 2e^- \overset{k_{0,\text{CO}_2\text{R}}}{\leftrightarrow} 2OH^- + CO \qquad\qquad \text{Eq. A.6}$$
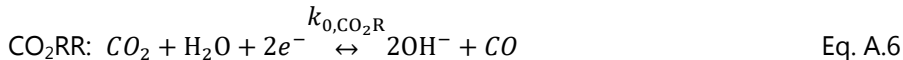
$$E_0 = -0.52\,V\ vs\ SHE$$

The rates of PR and WR, due to the large overpotentials, were expressed by Tafel kinetics. CO_2RR was expressed in Butler-Volmer form:

$$r_{\text{PR}} = k_{0,\text{PR}}(C_{H^+}\exp(-\alpha_{\text{PR}}n_{\text{PR}}f\eta_{\text{PR}})) \qquad\qquad \text{Eq. A.7}$$

$$r_{\text{WR}} = k_{0,\text{WR}}\big(C_{H_2O}\exp(-\alpha_{\text{WR}}n_{\text{WR}}f\eta_{\text{WR}})\big) \qquad\qquad \text{Eq. A.8}$$

$$r_{\text{CO}_2\text{RR}} = k_{0,\text{CO}_2\text{RR}}\Big(C_{CO_2RR}C_{H^+}^2\exp(-\alpha_{\text{CO}_2\text{RR}}n_{\text{CO}_2\text{RR}}f\eta_{\text{CO}_2\text{RR}}) - $$
$$C_{H_2O}C_{CO}\exp\big((1-\alpha_{\text{CO}_2\text{RR}})n_{\text{CO}_2\text{RR}}f\eta_{\text{CO}_2\text{RR}}\big)\Big) \qquad\qquad \text{Eq. A.9}$$

where $k_{0,j}$ are the rate constants, the number of electrons is n_j, the charge transfer coefficient is α_j, and $\eta_j = E - E_{0,j}$, where the $E_{0,j}$ are the formal potentials are and E is the applied surface potential. Finally, $f = \frac{F}{RT}$, where F is Faraday's constant, R is the gas constant and T is the temperature.

Three surface reactions occur simultaneously at the gold surface electrode. At the liquid-atmosphere boundary($z = L + ht_{ins}$), the concentration of molecular hydrogen, H_2, is zero (Fig. A.8), the bulk concentration of CO_2 is set to 0 (under Ar) or 10 mM (under CO_2), and flux is set to zero for all other species. This bulk CO_2 concentration, which is roughly half of the estimated saturation concentration (23 mM, for 1 atm CO_2 in 0.1 M Li_2SO_4 at pH 3 and 25 °C), is set to avoid numerical convergence issues encountered at higher concentrations. At all other boundaries, a zero-flux condition is imposed for all species. Diffusivities used in the simulation are listed in Table A.3 with the equilibrium and dissociation constants for the reversible reactions. Kinetic rate constants for the homogeneous dissociation reactions were obtained from Wuttig et al.[4] and Bohra et al.[5] The tip electrode proton adsorption is assumed to have negligible effects on the pH.

A.8 pH measurements during HER and CO_2 reduction (Chapter 4)
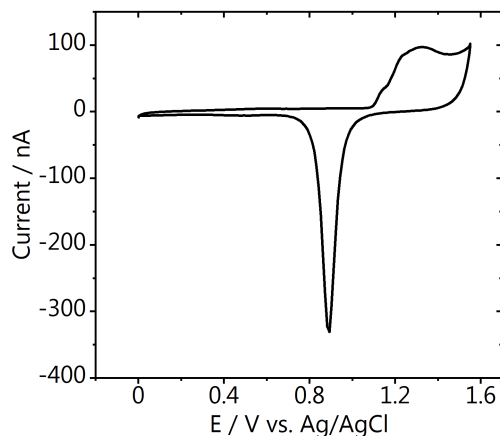
A.8.1 Calibration functionalized Au-UME in CO_2 atmosphere

Fig. A.9. Blank voltammetry of the Au-UME used for the pH measurements taken in argon saturated 0.1 M H_2SO_4 at 50 mV s^{-1}.
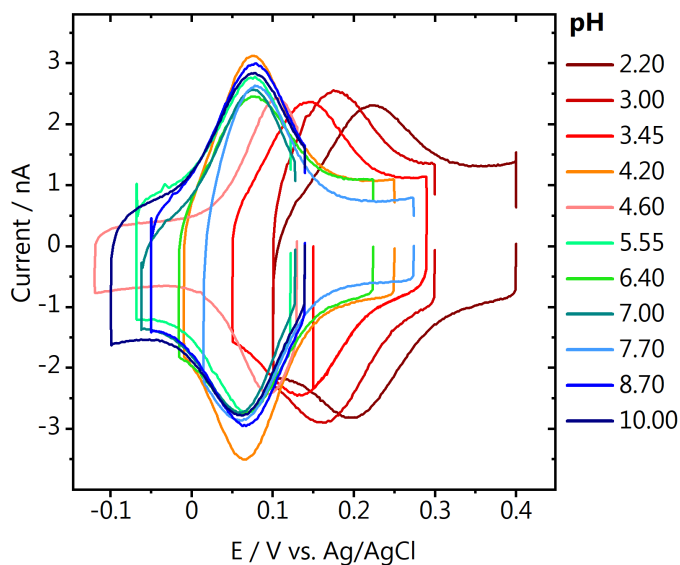

Fig. A.10. Voltammetric response of the Au-UME functionalized with the 4-HATP/4-NSTP redox couple in 0.1 M Li_2SO_4 solutions of different bulk pH after saturation with CO_2 for 5 minutes.
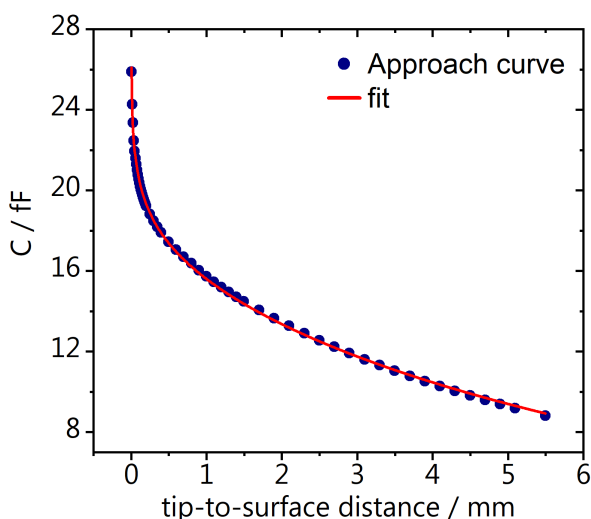
A.8.2 Capacitive approach curve

Fig. A.11. Capacitive approach curve recorded before the pH measurements, in order to define the surface position.

A.8.3 pH measurements

SECM pH measurements were performed in 0.1 M Li_2SO_4, pH = 3. The sample potential was stepped from –0.5 to –0.9 V vs. Ag/AgCl in 50 mV steps. Chronoamperometry at the sample was carried out for about 3 minutes at each potential while the pH was measured with the tip. The pH response as a function of potential shown in Fig. 4.3 in Chapter 4 is summarized in the figure below, where each value displayed is the pH measured after 100 seconds of chronoamperometry at the sample.

A
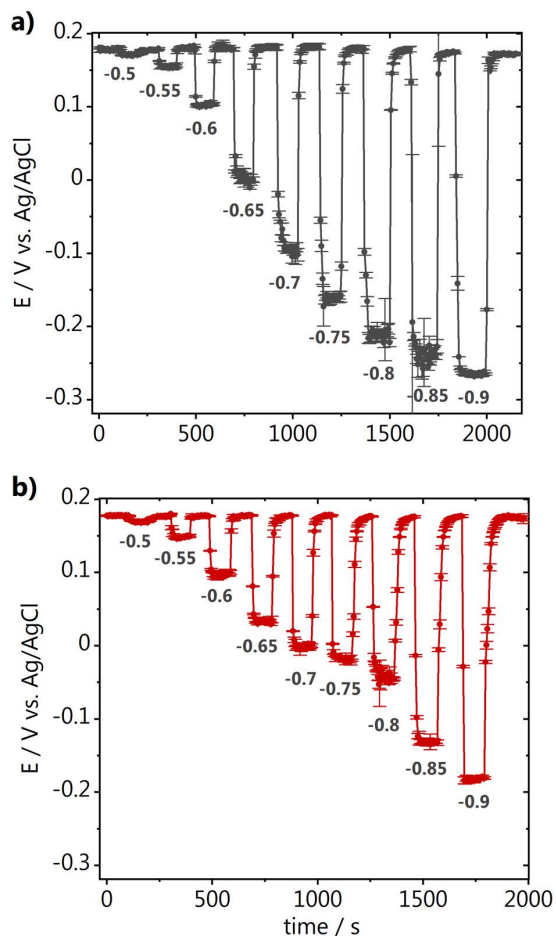
Fig. A.12. Mid-peak potential obtained by fitting the voltammetry of the 4-HATP/4-NSTP functionalized Au-UME recorded while the sample potential was stepped in 0.1 M Li_2SO_4 either in **a)** argon or **b)** CO_2 atmosphere. The sample potentials are indicated below the curves, in V vs. Ag/AgCl.
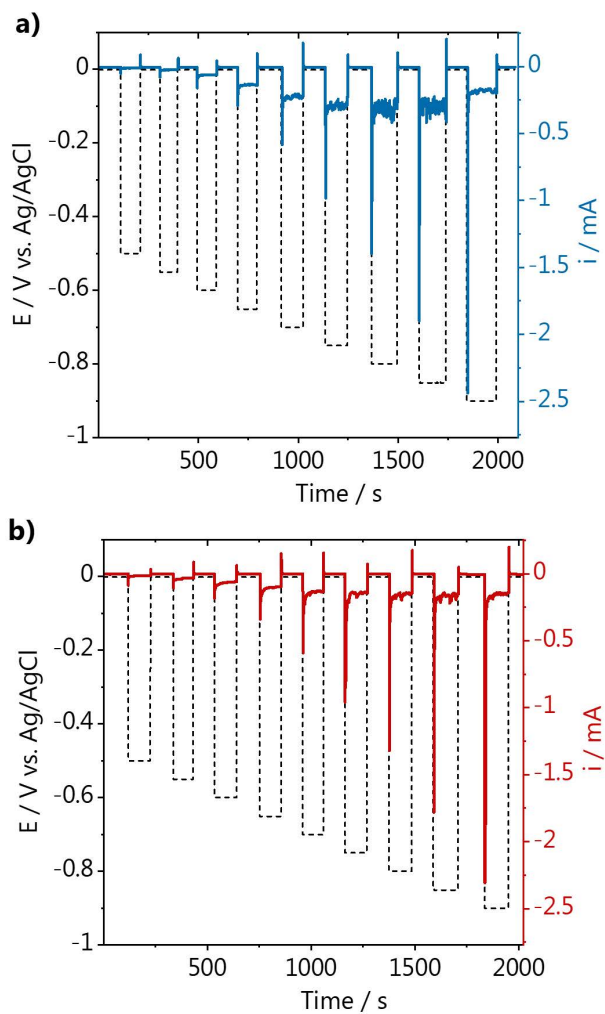
Fig. A.13. Chronoamperometry recorded at the polycrystalline gold sample in **a)** argon and **b)** CO_2 atmosphere in 0.1 M Li_2SO_4, pH 3.
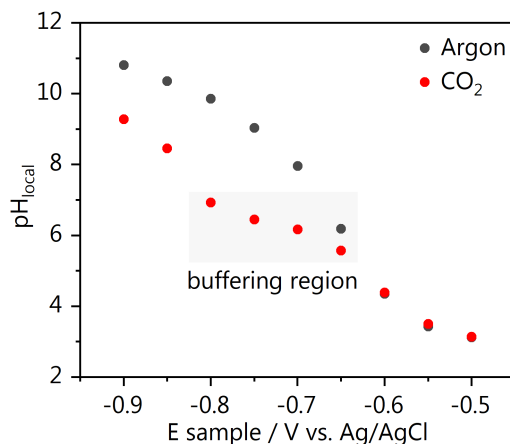
Fig. A.14. Comparison of the pH measured at the same distance from the surface in argon and CO_2 atmosphere. Values taken from Fig. 4.3 in the main text, after each potential was applied for 100 s.

A.9 Finite Element Method (FEM) simulation

Simulations were completed using COMSOL Multiphysics with transport of dilute species. A triangular mesh was used with an increased resolution surrounding the surface and tip electrodes. All species were included in the simulation and the properties defined below were used to describe the transport and reactivity of each species.

A.9.1 Hydrogen evolution reaction kinetics

The hydrogen evolution reaction is simulated by solving Eq. A.2 and A.3 shown in Section A.8. The use of Eq. A.7 to calculate initial proton reduction kinetic rate parameters is justified by the Tafel slope of 147 mV dec^{-1} (Fig. A.15), indicating that a Volmer or large overpotential Heyrovsky steps are likely the rate limiting step.[2] When the reduction reaction is largely irreversible, the Heyrovsky response approaches that of the Volmer. Initial guesses of α_p and $k_{0,PR}$ were determined from the Tafel plot (see Fig. A.15) and $E_0 = 0$ V vs. SHE at pH = 0. Subsequently, kinetic parameters for proton reduction (PR) appearing in Eq. A.7 in the main text, were obtained from fitting to cyclic voltammetric data, specifically the reductive peak of the third cathodic sweep under argon (Fig. A.16) over a potential range from 0 to 0.9 V vs. Ag/AgCl. We expect this CV current to be mainly due to proton reduction

251

and not water reduction, because of the fast potential sweep rate (100 mV s^{-1}) and low bulk pH. During a CV cycle, the surface pH remains below 6.5, supporting this
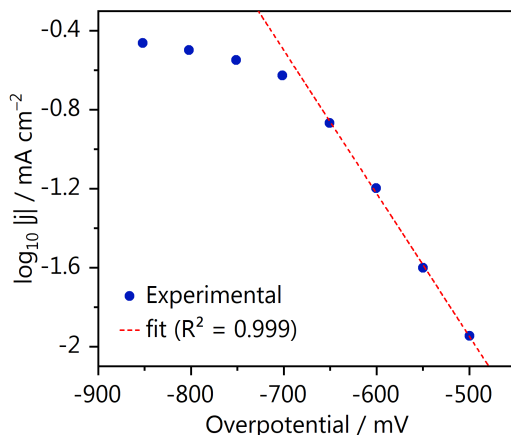

Fig. A.15. Tafel slope for HER at pH 3 extracted from the chronoamperometry (Fig. A.13a) experiment.
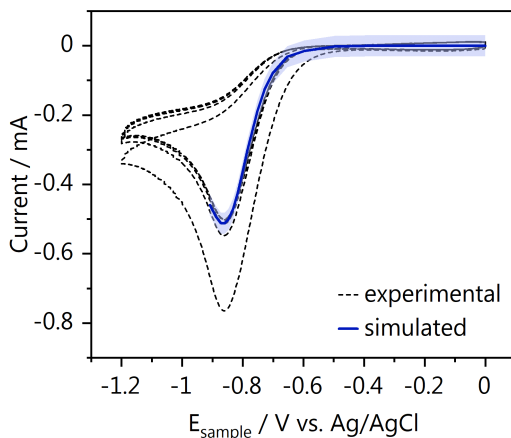

Fig. A.16. Cyclic voltammogram of proton and water reduction in argon. Experimental results (black) are compared to FEM simulation results (blue line) with a 95% confidence interval.

A

Table A.2. Kinetic parameters estimated by fit to the Tafel plot (Fig. A.15), the cyclic voltammogram (Fig. A.16), or the pH-V relation (see Fig. 4.6a in Chapter 4). Values that were fixed and not fitted are marked with a star (*).

Parameter	Tafel (Fig. A.15)	CV fit (Fig.A.16)	pH-V fit (Fig. A.14)	Literature	Ref.
$k_{0,PR}$ [cm/s]	4.2E-8 ± 1.8E-8	3.8E-8 ± 1.8E-8	-	1E-6–1E-10	6–9
α_{PR}	0.41 ± 0.01	0.43 ± 0.03	-	-	-
n_{PR}	-	1.3 ± 0.01	-	-	-
$E_{0,PR}$ [V vs. SHE]	0*	0*	0*		
D_{H^+} [cm²/s]	-	1.4E-5 ± 5.5E-6	-	9.3E-5	4
$k_{0,WR}$ [cm/s]	-	-	3E-14±2E-14	-	-
α_{WR}	-	-	0.5*		
n_{WR}	-	-	1*		
$E_{0,PR}$ [V vs. SHE]	-	-	0*		
D_{OH^-} [cm²/s]	-	-	5.3E-5*		10
R^2	0.999	0.993	0.976	-	-

assumption. The resulting parameters for α_P, $k_{0,PR}$, D_{H^+} and n_P are listed in Table A.2, where the calculated charge transfer coefficient ($\alpha_p = 0.41$) agrees with the result obtained from the Tafel slope in Fig. A.15.

After having fit the cyclic voltammogram, the rate constant for the water reduction reaction, $k_{0,WR}$, described by Eq. A.8 was obtained by fitting the pH–voltage relation shown in Fig. 4.6 of Chapter 4. All other parameters appearing in Eq. A.8, were set to the values given in Table A.3. For comparison to experiment, the pH values were averaged over the SECM electrode area. During the optimization of $k_{0,WR}$, the parameters obtained for the hydrogen evolution reaction were kept constant. As the pH response is largely dominated by the water reduction reaction at potentials more negative than –0.65 V vs. Ag/AgCl (Fig. A.17), keeping the hydrogen evolution reaction parameters fixed, is a reasonable approach. Because of this, only the water reduction rate constant ($k_{0,w} = 3E–14 ± 2E–14$ cm s⁻¹) was fit for this data set. With an R^2 value of 0.976, the simulation results shown in Fig. 4.6a of Chapter 4 match reasonably well with the experimental results, except at the potential of –0.65 V vs. Ag/AgCl, where the simulation underestimates the pH change. The water reduction current at the portion of the surface electrode directly below the surface (r = 0 – R_{tip}, z = 0) reaches a local maximum at –0.65 V vs. RHE due to the large pH increase (OH⁻ accumulation) directly below the tip. This

hydroxide accumulation drives a decrease in the water reduction rate directly below the SECM tip.
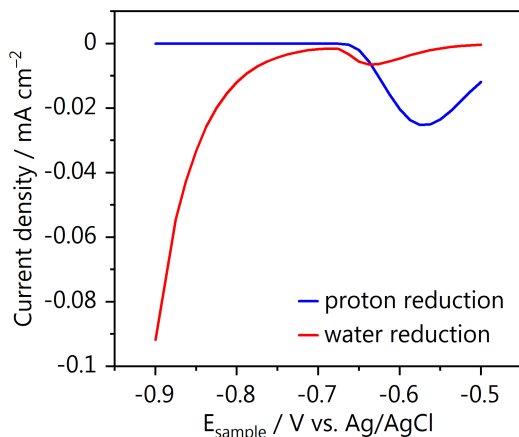
Fig. A.17. Calculated contributions of the local chronoamperometric current density at the gold electrode and beneath the SECM tip, due to proton (blue) and water (red) reduction. Current density is calculated from average flux of each species over 25 μm (R_{Tip}) from the center of the surface electrode, which is below the SECM tip electrode.

Fig. A.18. Vertical concentration profiles during HER in the absence of CO_2 for H^+ (solid) and OH^- (dashed) as the boundary layer approaches the tip position (dotted grey line). Surface electrode potentials of –0.850 V (blue) and –0.8625 V (red) vs. Ag/AgCl are shown.

A

A.9.2 CO$_2$ reduction reaction kinetics

The electrochemical reduction of CO$_2$ is described by Eq. A.9. The relevant parameters, which are listed in Table A.2, are either set to the theoretical values or taken f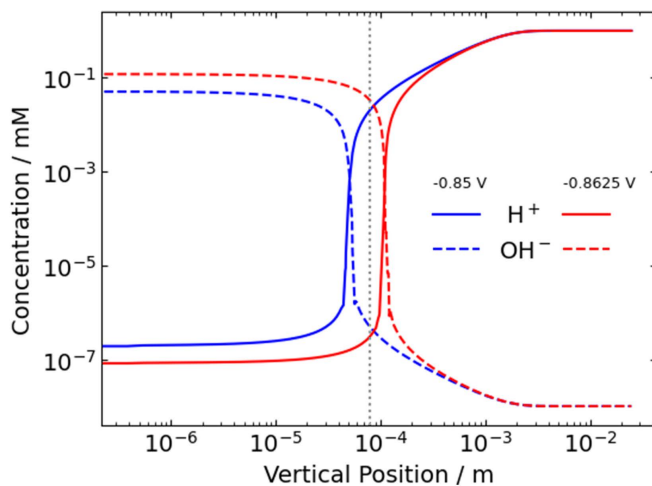rom literature. Homogeneous reactions are represented by the below rate laws (Eq. A10-A16). The values for the equilibrium, K_i, and dissociation rate constants, k_{-i}, are listed in table A.3.

$$-r_{s1*H_2O} = K_1 * k_{-1}C_{CO_2}C_{H_2O} - k_{-1}C_{H_2CO_3}$$ Eq. A.10

$$-r_{s2*H_2CO_3} = K_2 * k_{-2}C_{H_2CO_3} - k_{-2}C_{HCO_3^-}C_{H^+}$$ Eq. A.11

$$-r_{s3*OH^-} = K_3 * k_{-3}C_{CO_2}C_{OH^-} - k_{-3}C_{HCO_3^-}$$ Eq. A.12

$$-r_{s4*OH^-} = K_4 * k_{-4}C_{HCO_3^-}C_{OH^-} - k_{-4}C_{CO_3^{2-}}$$ Eq. A.13

$$-r_{s5*H^+} = K_5 * k_{-5}C_{H^+}C_{OH^-} - k_{-5}C_{H_2O}$$ Eq. A.14

$$-r_{s6*HCO_3^-} = K_6 * k_{-6}C_{HCO_3^-} - k_{-6}C_{CO_3^{2-}}C_{H^+}$$ Eq. A.15

$$-r_{s7*H_2O} = K_7 * k_{-7}C_{CO_2}C_{H_2O} - k_{-7}C_{H=}C_{HCO_3^-}$$ Eq. A.16

Table A.3. FEM system parameters. Values for proton reduction and water reduction are given in Table A.2.

Variable	Value	Reference
D_{H_2} , cm^2 s^{-1}	5.5E-5	[11]
D_{H_2O} , cm^2 s^{-1}	2.2E-5	[12]
D_{Li^+} , cm^2 s^{-1}	1.0E-5	[13]
$D_{SO_4^{2-}}$, cm^2 s^{-1}	2.0E-5	[11]
*D_{H^+} , cm^2 s^{-1}	9.3E-5	[4]
D_{OH^-} , cm^2 s^{-1}	5.3E-5	[10]
$D_{HSO_4^-}$, cm^2 s^{-1}	2.3E-5	[4]
D_{CO_2} , cm^2 s^{-1}	1.7E-5	[4]
D_{CO} , cm^2 s^{-1}	1.6E-5	[4]
$D_{HCO_3^-}$, cm^2 s^{-1}	1.0E-5	[4]
$D_{CO_3^{2-}}$, cm^2 s^{-1}	8.0E-6	[4]
$D_{H_2CO_3}$, cm^2 s^{-1}	3.5E-5	[4]
K_1	2.6E-3	[4,14,15]
k_{-1} , s^{-1}	2E4	[4]
K_2 , M	1.7E-4	[4,14]

k_{-2} , M^{-1} s^{-1}	1E12	[4]
K_3 , M^{-1}	4E7	[5,14,15]
k_{-3} , s^{-1}	5E-5	[5]
K_4 , M^{-1}	1.7E3	[5,15]
k_{-4} , M^{-1} s^{-1}	1E6	[5]
K_5 , M^2	1E-14	[5,16]
k_{-5} , M^{-1} s^{-1}	2E9	[5,16]
K_6 , M	5E-11	[4,5,16]
k_{-6} , M^{-1} s^{-1}	1E12	[4,16,17]
K_7 , M	4.4E-7	[15,16]
k_{-7} , M^{-1} s^{-1}	9E4	[15]
k_{0,CO_2RR}	1E-15	
α_{CO_2RR}	0.5	
n_{CO_2RR}	2	
E_{0,CO_2R} [V vs. SHE]	−0.52	

*see Table A.2 for fitted value used in FEM simulations

References

(1)   Monteiro, M. C. O.; Jacobse, L.; Touzalin, T.; Koper, M. T. M. *Anal. Chem.* 2020, *92* (2), 2237–2243.
(2)   Shinagawa, T.; Garcia-Esparza, A. T.; Takanabe, K. *Sci. Rep.* 2015, *5* (1), 13801.
(3)   Carneiro-Neto, E. B.; Lopes, M. C.; Pereira, E. C. *J. Electroanal. Chem.* 2016, *765*, 92–99.
(4)   Wuttig, A.; Yoon, Y.; Ryu, J.; Surendranath, Y. *J. Am. Chem. Soc.* 2017, *139* (47), 17109–17113.
(5)   Bohra, D.; Chaudhry, J. H.; Burdyny, T.; Pidko, E. A.; Smith, W. A. *Energy Environ. Sci.* 2019, *12* (11), 3380–3389.
(6)   Hamelin, A.; Weaver, M. J. *J. Electroanal. Chem. Interfacial Electrochem.* 1987, *223* (1), 171–184.
(7)   Brug, G. J.; Sluyters-Rehbach, M.; Sluyters, J. H.; Hemelin, A. *J. Electroanal. Chem. Interfacial Electrochem.* 1984, *181* (1), 245–266.
(8)   Perez, J.; Gonzalez, E. R.; Villullas, H. M. *J. Phys. Chem. B* 1998, *102* (52), 10931–10935.
(9)   Dubouis, N.; Grimaud, A. *Chem. Sci.* 2019, *10* (40), 9165–9181.
(10)   Lee, S. H.; Rasaiah, J. C. *J. Chem. Phys.* 2011, *135* (12), 124505.
(11)   Green, D. W.; Perry, R. H. 8th ed.; McGraw Hill Professional, 2007.
(12)   Mills, R. *J. Phys. Chem.* 1973, *77* (5), 685–688.
(13)   Banerjee, P.; Bagchi, B. *J. Chem. Phys.* 2019, *150* (19), 190901.
(14)   Keene, R. F.; Sullivan, B. P.; Krist, K.; Guard, H. E. 1st ed.; Elsevier, 1993.
(15)   Gupta, N.; Gattrell, M.; MacDougall, B. *J. Appl. Electrochem.* 2006, *36* (2), 161–172.
(16)   Singh, M. R.; Goodpaster, J. D.; Weber, A. Z.; Head-Gordon, M.; Bell, A. T. *Proc. Natl. Acad. Sci.* 2017, *114* (42), E8812--E8821.
(17)   Schulz, K. G.; Riebesell, U.; Rost, B.; Thoms, S.; Zeebe, R. E. *Mar. Chem.* 2006, *100* (1–2), 53–65.
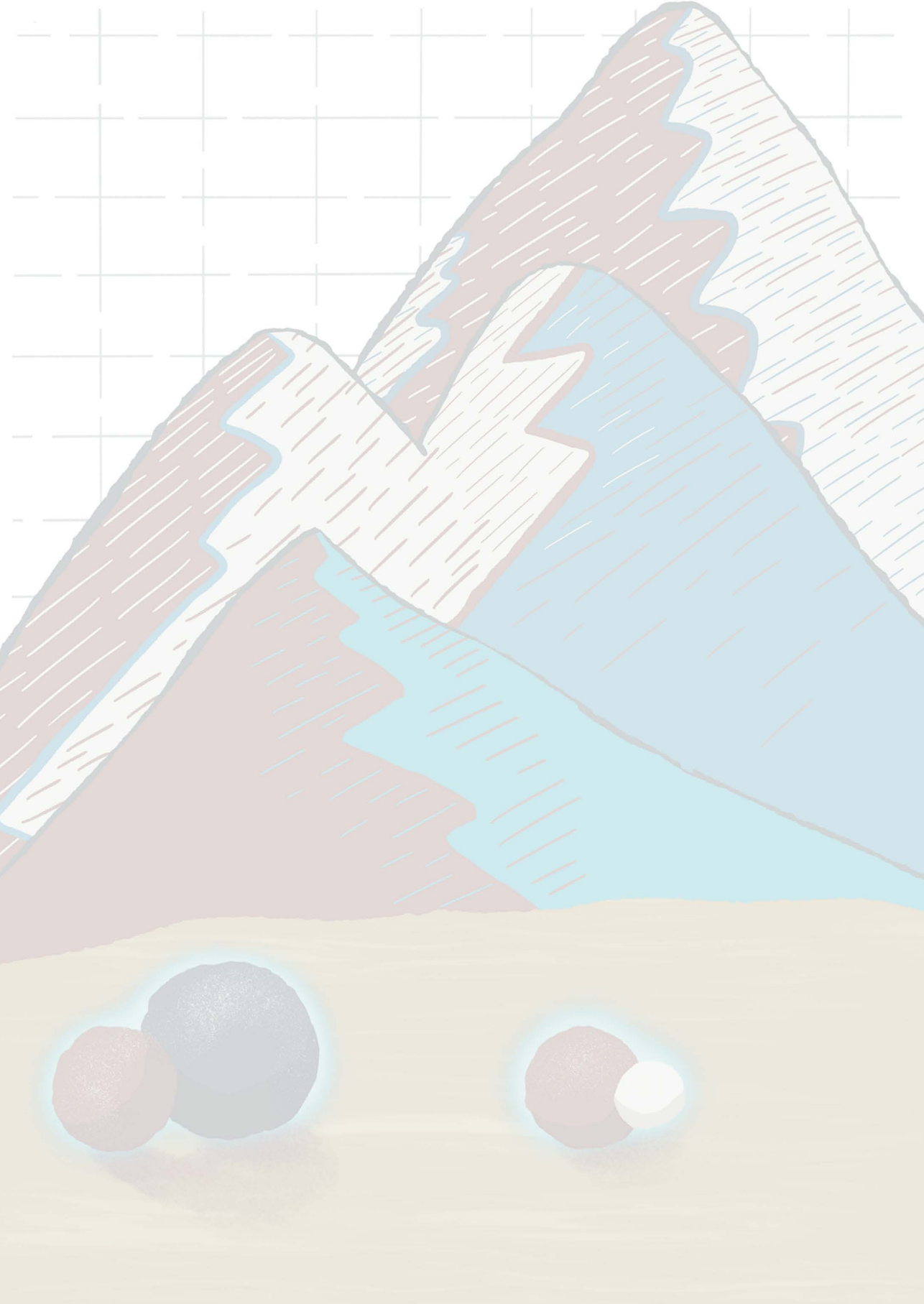
B

Methods and supporting information to Chapter 5

B.1 Microelectrode and pH sensor fabrication

The platinum ultramicroelectrode (Pt-UME) was made by etching and sealing a platinum wire (50 μm diameter, Goodfellow, 99.99%) into a soda lime glass capillary using a butane torch. Details can be found elsewhere.[1] The gold ultramicroelectrode (Au-UME) was fabricated also by sealing a gold wire (50 μm diameter, H. Drijfhout en Zoon's Edelmetaalbedrijven B.V.) in a soda lime glass capillary, however without the etching step. A cross section of the wires was exposed by grinding the UMEs with a silicon carbide paper (grit size 600, MaTeck). The surface preparation was done by polishing with a 1, 0.25 and 0.05 μm diamond suspension (MetaDi, Buehler) for 2 min. To remove as much as possible polishing particle residues, the electrode was sonicated (Bandelin SONOREX RK 52H) in ultrapure water (>18.2 MΩ cm, Millipore Milli-Q) for 5 minutes in between each polishing step and after the last step sonicated for 5 minutes in ethanol and 15 minutes in water. The resulting Pt-UME and Au-UME used in Chapter 5 have a radius of approximately 6.5 ± 0.07 μm and 26.9 ± 0.05 μm, respectively, determined with the $Fe(CN)_6^{3-}/Fe(CN)_6^{4-}$ outer sphere reaction. Prior to experiments, the Pt-UME was cycled 200 times between 0.06 and 1.60 V vs. RHE in 0.1 M H_2SO_4 (Merck, Suprapur, 96%) at 1 V s^{-1}, yielding a reproducible blank voltammogram. The Au-UME was also characterized by cyclic voltammetry in 0.1 M H_2SO_4, to assure that there is no leakage between the wire and the sealing. The blank voltammetry of the Pt and Au UMEs and the voltammetry in $Fe(CN)_6^{3-}/Fe(CN)_6^{4-}$ can be found in Fig. B.1. The Au-UME pH sensor synthesis is done as described in Chapter 3 and Appendix A.

B.2 Scanning Electrochemical Microscopy (SECM) methods

SECM experiments were carried out in our home-built SECM setup, which was described in detail in Appendix A.[2] All the equipment and cleaning procedures used here, are exactly the same as also reported in Appendix A. The sample used is a gold disc (0.5 mm thick, MaTeck, 99.995%) cleaned and polished with diamond suspension using the protocol described in Chapter 7 and Appendix D.[3] Measurements were performed in 5 ml of 0.1 M Cs_2SO_4 (Alfa Aesar, Puratronic™, 99.997%, metals basis) which was constantly purged with CO_2. The electrolyte choice was made based on the high activity for CO_2 reduction achieved in Cs^+ containing electrolytes. Measurements were performed at a constant distance from the surface and the tip voltammetry was constantly recorded at a scan rate of 200 mV s^{-1} while the sample potential was varied.

B.3   RDE methods

RDE experiments were performed using a MSR Electrode Rotator (Pine Research Instrumentation) equipped with an AFE6M shaft. The RDE measurements were carried out in a three-electrode glass cell in which the reference was a reversible hydrogen electrode (RHE) separated from the work compartment by a Luggin capillary. The working electrode was a polycrystalline platinum disc (5.0 mm OD x 4.0 mm thick, Pine Research and Instrumentation) and the counter electrode a platinum mesh. Prior to experiments, the Pt working electrode was cycled 200 times between 0.06 and 1.65 V vs. RHE in 0.1 M H_2SO_4 (Merck, Suprapur, 96%) at 1 V s^{-1}, yielding a reproducible blank voltammogram. Measurements were performed in 50 ml of 0.1 M Cs_2SO_4 (Alfa Aesar, Puratronic™, 99.997%, metals basis) while constantly saturating the electrolyte with CO. To change the OH^- concentration, appropriate amounts of KOH (Alfa Aesar, 99.99%, metals basis) were added and the pH of the CO saturated solution was determined using a glass-electrode pH meter (Lab 855, SI Analytics) calibrated with standard buffer solutions (Radiometer Analytical).

B.4   Characterization of the ultramicroelectrodes

Characterization of the platinum and gold ultramicroelectrodes (UMEs) was performed before the SECM experiments. The blank voltammetry can be seen in Fig. B.1 below, together with the voltammetry of the outer sphere reaction $Fe(CN)_6^{3-}$/$Fe(CN)_6^{4-}$. The diffusion limiting currents from Fig. B.1b and d were used to calculate the radius of the platinum and gold UMEs, respectively, using Eq. B.1:

$$r_{UME} = i_{lim}/4nFDc \hspace{3cm} \text{Eq. B.1}$$

where i_{lim} is the diffusion limited current in A, n is the number of electrons transferred, F is the Faraday constant in s A mol^{-1}, D is the diffusion coefficient of $Fe(CN)_6^{3-}$ in cm^2 s^{-1} and c is the concentration in mol cm^{-3}.

B.5   Capacitive approach

The tip-to-surface distance was determined by performing a capacitive approach[2,4] in air before all SECM measurements as described in Appendix A. The absolute surface position is determined by fitting the approach curve with Eq. B.2.
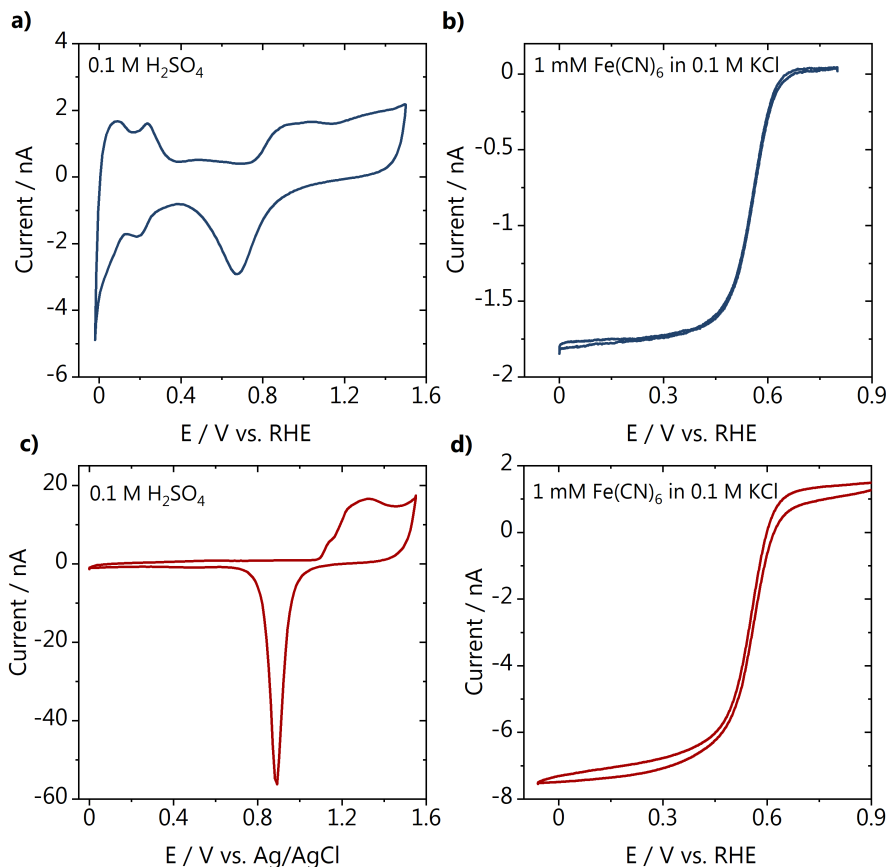
Fig. B.1. Blank voltammetry of **a)** the Pt-UME and **c)** the Au-UME taken in 0.1 M H$_2$SO$_4$ at 200 mV s^{-1}. Voltammetry of the outer sphere reaction recorded in argon saturated K$_3$Fe(CN)$_6{}^3$ + 0.1 M KCl at 10 mV s^{-1} with the **b)** Pt-UME and **d)** Au-UME.

$$C_{tot}(Z) = -A_1 * \ln(d_0 - Z) + B + \left(\frac{A_2}{L_{par} + d_0 - Z} \right)$$
Eq. B.2

   The approach curves measured before the different SECM experiments from Chapter 5 can be seen in Fig. B.2 together with their fit. Fig. B.2a and b show the approach curve for the experiments performed with the Pt-UME, changing sample potential and changing scan rate, respectively. Fig. B.2c displays the approach curve performed with the functionalized Au-UME for the pH measurements.
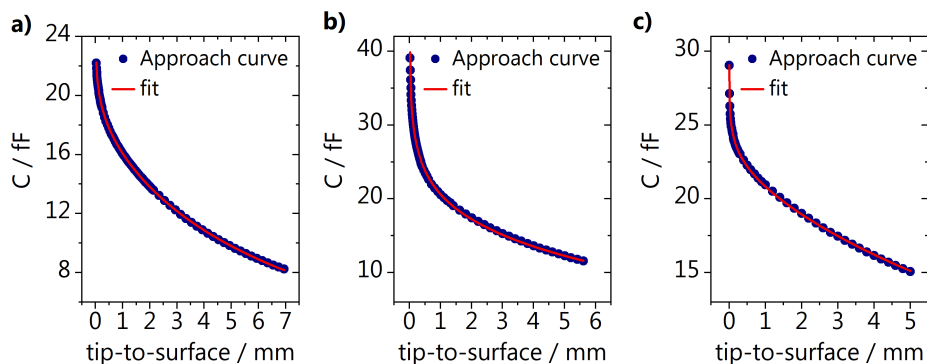
Fig. B.2. Approach curves recorded before the different SECM experiments: **a)** Pt-UME in SG-TC mode with potential steps applied to the sample; **b)** Pt-UME in SG-TC mode constant potential applied to the sample, changing the scan rate of the tip voltammetry; **c)** pH measurements with the functionalized Au-UME.

B.6 CO oxidation measurements with the Pt-UME

During the experiments, the Pt-UME voltammetry was recorded (shown in the manuscript) while the gold sample potential was varied. The chronoamperometry data recorded at the gold sample can be seen in Fig. B.3.

B.7 pH measurements with the functionalized Au-UME

pH measurements were performed by turning CO_2 reduction "on" and "off" at the gold sample and simultaneously recording the functionalized Au-UME voltammetry. The CO_2 reduction reaction was carried out at sample potentials from –0.5 to –1.0 V vs. RHE, in 50 mV steps. Fig. B.4 shows the results, where each data point corresponds to the value extracted from one tip cyclic voltammogram. The pH values displayed in Fig. 5.4 in the main text, correspond to the average of three pH values recorded in 15 seconds. The three data points chosen are the ones acquired at the same time scale the Pt-UME CVs shown in Fig. 5.2 were recorded, after each sample potential step.

B.8 RDE measurements

Before the RDE experiments, the platinum disc electrode was characterized in 0.1 M H_2SO_4 and the blank voltammetry can be found in Fig. B.5.
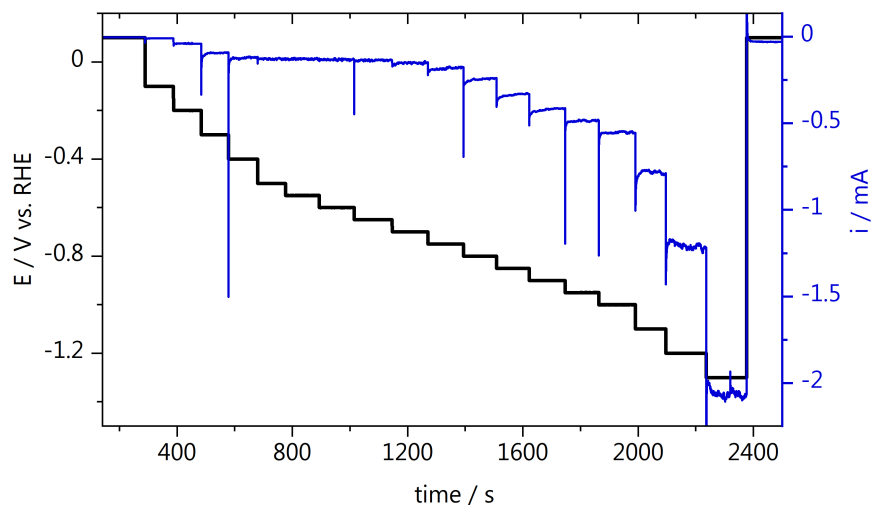
Fig. B.3. Chronoamperometry recorded at the gold sample during CO_2 reduction in 0.1 M Cs_2SO_4, pH = 3.
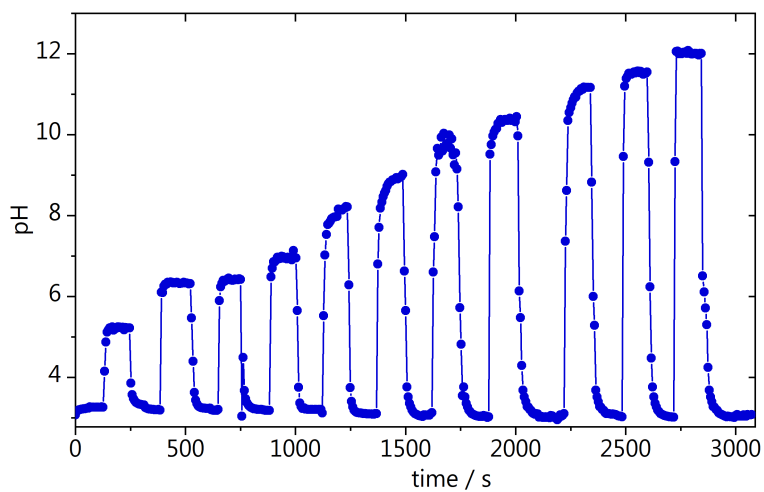

Fig. B.4. pH measured with the Au-UME when the sample potential was varied from -0.5 to -1 V vs. RHE in 50 mV steps.
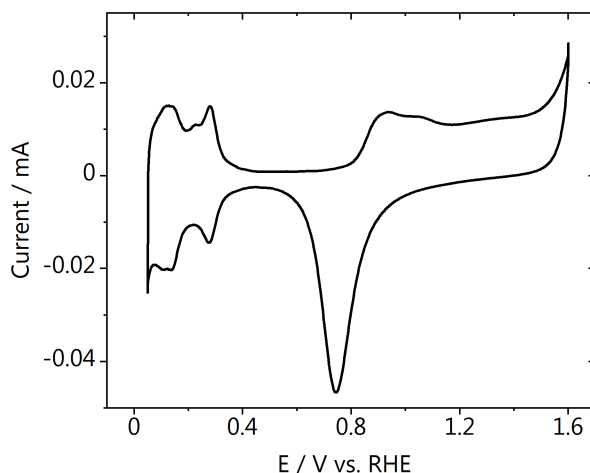
Fig. B.5. Blank voltammetry of the platinum disc taken at 50 mV s^{-1} in argon saturated 0.1 M H$_2$SO$_4$.

The voltammetry of bulk CO electrooxidation on the platinum RDE was recorded at different rotation rates (100, 400 and 900 rpm) in pure Cs$_2$SO$_4$ electrolyte and with the addition of different amounts of KOH. The results can be seen in Fig. B.6, and the diffusion limiting currents from peak I and peak II obtained for each electrolyte were used to derive the diffusion coefficients shown in Chapter 5.

B.9 CO$_2$ reduction products

To exclude that methanol formation at the gold sample is what gives rise to peak II observed in the Pt-UME voltammetry, we performed product analysis in the same electrolyte used in this work (0.1 M Cs$_2$SO$_4$, pH 3) using gas chromatography (GC) and high-pressure liquid chromatography (HPLC). We used a two-compartment electrochemical cell and liquid and gas samples were taken during electrolysis every 20 minutes. As it can be seen in Fig. B.7, only CO and hydrogen were detected by GC and no liquid products were detected by HPLC.
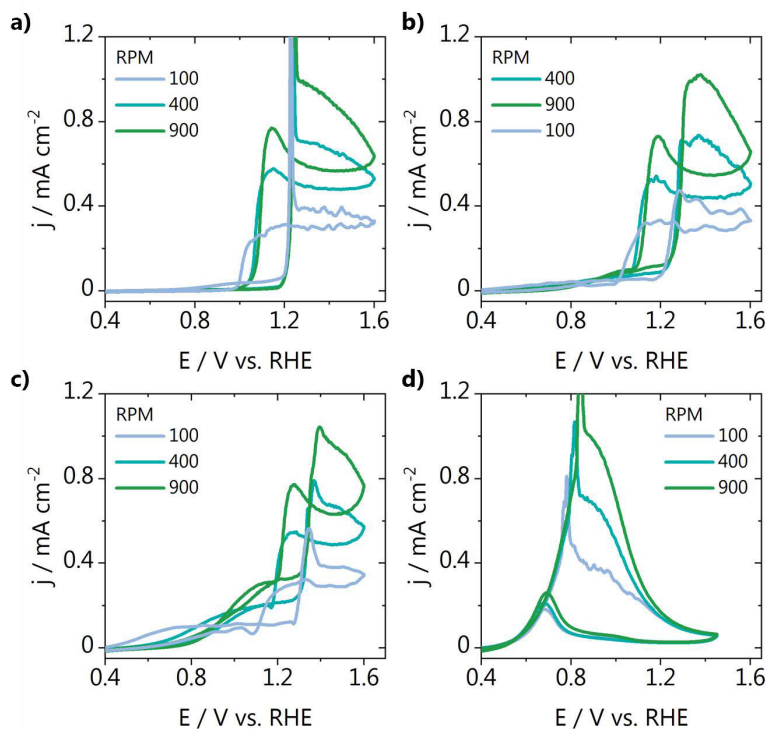
Fig. B.6. CO oxidation voltammetry take at different rotation rates in **a)** Cs_2SO_4 and with the addition of **b)** 0.03 mM, **c)** 0.06 mM, and **d)** 1 mM KOH.
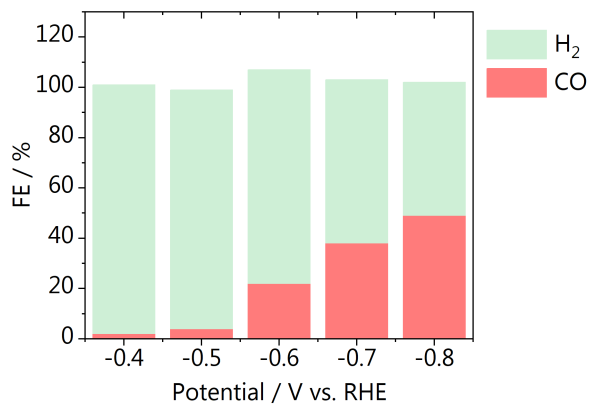
Fig. B.7. Faradaic efficiency for CO_2 reduction on a flat gold electrode, carried out in 0.1 M Cs_2SO_4, pH = 3.

References

(1)   Jacobse, L.; Raaijman, S. J.; Koper, M. T. M. *Phys. Chem. Chem. Phys.* 2016, *18* (41), 28451–28457.

(2)   Monteiro, M. C. O.; Jacobse, L.; Touzalin, T.; Koper, M. T. M. *Anal. Chem.* 2020, *92* (2), 2237–2243.

(3)   Monteiro, M. C. O.; Koper, M. T. M. *Electrochim. Acta* 2019, *325*, 134915.

(4)   Voogd, J. M. De; Spronsen, M. A. Van; Kalff, F. E.; Bryant, B.; Ostoji, O.; Haan, A. M. J. Den; Groot, I. M. N.; Oosterkamp, T. H.; Otte, A. F.; Rost, M. J. *Ultramicroscopy* 2017, *181*, 61–69.

β

C

Methods and supporting information to Chapter 6

C.1 Methods

C.1.1 Materials

All glassware used was cleaned by immersion in a potassium permanganate solution overnight (1 g/L $KMnO_4$ dissolved in 0.5 M H_2SO_4), followed by immersion in dilute piranha. The glassware was further boiled in ultrapure water at least five times. The electrolytes used in this work, KH_2PO_4 (Alfa Aesar, dried, 99.99 %) and K_2SO_4 (Alfa Aesar, Puratronic, 99.997 %, metals basis), were adjusted to pH 3-5 by addition of appropriate amounts of H_2SO_4 (Merck, Suprapur, 96%) or H_3PO_4 (ortho-Phosphoric acid 85%, Suprapur®, Merck).

C.1.2 pH sensor fabrication and characterization

A gold ring electrode (E6R1PK tip, Pine Research Instrumentation) was used in this work, together with a gold disc (diameter = 5 mm, Pine Research Instrumentation). Prior to experiments, the ring and the disc (Pine Research Instrumentation) were polished with a polycrystalline diamond suspension of 0.25 µm (MetaDi, Buehler) and then sonicated (Bandelin Sonorex RK 52H) in ultrapure water (>18.2 MΩ cm, Millipore Milli-Q) for 10 minutes.[1] Before functionalization of the ring with the pH sensing monolayer, the ring and disc were characterized by recording the blank voltammetry between 0.1 and 1.75 V vs. RHE in argon saturated (6.0 purity, Linde) 0.1 M H_2SO_4 (Merck, Suprapur, 96%) in a one compartment electrochemical cell. A gold wire (0.5 mm diameter, MaTeck, 99.9%) was used as counter electrode and a reversible hydrogen electrode (RHE) as reference. The electrochemically active surface area (ECSA) of the disc was calculated based on the charge corresponding to the gold oxide reduction and a surface charge of 386 µC cm^{-2}.[2] The gold ring electrode is modified by immersing it (without the disc inserted) into a 1 mM solution of 4-NTP (Merck, 80%) in ethanol for 15 minutes. The ring is then thoroughly rinsed with ethanol and water, and dried. The disc electrode is carefully inserted in the shaft, avoiding too much friction (which could damage the 4-NTP monolayer). The 4-NTP is then electrochemically reduced to 4-HATP in the working electrolyte (pH ≈ 4) by cycling the ring from 0.3 to -0.43 V vs. Ag/AgCl (argon saturated, 100 mV s^{-1}). It is important to point out that the monolayer can be easily removed from the gold ring by polishing it with a polycrystalline diamond suspension of 0.25 µm. This can be done whenever necessary i.e. when the 4-HATP/4-NSTP signal is for some reason compromised. A decrease in signal can be caused e.g., by bubbles and loss of potential control

during measurements. Considering how simple and fast the pH sensor synthesis is, it is advised to always have a fresh monolayer adsorbed onto the surface at the start of new experiments.

C.1.3 RRDE pH measurements

All electrochemical measurements were carried out using a BioLogic 2-channel potentiostat/galvanostat/EIS (SP-300). The ring and disc electrodes were controlled simultaneously, by two different potentiostat channels. Two gold wires (0.5 mm diameter, MaTeck, 99.9%) were used as counter electrodes and a Ag/AgCl (low profile, BioLogic) as reference. Argon (6.0 purity, Linde) was purged through the solution for 20 minutes prior to the experiments. The argon flow was kept also during the experiments in order to avoid oxygen diffusing into the electrolyte. The ring cyclic voltammetry (CV) was constantly recorded at 200 mV s^{-1} while hydrogen evolution took place at the disc.

C.2 Calculation of the interfacial disc pH

The mid-peak potential (E_{peak}) of the 4-HATP oxidation to 4-NSTP was determined by fitting the forward scans with a Gaussian function containing a linear background (see details in Chapter 3 and Appendix A). E_{peak} was then converted to the ring pH (pH_{ring}) using the calibration curve of the 4-HATP/4-NSTP from our previous work: $pH_{ring} = (0.341 - E_{peak})/0.057$ (Chapter 3).[3] To calculate the interfacial disc pH (pH_{disc}), for an unbuffered electrolyte, we use Eq. C.2, from Yokoyama et al.[4], which is an extension of the analytical solution of Albery and Calvo[5,6] (Eq. C.1), taking the autoprotolysis of water (Eq. C.3) into account.

$$c_r = c_\infty + N_D(c_d - c_\infty) \qquad \text{Eq. C.1}$$

$$c_{r,H^+} - c_{r,OH^-} = N_D(c_{d,H^+} - c_{d,OH^-}) + (1 - N_D)(c_{\infty,H^+} - c_{\infty,OH^-}) \qquad \text{Eq. C.2}$$

$$K_W = c_{rt,H^+}c_{rt,OH^-} \qquad \text{Eq. C.3}$$

where c_∞ represents the proton or OH$^-$ concentration in the bulk and c_d, and c_r, the same at the disc and ring, respectively. The detection efficiency N_D is given by Eq. C.4 and C.5 and is only dependent on the geometrical parameters of the ring and disc electrode (see Fig. C.1). For the electrode used in this work $N_D = 0.23$.

$$N_D = 1 - \frac{1}{6}F\left[\left(\frac{r_2}{r_1}\right)^3 - 1\right] - \frac{2}{3}F\left[\left(\frac{r_2+r_3}{2r_1}\right)^3 - 1\right] - \frac{1}{6}F\left[\left(\frac{r_3}{r_1}\right)^3 - 1\right] \qquad \text{Eq. C.4}$$

where $F[x]$ is:

$$F[x] = \frac{3^{\frac{1}{2}}}{4\pi} \ln\left(\frac{\left(1+x^{\frac{1}{3}}\right)^3}{1+x}\right) + \frac{3}{2}\tan^{-1}\left(\frac{2x^{\frac{1}{3}}-1}{3^{\frac{1}{2}}}\right) + \frac{1}{4} \qquad\qquad \text{Eq. C.5}$$
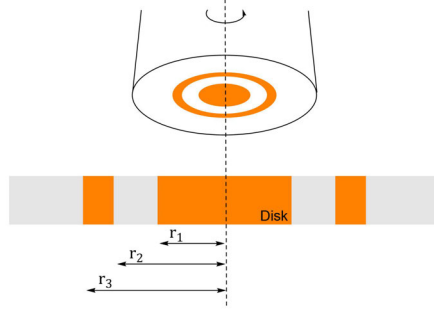

Fig. C.1. Schematic representation of the rotating ring-disc electrode with the geometrical parameters from Eq. C.4 indicated.

Fig. C.2 shows the theoretical relationships between pH_{Disc} and pH_{Ring} at various pH_∞, comparing Eq. C.2 (Yokoyama) and Eq. C.1 (Albery and Calvo) for an unbuffered electrolyte. It can be observed that not taking the autoprotolysis of water into account can lead to over/underestimating the disc pH, depending on the bulk pH. Eq. C.2 is rewritten as follows and used to convert pH_{ring} to pH_{disc} for unbuffered electrolytes:

$$pH_{disk} = -\log\left(\frac{c_{r,H^+} - c_{rt,OH^-}}{N_D} - \frac{c_{\infty,H^+} - c_{\infty,OH^-}}{N_D} + c_{\infty,H^+} - c_{\infty,OH^-}\right) \qquad \text{Eq. C.6}$$

For buffered systems, as the phosphate electrolyte used in this work, a correction must be applied to Eq. C.6, to consider the homogeneous reactions taking place involving the phosphate species. In this case, the OH⁻ concentration is given by Eq. C.7 and is applied to Eq. C.8 to obtain the interfacial disc pH.

$$c'_{OH^-} = c_{OH^-} + [H_2PO_4^-] + 2\,[HPO_4^{2-}] + 3\,[PO_4^{3-}] \qquad\qquad \text{Eq. C.7}$$

$$N_D = \frac{c'_{r,OH^-} - c'_\infty}{c'_{d,OH^-} - c'_\infty} \qquad\qquad \text{Eq. C.8}$$

The following equilibrium constants and equations were used to calculate the concentration of phosphate species[7]:

$$H_3PO_4 \rightleftharpoons H_2PO_4^- + H^+ \qquad K_{a1} = 7.5 \times 10^{-3} \qquad \text{Eq. C.9}$$

$$H_2PO_4^- \rightleftharpoons HPO_4^{2-} + H^+ \qquad K_{a2} = 6.2 \times 10^{-8} \qquad \text{Eq. C.10}$$

$$HPO_4^{2-} \rightleftharpoons PO_4^{3-} + H^+ \qquad K_{a3} = 2.14 \times 10^{-13} \qquad \text{Eq. C.11}$$
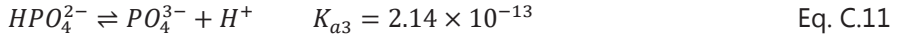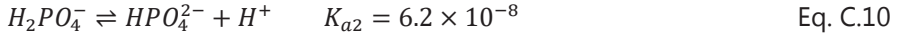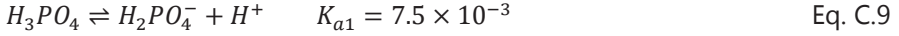
The total concentration of species is given by TC and the concentration of each species to be used in Eq. C.7 is determined based on Eq. C.12-C.16:

$$TC = [H_3PO_4] + [H_2PO_4^-] + [HPO_4^{2-}] + [PO_4^{3-}] \qquad \text{Eq. C.12}$$

$$[H_3PO_4] = \frac{TC[H^+]^3}{[H^+]^3 + K_{a1}[H^+]^2 + K_{a1}K_{a2}[H^+] + K_{a1}K_{a2}K_{a3}} \qquad \text{Eq. C.13}$$

$$[H_2PO_4^-] = \frac{TCK_{a1}[H^+]^2}{[H^+]^3 + K_{a1}[H^+]^2 + K_{a1}K_{a2}[H^+] + K_{a1}K_{a2}K_{a3}} \qquad \text{Eq. C.14}$$

$$[HPO_4^{2-}] = \frac{TCK_{a1}K_{a2}[H^+]}{[H^+]^3 + K_{a1}[H^+]^2 + K_{a1}K_{a2}[H^+] + K_{a1}K_{a2}K_{a3}} \qquad \text{Eq. C.15}$$

$$[PO_4^{3-}] = \frac{TCK_{a1}K_{a2}K_{a3}}{[H^+]^3 + K_{a1}[H^+]^2 + K_{a1}K_{a2}[H^+] + K_{a1}K_{a2}K_{a3}} \qquad \text{Eq. C.16}$$

Finally, expanding Eq. C.7 and C.8, the relationship between pH$_{ring}$ and pH$_{disc}$ for a phosphate buffered electrolyte is given by Eq. C.17:

$$N_D = \frac{c_{r,OH^-} + [H_2PO_4^-]_r + 2[HPO_4^{2-}]_r + 3[PO_4^{3-}]_r - c_{\infty,OH^-} - [H_2PO_4^-]_\infty - 2[HPO_4^{2-}]_\infty - 3[PO_4^{3-}]_\infty}{c_{d,OH^-} + [H_2PO_4^-]_d + 2[HPO_4^{2-}]_d + 3[PO_4^{3-}]_d - c_{\infty,OH^-} - [H_2PO_4^-]_\infty - 2[HPO_4^{2-}]_\infty - 3[PO_4^{3-}]_\infty}$$

$$\text{Eq. C.17}$$

A quartic equation can be derived from Eq. C.7-C.17, where a, b, c, d, and e are parameters of C_{r,OH^-}, and x stands for C_{d,H^+}.

$$ax^4 + bx^3 + cx^2 + dx + e = 0 \qquad \text{Eq. C.18}$$

Solving the equation, four roots can be obtained and the nature of which can be inferred from the sign of the discriminants Δ, P and D. In our cases, all the roots are real and distinct roots since the Δ>0, P<0 and D<0.

$$\Delta = 256a^3e^3 - 192a^2bde^2 - 128a^2c^2e^2 + 144a^2cd^2e - 27a^2d^4 + 144ab^2ce^2 - 6ab^2d^2e - 80abc^2de + 18abcd^3 + 16ac^4e - 4ac^3d^2 - 27b^4e^2 + 18b^3cde - 4b^3d^3 - 4b^2c^3e + b^2c^2d^2$$

Eq. C.19

$$P = 8ac - 3b^2$$

Eq. C.20

$$D = 64a^3e - 16a^2c^2 + 16ab^2c - 16a^2bd - 3b^4$$

Eq. C.21

So that:

$$x_{1,2} = -\frac{b}{4a} - S \pm \frac{1}{2}\sqrt{-4S^2 - 2p + \frac{q}{S}}$$

Eq. C.22

$$x_{3,4} = -\frac{b}{4a} + S \pm \frac{1}{2}\sqrt{-4S^2 - 2p - \frac{q}{S}}$$

Eq. C.23

where:

$$p = \frac{8ac - 3b^2}{8a^2}$$

Eq. C.24

$$q = \frac{b^3 - 4abc + 8a^2d}{8a^3}$$

Eq. C.25

$$S = -\frac{1}{2}\sqrt{-\frac{2}{3}p + \frac{2}{3a}\sqrt{\Delta_0}\cos\frac{\varphi}{3}}$$

Eq. C.26

$$\varphi = \cos^{-1}\left(\frac{\Delta_1}{2\sqrt{\Delta_0^3}}\right)$$

Eq. C.27

with:

$$\Delta_0 = c^2 - 3bd + 12ae$$

Eq. C.28

$$\Delta_1 = 2c^3 - 9bcd + 27b^2e + 27ad^2 - 72ace$$

Eq. C.29

The Eq. C.22 and C.23 are solved and C_{d,H^+} can be determined out of the four solutions by limiting x (C_{d,H^+}) to be positive and relatively smaller than the corresponding C_{r,H^+}. The theoretical relationship that can be obtained using this description between the interfacial ring (pH$_{ring}$) and disc (pH$_{disc}$) pH for phosphate buffered solutions of different bulk pH is shown in Fig. C.2c.
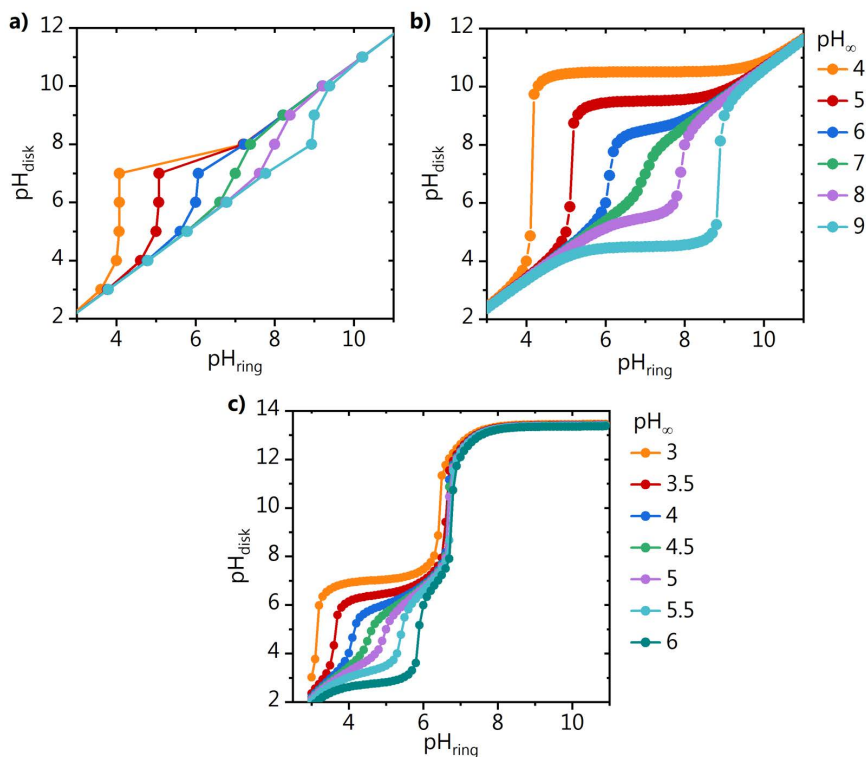
Fig. C.2. Theoretical relationship between pH_{ring} and pH_{disk} for different bulk pH (pH_∞) using **a)** the analytical equation reported by Albery and Calvo[8] and **b)** the extended theory, reported by Yokoyama et al.[4] (both for unbuffered systems), and **c)** the correction presented in this work for a phosphate buffered electrolyte.

C.3   RRDE pH measurements additional data
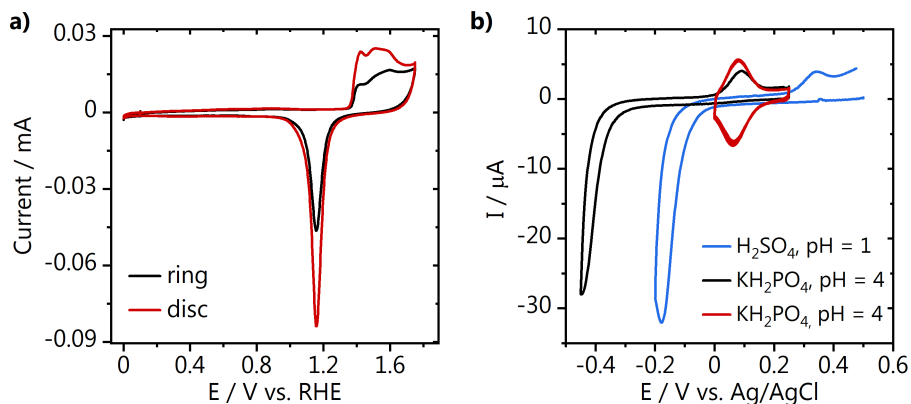
Fig. C.3. a) Blank voltammetry of the ring (black) and disc (red) electrodes taken in 0.1 M H_2SO_4 at 50 mV s^{-1} . **b)** cyclic voltammetry of the 4-NTP to 4-HATP conversion in 0.1 M KH_2PO_4 (black, 100 mV s^{-1}) and 0.1 M H_2SO_4 (blue), together with a characterization of the 4-HATP/4-NSTP redox couple (red, 200 mV s^{-1}) in phosphate.
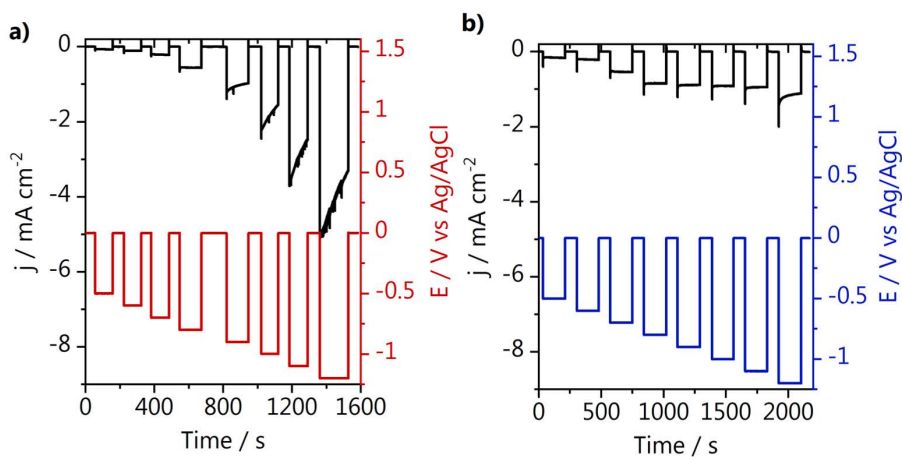
Fig. C.4. Chronoamperometry from pH measurements at different potentials in 0.1 M argon saturated **a)** KH_2PO_4 pH$_{bulk}$ = 4.4 and **b)** K_2SO_4 pH$_{bulk}$ = 3.6 at 1600 rpm.
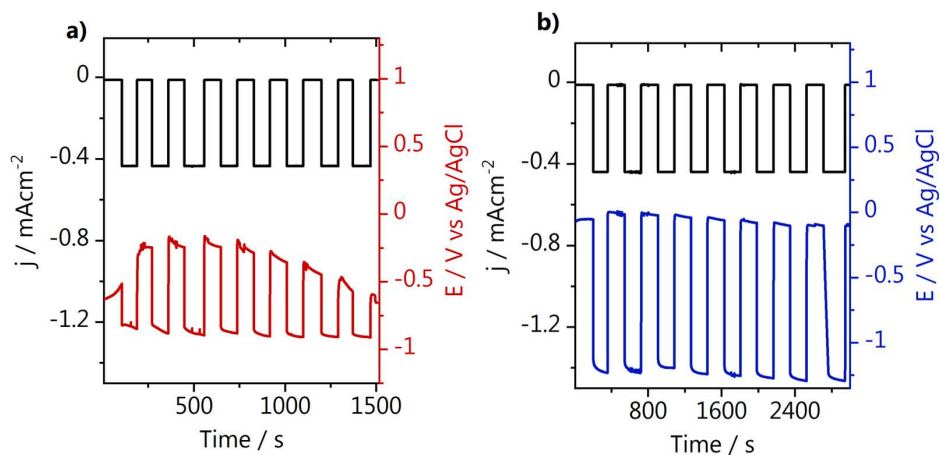
Fig. C.5. Chronopotentiometry from pH measurements in 0.1 M argon saturated **a)** KH_2PO_4 pH_{bulk} = 4.4 and **b)** K_2SO_4 pH_{bulk} = 4.0 at different rotations (500, 750, 1000, 1250, 1500, 1750, 2000, 2600 rpm).
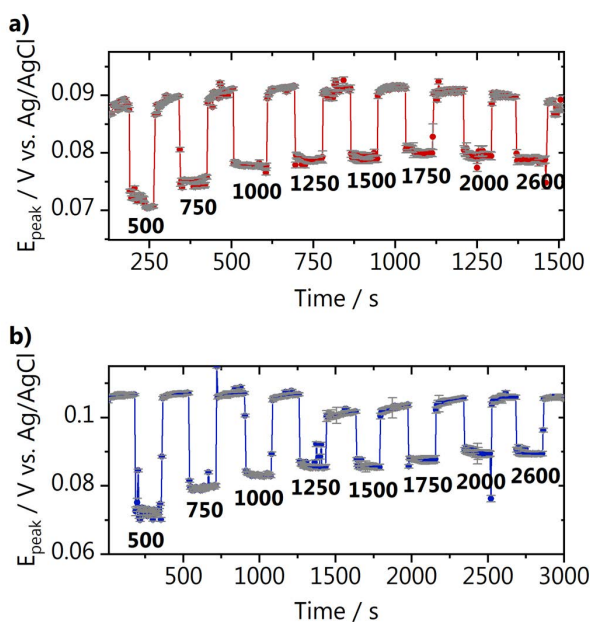
Fig. C.6. Mid-peak potential extracted from the 4-HATP/4-NSTP voltammetry for the experiment in 0.1 M argon saturated **a)** KH_2PO_4 pH_{bulk} = 4.4 and **b)** K_2SO_4 pH_{bulk} = 4.0 at different rotations (500, 750, 1000, 1250, 1500, 1750, 2000, 2600 rpm).

References

(1)   Monteiro, M. C. O.; Koper, M. T. M. *Electrochim. Acta* 2019, *325*, 134915.

(2)   Do, U. P.; Seland, F.; Johannessen, E. A. *J. Electrochem. Soc.* 2018, *165* (5), 219–228.

(3)   Monteiro, M. C. O.; Jacobse, L.; Touzalin, T.; Koper, M. T. M. *Anal. Chem.* 2020, *92* (2), 2237–2243.

(4)   Yokoyama, Y.; Miyazaki, K.; Miyahara, Y.; Fukutsuka, T.; Abe, T. *ChemElectroChem* 2019, *6* (18) 4750–4756.

(5)   Albery, W. J.; Mount, A. R. *J. Chem. Soc. Faraday Trans. 1 Phys. Chem. Condens. Phases* 1989, *85* (5), 1181.

(6)   Albery, W. J.; Calvo, E. J. *J. Chem. Soc. Faraday Trans. 1 Phys. Chem. Condens. Phases* 1983, *79* (11), 2583–2596.

(7)   Powell, K. J.; Brown, P. L.; Byrne, R. H.; Gajda, T.; Hefter, G.; Sjöberg, S.; Wanner, H. *Pure Appl. Chem.* 2005, *77* (4), 739–800.

(8)   Calvo, E. J.; Albery, W. J. *J. Chem. Soc. Faraday Trans. 1* 1983, *79*, 2583–2596.

D

Methods and supporting information to Chapter 7

D.1. **Methods**

Gold disc electrodes of 5 mm in diameter were cut from a polycrystalline gold foil (0.5 mm thick, MaTecK, 99.995%) and prepared by first grinding with a silicon carbide paper (grit size 600, MaTecK) to level and clean the sample, so that a mirror-like surface can be obtained by polishing for the shortest possible time. Subsequently, the electrodes were polished on a microcloth (Buehler) with either diamond suspension (MetaDi 3, 1, 0.25 and 0.05 μm, Buehler) or alumina (3, 1, 0.3 and 0.05 μm, Buehler) for 1 minute with each size. In between polishing steps, the electrodes were cleaned in an ultrasonic bath (Bandelin SONOREX RK 52 H) in ultrapure (>18.2 MΩ cm, Millipore Milli-Q) water for 3 minutes. After the last step, the electrodes were sonicated in ethanol for 3 minutes. and subsequently in ultrapure water for 10 minutes. Different commonly reported gold pre-treatments were also performed: chemical etching in 0.1 M H_2SO_4 (Merck, Suprapur, 96%) by applying a potential of 10 V vs. a graphite counter electrode for 20 seconds and removing the gold oxide layer formed by dipping the electrode in 6 M HCl (Merck, EMSURE® ACS, 37%); electrochemical roughening by cycling the electrode 200 times between 0 and 1.75 V vs. RHE (0.1 M H_2SO_4, 1 V s^{-1}); flame annealing the electrode until it glows and then three subsequent times for 5 seconds using a butane torch held about 1 cm away from the surface. In this study, polishing and (subsequent) flame annealing were performed before each experiment.

All glassware was stored in potassium permanganate solution (1 g L^{-1} KMnO$_4$ dissolved in 0.5 M H_2SO_4) and cleaned prior to each experiment by immersion in dilute piranha in order to remove residues of manganese oxide and permanganate anions. After, the glassware was further cleaned by boiling at least five times in ultrapure water. The electrochemical experiments were performed in a one-compartment cell (Duran, 25 ml) with the gold working electrode in the hanging meniscus configuration. Measurements were carried out using a Bio-Logic potentiostat/galvanostat/EIS (SP-300). A gold wire (0.8 mm thick, Mateck, 99.9%) was used as counter electrode and a reversible hydrogen electrode (RHE) as reference. The gold electrodes were characterized before each experiment by recording a cyclic voltammogram between 0 and 1.75 V vs. RHE (0.1 M H_2SO_4, 0.05 V s^{-1}). The gold electrochemical surface area (ECSA) was determined by calculating the charge corresponding to the gold oxide reduction. The obtained value was normalized to the charge density associated with the reduction of a monolayer of gold oxide (386 μC cm^{-2}).[1] Hydrogen evolution reaction was carried out in 0.1 M

Li$_2$SO$_4$ (Alfa Aesar, anhydrous, 99.99% (metal basis)), unless stated otherwise. Lithium is the alkaline earth cation that promotes HER on gold the least and therefore was chosen for these studies.[2] The solution was brought to pH = 3 by the addition of adequate amounts of H$_2$SO$_4$. The electrolyte was always purged from oxygen by bubbling argon (Linde, 6.0 purity) for 5 minutes prior to the experiments. During the experiments, an argon flow was kept above the electrolyte, to avoid oxygen diffusion into the solution. Appropriate amounts of a 0.01 M Al$_2$(SO$_4$)$_3$ (Acros Organics, 99.999%, trace metal basis) solution were added to the electrolyte in order to perform experiments in the presence of different concentrations of Al^{3+}. The dissolution kinetics of Al$_2$(SO$_4$)$_{3(s)}$ is very slow, therefore the solution was stirred for 48 h at 60 °C until the salt fully dissolved. The 0.01 M Al$_2$(SO$_4$)$_3$ solution pH is 2.7 (due to the cation acidity) and adding it to the background electrolyte (0.1 M Li$_2$SO$_4$) did not lead to changes in the pH. Before each HER experiment, the solution resistance was determined by Electrochemical Impedance Spectroscopy (EIS) and the electrode potential was compensated for 85% of the ohmic drop. All the voltammograms in this work show the first cycle recorded, unless stated otherwise.

The gold electrode topography and composition were characterized by Scanning Electron Microscopy (SEM) in an Apreo SEM (ThermoFisher Scientific). Micrographs were obtained using an acceleration voltage of 10 kV and an electron beam current of 0.4 nA. Energy Dispersive X-Ray Spectrometry (EDX) was used for elemental analysis (Oxford Instruments X-Max^N 150 Silicon Drift detector). EDX data processing was done with the Pathfinder™ X-ray Microanalysis software v1.3. The data is displayed in atomic percentage for easier visualization however the quantification was performed in automatic mode (without providing external standards).

D.2. Micrographs of polished gold electrodes

This section contains additional scanning electron (SEM) micrographs of the gold electrodes after polishing with diamond or alumina and flame annealing three times using a butane torch. As can be seen in Fig. D.1a, polishing with diamond leads to a clean electrode, with a few large contaminating diamond particles on the surface. Opposite, polishing with alumina (Fig. D.1b) leads to contaminating alumina particles of various sizes (from 100 nm to 3 μm) distributed over the whole surface. Higher magnification images also show the presence of small corrosion pits from polishing, and carbonaceous deposits due to flame annealing.
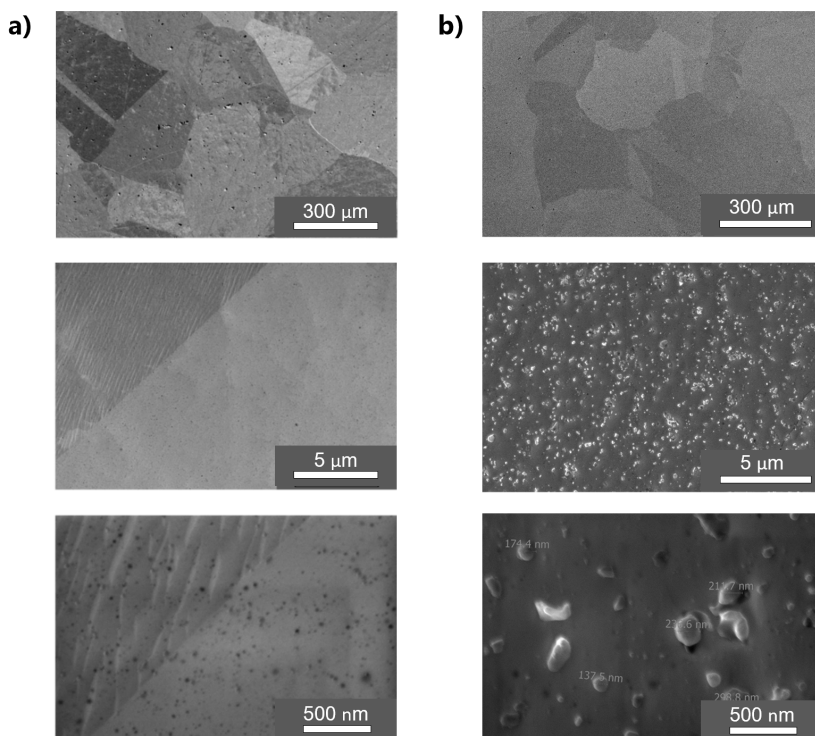
Fig. D.1. SEM micrographs of gold polished with **a)** diamond or **b)** alumina and flame annealed.

D.3. **Gold surface preparation**

This section contains additional SEM micrographs of the gold electrodes after polishing with diamond and applying different surface preparation methods for gold electrodes. Diamond was chosen here as polishing media, because the alumina particles are detrimental to the proper visualization of the surface topography. Only polishing (Fig. D.2a) leads to a surface that contains scratches and pits of different sizes. During our studies we observed that the gold voltammetry of electrodes that are only polished is not very reproducible. Polishing followed by flame annealing, on the other hand, smoothens the surface and brings it to its most stable state, where defined grains and grain boundaries are observed (Fig. D.2b). The flame annealing procedure reported in this work (1x until glowing + 3x for 5 seconds at 1 cm distance of the electrode), when systematically performed, leads to a very clean and reproducible surface (see the cyclic voltammograms displayed in the following section). It is important to notice that the quality of the flame annealed surface is

directly related to the quality of the mechanical polishing procedure. Chemically etching the gold electrode after polishing (Fig. D.2c), leads to partial removal of polishing contaminants by the removal of gold layers. To remove enough gold layers, etching has to be performed for long enough periods, although this significantly increases the surface roughness. If a smooth, reproducible, and highly crystalline surface is desired, prolonged chemical etching is therefore not recommended. Roughening the polished electrode by repeated cycling at high scan rate, leads to the formation of nanoparticles that are more homogeneously distributed in the polished (Fig. D.2d) than in the polished and flame annealed electrode (Fig. D.2e). The reactivity of nanoparticles is different than of flat surfaces, and not much is known about their stability during electrochemical experiments. Based on this evaluation, we concluded that polishing with diamond and flame annealing gold (following a strict protocol) is the best way to obtain a clean and reproducible surface for fundamental cyclic voltammetry studies.
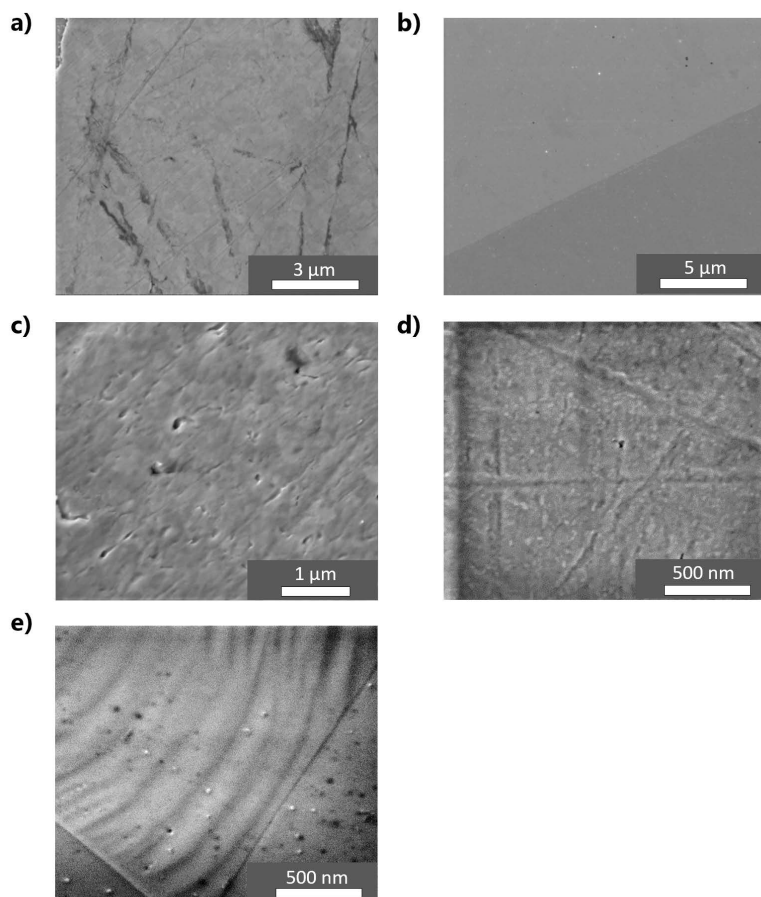
D

Fig. D.2. SEM micrographs of gold electrodes **a)** polished with diamond and additionally **b)** flame annealed 1x until glowing and subsequently 3x for 5 s, **c)** chemically etched in 0.1 M H_2SO_4 at 10 V vs. OCP for 20 seconds, **d)** electropolished by 200 cycles from 0 to 1.75 V vs. RHE in 0.1 M H_2SO_4 at 1 V s^{-1}, **e)** flame annealed and electropolished.

D.4. **Surface characterization after hydrogen evolution**

The topography and composition of the gold electrodes polished with diamond (Fig. D.3a) or alumina (Fig. D.3b) was evaluated after the hydrogen evolution reaction. Fig. D.3 shows that for both cases the contaminating particles remain on the surface after the reaction is carried out. In addition, by comparison with the EDX spectra obtained before the experiments (see Chapter 7), the surface composition remains unchanged. No sulphur is detected by EDX, even though HER was performed in a sulphate containing electrolyte.
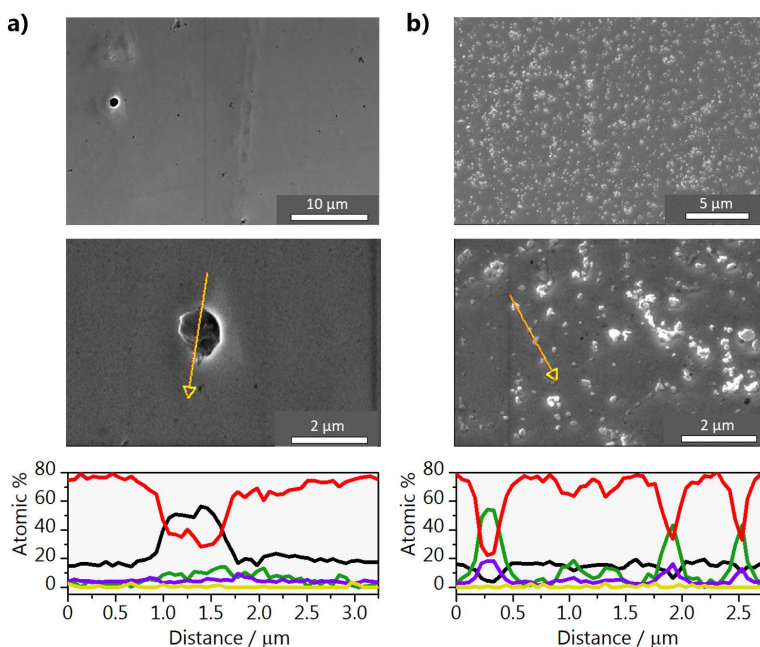

Fig. D.3. SEM micrographs and EDX line spectra of the gold electrodes polished with **a)** diamond or **b)** alumina after hydrogen evolution. The lines refer to the following signals: (—) C K, (—) O K, (—) Al K, (—) Au M and (—) S K.

D.5. HER in the presence of different Al³⁺ concentrations

Experiments adding micro molars of Al^{3+} to the background electrolyte were carried out in order to confirm that the enhancement in HER activity by the presence of alumina particles is actually due to the release of Al^{3+} cations in the electrolyte. Before each experiment, gold electrodes were polished with diamond, flame annealed and characterized. The resulting cyclic voltammograms (CVs) from Fig. D.4 show that the preparation method chosen leads to a reproducible surface, which is very important when performing voltammetry studies. The electrode was also characterized after the HER experiments. The CV of gold before and after HER is shown in Fig. D.5a and no significant changes are observed in the blank voltammetry. SEM characterization, on the other hand, shows that deposits form on the surface during HER, in the form of flakes. The micrograph shown in Fig. D.5b displays how these deposits are homogeneously distributed throughout the surface. An image at higher magnification and EDX line spectra are presented in Chapter 7. The elemental composition found by EDX together with the speciation diagram from Fig. D.6a indicate that these flakes are $Al(OH)_3$. The deposition can happen, as during hydrogen evolution the local pH is more alkaline than the bulk.
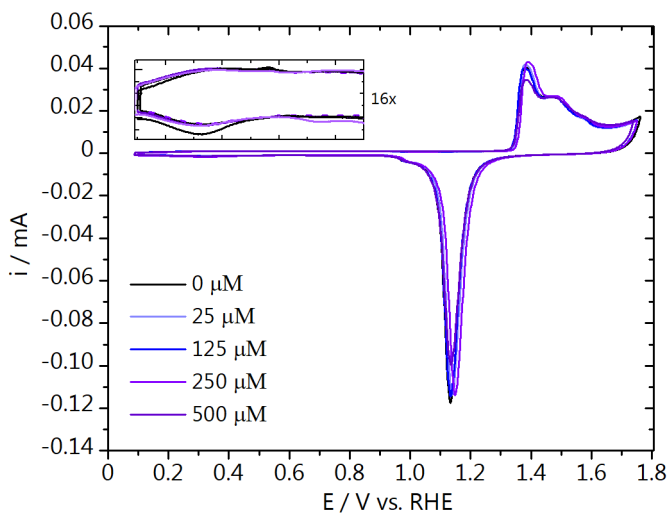

Fig. D.4. Cyclic voltammogram of gold electrodes polished with diamond paste taken at a scan rate of 50 mV s^{-1} in 0.1 M H$_2$SO$_4$ before the Al^{3+} addition experiments.
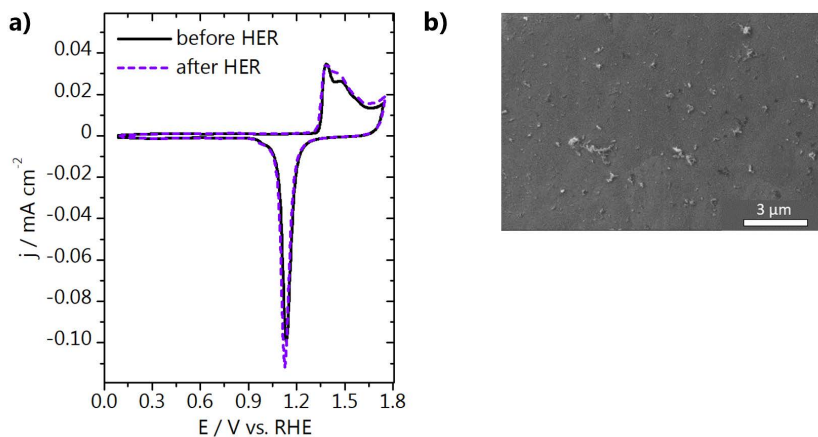
Fig. D.5. a) Comparison of the cyclic voltammogram of gold before and after the HER experiment with 500 µM $Al_2(SO_4)_3$ added to the electrolyte. CV taken at a scan rate of 50 mV s^{-1} in 0.1 M H_2SO_4. **b)** SEM micrograph after HER.

D.6. Speciation of Al^{3+} and aluminium hydroxide deposition

A speciation diagram of Al^{3+} was constructed with the Hydra-Medusa software[3], in order to support that the flakes found on the surface after HER in the presence of Al^{3+} are $Al(OH)_3$. The diagram can be seen in Fig. D.6a, where the molar fraction of aluminium containing species present in the electrolyte is shown as a function of pH. Even though the diagram is plotted as a function of the aluminium containing species, the real concentrations and solubility products of all the different ionic species present in the working electrolyte (H^+, OH^-, H_3O^+, SO_4^{2-}, Li^+, and Al^{3+}) are taken into account for the calculations. It can be seen that below pH 3.7, aluminium is octahedrally coordinated by water molecules (as Al^{3+}) or complexed with SO_4^{2-}. At higher OH^- concentrations, starting at pH 4.2, the number of OH^- bound to each Al^{3+} increases and polymerization of the octahedrons starts to take place through sharing of edge atoms. Above pH 5.2, the polymerization process leads to the formation of planar $Al(OH)_3$ sheets, where each aluminium ion shares 3 pairs of OH^- with 3 other aluminium ions.[4] See the top and side view of the $Al(OH)_3$ sheets structure in Fig. D.6b. Experiments in 0.01 M $Al_2(SO_4)_3$ electrolyte were performed in order to confirm that aluminium cations deposit on the gold electrode surface due to an increase in local pH during HER. Below, additional SEM images of the layer formed and an EDX line scan are presented. Fig. D.7a shows that $Al(OH)_3$ plates are formed during HER, with a spacing of 1-3 µm in between them.
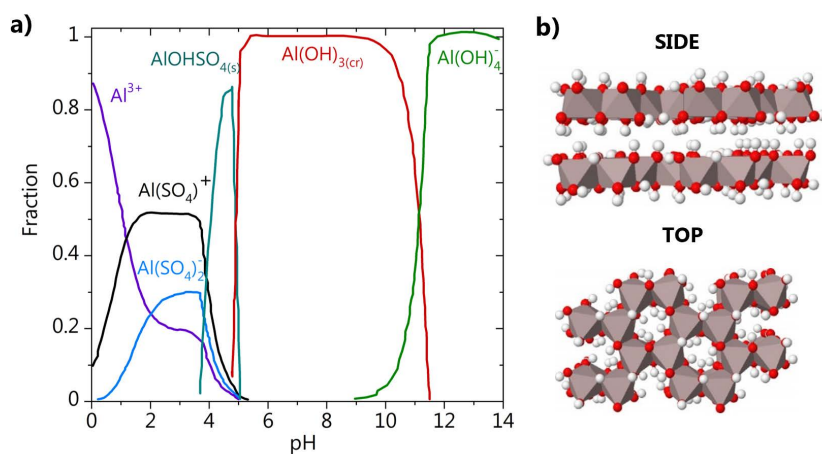
Fig. D.6. a) Speciation diagram of Al^{3+} in the experimental conditions used in this work (HER in 0.1 M Li_2SO_4 + 500 µM $Al_2(SO_4)_3$). This diagram was constructed with the software Hydra-Medusa and is presented as provided. **b)** Molecular structure of $Al(OH)_3$ sheets. Figure adapted from reference.[5]
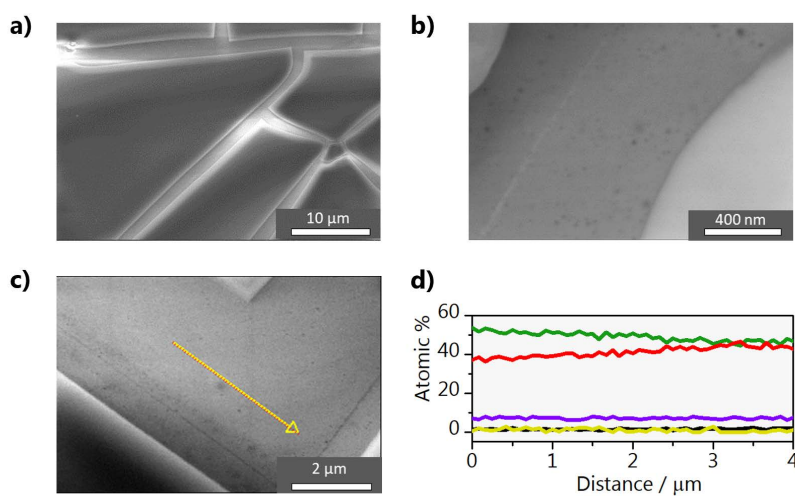
Fig. D.7. SEM micrographs characterizing **a)** the aluminium hydroxide layer deposited on gold, **b)** the region in between the aluminium hydroxide sheets, **c)** and **d)** EDX line spectra determining the composition in the region between the hydroxide sheets. The lines refer to the following signals: (—) C K, (—) O K, (—) Al K, (—) Au M and (—) S K.

Table D.1. Layer composition measured by EDX in 3 different spots of the Au-Al(OH)$_3$ modified electrode.

	Atomic %				
	C	O	Al	Au	S
1	1	74.89	12.07	6.13	5.04
2	0	75.86	12.89	4.26	5.46
3	0	76.26	12.91	5.06	5.57

Fig. D.8. Cyclic voltammogram of gold in 0.1 M H$_2$SO$_4$ taken at a scan rate of 50 mV s^{-1} before and after HER experiment in 0.01 M Al$_2$(SO$_4$)$_3$.
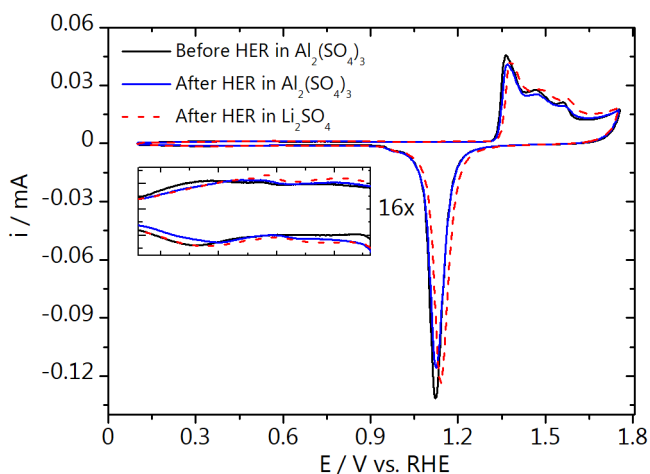
The EDX line scan (Fig. D.7d) from the region showed in Fig. D.7c, demonstrates that the gold is not fully exposed in the region in between the plates, and a thin layer containing Al and O can be found. The thickness of this layer is probably only a few nanometres, as the EDX line scan going through the 128 ± 14 nm thick plate, shows a much lower Au signal. The fact that no sulphur is found in this region (but it is present in the plates) also suggests that this is a thin initiation layer, instead of the highly crystalline hydroxide sheets intercalated with sulphate anions. In order to assure the composition of the surface deposits, EDX scans were also performed in 3 different spots of the sample. Table D.1 shows that the layer composition is nearly the same for the 3 different measurements, which is expected considering the high crystallinity of the Al(OH)$_3$ sheets.

Fig. D.8 shows the CVs of the gold electrodes before HER in 0.01 M Al$_2$(SO$_4$)$_3$ (black), directly after HER with the Al(OH)$_3$ sheets on the surface (blue) and after

this Au-Al(OH)$_3$ modified electrode was used for HER in 0.1 M Li$_2$SO$_4$ (red dotted line). Surprisingly, the gold CV remains nearly unchanged, with only a small decrease in the gold oxidation and reduction peaks when the hydroxide sheets are present on the surface. This indicates that the deposited layer is highly porous and does not hinder access of the electrolyte to the gold.

D.7. Removal of alumina from the surface

Prolonged etching after polishing the electrode with alumina was performed (2x 60 seconds), as an attempt to fully remove the alumina particles of the surface. The sample was subsequently flame annealed. SEM micrographs from Fig. D.9b show that prolonged etching does not lead to full removal of the alumina particles. Fig. D.9a shows the comparison of the HER curves obtained for the gold electrode polished with diamond, alumina, and alumina with subsequent prolonged etching. Results show that 2 minutes are not enough to fully remove the particles and that their corrosion still leads to larger HER currents than obtained on gold polished with diamond. It is important to point out that the time scale of these experiments is very short, and certainly in longer experiments, an increasing amount of Al^{3+} cations will be present in the electrolyte and this effect will be even more pronounced.
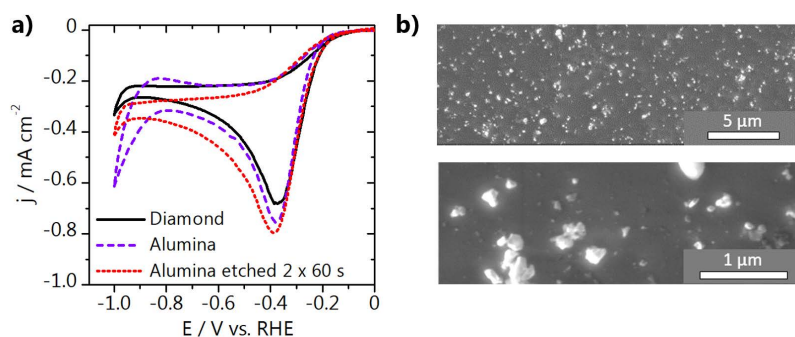
Fig. D.9. a) Cyclic voltammogram of HER on gold electrodes polished with alumina (with and without 2 etching cycles of 1 min) and polished with diamond in argon saturated 0.1 M Li$_2$SO$_4$ taken at a scan rate of 50 mV s^{-1} (pH = 3) and **b)** SEM micrographs after etching.

References

(1)   Do, U. P.; Seland, F.; Johannessen, E. A. *J. Electrochem. Soc.* 2018, *165* (5), H219–H228.

(2)   Xue, S.; Garlyyev, B.; Watzele, S.; Liang, Y.; Fichtner, J.; Pohl, M. D.; Bandarenka, A. S. *ChemElectroChem* 2018, *5* (17), 2326–2329.

(3)   Puigdomenech, I. KTH Royal Institute of Technology: Stockholm 2015.

(4)   Hem, J. D.; Roberson, C. E. *USGPO* 1967, No. 1827-A.

(5)   Lisensky, G. Solid State Structures https://archive.education.mrsec.wisc.edu/pmk/pages/AlOExample.html (accessed Jul 9, 2019).

D

E

Methods and supporting information to Chapter 8

E.1. Methods

E.1.1 Cyclic voltammetry experiments

CO_2 reduction measurements were performed in a three-electrode glass cell in which the reference was a reversible hydrogen electrode (RHE) separated from the work compartment by a Luggin capillary and the counter electrode was a gold wire (0.8 mm thick, Mateck, 99.9%). Polycrystalline gold (0.5 mm thick, MaTecK, 99.995%) discs of 5 mm in diameter were used as working electrode in the hanging meniscus configuration. The surface was first prepared using the procedure reported in Chapter 7.[1] After each flame annealing, the electrode was characterized by cyclic voltammetry in 0.1 M H_2SO_4 (Merck, Suprapur, 96%). The electrochemical surface area (ECSA) was determined using the charge corresponding to the gold oxide reduction peak. The charge was converted to surface area using the charge density associated with the reduction of a monolayer of gold oxide (386 μC cm^{-2}).[2] Prior to the experiments, the glassware was stored in potassium permanganate solution (1 g L^{-1} $KMnO_4$ dissolved in 0.5 M H_2SO_4), and afterwards cleaned by immersion in dilute piranha and boiled at least five times in ultrapure water. Measurements were performed in 50 ml of electrolyte, using a Bio-Logic potentiostat/galvanostat/EIS (SP-300). The experiments in the absence of metal cations were performed in 1 mM H_2SO_4 (Merck, Suprapur, 96%). Other measurements were performed using different high purity sulfate electrolytes: 1 mM Li_2SO_4 (Alfa Aesar, anhydrous, 99.99%, metal basis), 1 mM Na_2SO_4 (Alfa Aesar, Puratronic™, 99.9955%, metals basis), 1 mM K_2SO_4 (Alfa Aesar, Puratronic™, 99.997%, metals basis) and 1 mM Cs_2SO_4 (Alfa Aesar, Puratronic™, 99.997%, metals basis). During the measurements the electrolyte was constantly purged with argon or CO_2 and the pH was always adjusted to 3 using H_2SO_4. The solution resistance was determined by performing Potentiometric Electrochemical Impedance Spectroscopy (PEIS) prior to every measurement and the electrode potential was always automatically compensated for 85% of the ohmic drop.

E.1.2 SECM measurements

The SECM measurements were performed in our home-built SECM setup, previously described in Chapter 3.[3] The SECM cell cleaning and all equipment used are the same as previously reported.[3] The SECM samples were prepared and characterized prior to every measurement. The polycrystalline gold, silver and copper samples were mechanically polished exactly like described for the gold disc

used in the hanging meniscus experiments. The copper sample was further electropolished in 66% H_3PO_4 at 3 V vs. a Cu counter electrode for 10 seconds. The SECM gold sample was characterized by cyclic voltammetry in 0.1 M H_2SO_4 (Merck, Suprapur, 96%). The silver sample was characterized by thallium under potential deposition (UPD) carried out in a mixture of 0.1 M Tl_2SO_4 (ACROS Organics™, 99.9%, trace metal basis) + 0.1 M H_2SO_4 (Merck, Suprapur, 96%) + 0.5 M Na_2SO_4 (Alfa Aesar, Puratronic™, 99.9955%, metals basis). The copper sample was characterized by cyclic voltammetry in 0.1 M NaOH (Merck, EMPLURA®, 32%). All electrolytes were purged with argon prior to the characterization. For both the characterization and SECM measurements a gold wire was used as counter electrode when using the gold sample, and a platinum wire used for the silver and copper electrodes. A platinum ultramicroelectrode (Pt-UME) was fabricated by etching and sealing a platinum wire (50 μm diameter, Goodfellow, 99.99%) into a soda lime glass capillary using a butane torch. The detailed procedure is reported elsewhere.[4] The Pt-UME was polished before every set of SECM measurements and further cleaned by cycling 200 times between 0.06 and 1.60 V vs. RHE in 0.1 M H_2SO_4 at 1 V s^{-1}, always resulting in a reproducible blank voltammogram. The Pt-UME used in this work has a radius of approximately 6.4 ± 0.05 μm determined using the $Fe(CN)_6^{3-}/Fe(CN)_6^{4-}$ outer sphere reaction. Before the measurements the tip-to-surface distance was determined using a capacitive approach performed in air. The details can be found in Chapter 3.[3] All SECM measurements were performed with the Pt–UME at a fixed distance (50 ± 2μm) from the surface. A 2–channel Bio-Logic potentiostat/galvanostat/EIS (SP-300) was used to control the sample and the tip individually. Chronoamperometry was performed at the sample for 10 seconds and subsequently the tip cyclic voltammetry was recorded at 200 mV s^{-1}. During the experiments, the electrolyte was constantly purged with CO_2 or argon and an argon flow was kept above the solution to avoid oxygen diffusing into the solution. The electrolyte used was 1 mM H_2SO_4 (pH = 3) with the addition of 140 μM Cs_2SO_4 when necessary (Alfa Aesar, Puratronic™, 99.997%, metals basis).

E.1.3 Density Functional Theory parameters

Density Functional Theory (DFT) simulations were performed with the VASP code.[5,6] We choose the PBE density functional[7] including dispersion through the DFT-D2 method,[8,9] with our reparametrized C_6 coefficients.[10] Inner electrons were represented by PAW pseudopotentials[11,12] and the monoelectronic states for the

valence electrons were expanded as plane waves with a kinetic energy cutoff of 450 eV.

E.1.4 Computational model

Polycrystalline Au was modeled by a $3\sqrt{3}\times3\sqrt{3}-R30°$ Au(111) (4 layers, 15.3 Å × 15.3 Å × 30.0 Å, 8 Å vacuum thickness), which was geometrically optimized (2 outermost layers relaxed, bulk fixed). The Brillouin zone was sampled at the Γ–point. Since Pt and Au have similar lattice constants, we inherited the solvent configuration (72 H_2O molecules, 15 Å thick) optimized by AIMD for 11 ps at 300 K from our previous study regarding water-metal interface for $3\sqrt{3}\times3\sqrt{3}-R30°$ Pt(111).[13] We inserted the pre-equilibrated water molecules on top of the Au surface and we carried out AIMD simulations for a total of 6 ps (1 ps of equilibration + 5 production, 1 fs time step), in a canonical NVT ensemble at 300 K regulated by a Nosé-Hoover thermostat.[14–16] First, we optimized the hydrogen bond network between the water molecules for 2 ps on the Au–H_2O system (Fig. E.8). Then, we inserted an alkali metal cation M^+ (Li^+, Na^+, K^+, Cs^+) in a cavity of the first solvation layer close to the surface, whilst we removed a hydrogen from a water molecule in the fourth water bilayer to keep charge balance. The cation coverage was set to 0.04 ML (1/27), which corresponded to a surface concentration of 0.5–0.8 M. The resulting four systems were named Au-H_2O-M^+ and underwent AIMD for 2 additional ps. Finally, we added a CO_2 (0.04 ML, 1/27) to the Au-H_2O and 4 Au-H_2O-M^+ proximal to the catalytic surface and the cation. The resulting 4 Au-H_2O-M^+-CO_2 and 1 Au-H_2O-CO_2 systems underwent AIMD for 2ps and 1 ps, respectively, and were used to investigate the activation of CO_2 in the presence and absence of an alkali cation (Fig. E.8). As the cation, CO_2, and the explicit water molecules were placed only on one side of the slab, we applied a dipole correction to remove spurious contributions arising from the asymmetric slab model.[17]

E.1.5 Data analysis

Cation-water radial distribution functions were obtained for the 2 ps equilibration of the Au-H_2O-M^+ systems. From these parameters, we determined the cation coordination number to water or CO_2 oxygens. Finally, the CO_2 binding energy at U = 0.0 V vs. RHE in the presence and absence of a cation was averaged from static DFT single point calculations from AIMD configurations taken every 20 fs during the last 0.5 ps with standard deviation taken as uncertainty. Gibbs free energies were calculated at 298.15 K by correcting DFT energies for entropic

contributions. The energy references were chosen as CO_2(g) and single point calculations of the previously described $Au–H_2O–CO_2$ and $Au–H_2O–M^+–CO_2$ configurations upon removal of the CO_2 molecule (Eq. E.1).

$$* + M^+(H_2O)_N + CO_2 + e^- \rightleftharpoons * CO_2^- + M^+(H_2O)_N; \ \Delta G_{CO_2} \qquad \text{Eq. E.1}$$
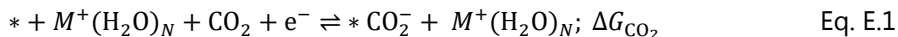
E.1.6 Cation accumulation at the outer Helmholtz plane

To assess the thermodynamics of cation accumulation at outer Helmholtz plan (OHP), we applied the methodology introduced by Resasco et al.[18] The energy of a solvated cation at the bulk electrolyte can be referenced to the energy of the bulk alkali metal following the principles of the Computational Hydrogen Electrode.[19] At the standard reduction potential U_0,[20] a cation M^+ is in equilibrium with its reduced state M, Eq. E.2. Thus, we can derive the energy of the cation/electron pair at a given potential U vs SHE from the DFT energy of the bulk alkali metal, Eq. E.3.

$$M^+ + e^- \leftrightarrow M, \ U = U_0 \qquad \qquad \text{Eq. E.2}$$

$$E_{M^++e^-} = E_M - |e^-|\,(U - U_0) \qquad \qquad \text{Eq. E.3}$$

We can instead estimate the energy of a cation at the OHP at $U = 0$ V vs SHE from our *ab initio* molecular dynamics simulations, since we specifically inserted an alkali metal at the OHP, which donates its valence electron to the solvation layer, Eq. E.4. The gold surface is represented by the symbol *, whilst the solvation layer is indicated by solv. Thus, we can calculate the thermodynamic driving force for each cation to accumulate at the OHP as in Eq. E.5. Considering the lowest energy configurations for Li^+, Na^+, K^+, Cs^+ during the last 2 ps of AIMD simulation, E(OHP) – E(bulk electrolyte) correlates with cation ionic radius.[21] Cations with larger radius are thermodynamically more prone to accumulate at the OHP, thus they exhibit higher concentration across the surface/electrolyte interface.[18]

$$* + \text{solv} + M \rightarrow * + \text{solv} + M^+ + e^-, E_{M^++e^-}(\text{OHP}) \qquad \text{Eq. E.4}$$
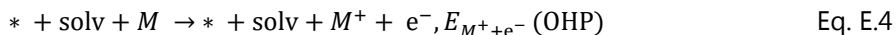
$$\Delta E = E_{M^++e^-}(\text{OHP}) - E_{M^++e^-}(\text{bulk}) \qquad \qquad \text{Eq. E.5}$$

E.1.7 Data availability

The datasets generated though Density Functional Theory simulation and analysed during the current study are available in the ioChem-BD database[22] at DOI: 10.19061/iochem-bd-1-194.[23]

E.2. Hanging meniscus experiments

E.2.1 Characterization of the gold electrode

Before all the CO_2 reduction experiments in hanging meniscus configuration were performed, the gold electrode was flame annealed using the protocol previously described[1] and the electrode was characterized in 0.1 M H_2SO_4. The characterization by cyclic voltammetry (CV) was done in between all measurements, to assure a reproducible surface which allows for comparison of the CO_2 reduction results and determination of the electrochemical active surface area. The characterization CVs recorded during the hanging meniscus experiments presented in the main text can be found in Fig. E.1.
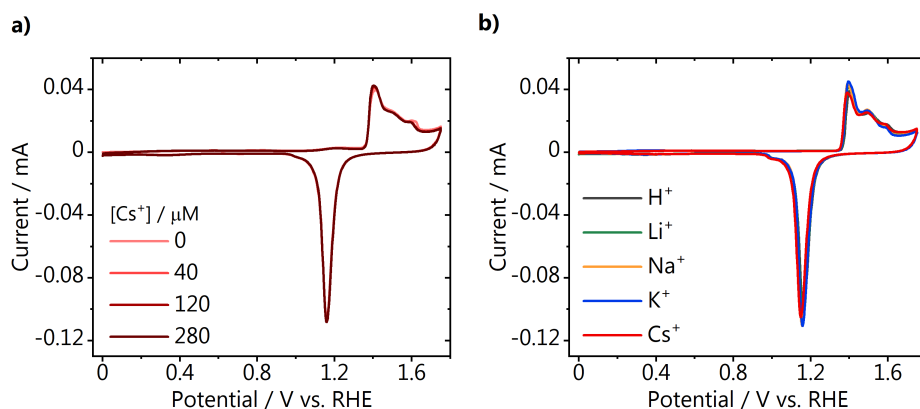

Fig. E.1. Blank voltammetry of the gold electrode used in the hanging meniscus experiments after surface preparation through polishing and flame annealing. **a)** CVs recorded before the measurements in 1 mM H_2SO_4 with the addition of different amounts of Cs^+, **b)** CVs recorded before the measurements in 1 mM M_2SO_4 (M = H, Li, Na, K, Cs).

E.2.2 Hydrogen evolution and CO_2 reduction in 1mM M_2SO_4 (M = H, Li, Na, K, Cs)

Hydrogen evolution and CO_2 reduction were also carried out in 1 mM sulfate solutions of different cations, all adjusted to pH = 3 when necessary. The cyclic voltammetry can be seen in the figure below, together with the results obtained in 1 mM H_2SO_4, for comparison. To calculate the CO oxidation charge density shown in the main text, the double layer charge recorded in Argon was subtracted from the total charge found in CO_2 atmosphere.
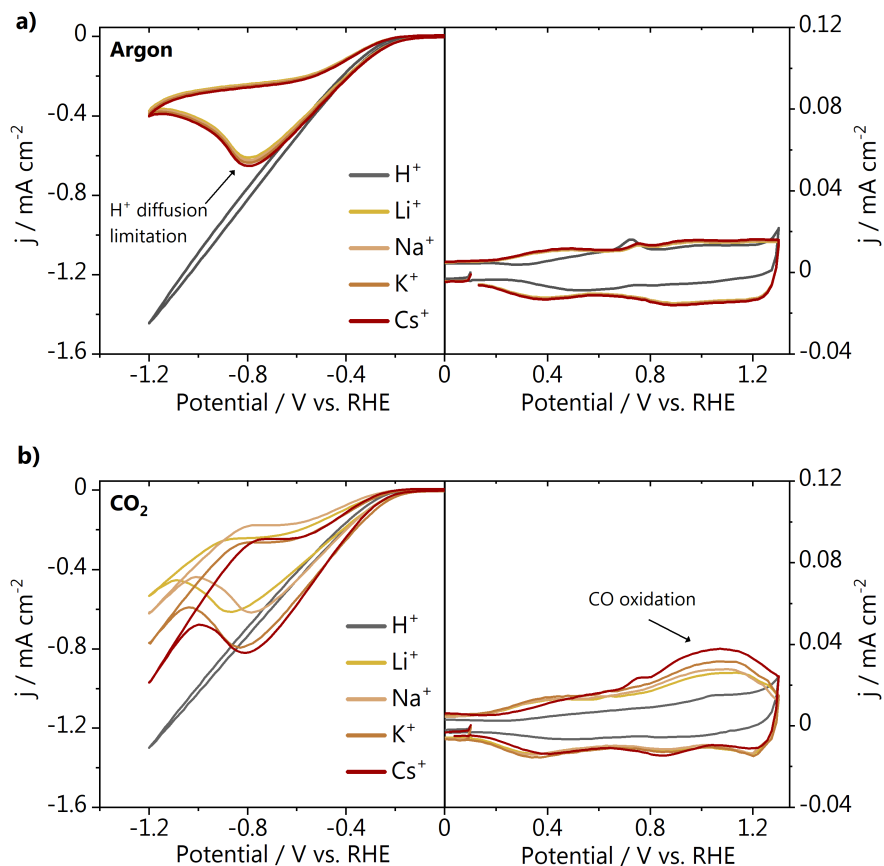
a)

b)

Fig. E.2. Cyclic voltammetry recorded in **a)** argon and **b)** CO_2 atmosphere on gold in 1 mM M_2SO_4 (M = H, Li, Na, K, Cs) at pH = 3 (50 mV s^{-1}).

E.2.3 CO oxidation control experiment

A control experiment was performed to show that CO can be oxidized on the gold electrode in the absence of a metal cation in the electrolyte. Before the measurement the gold electrode was characterized in argon saturated 0.1 M H_2SO_4 electrolyte. The 0.1 M H_2SO_4 electrolyte was saturated with CO for 5 minutes and subsequently a cyclic voltammogram was recorded. Fig. E.3 displays both CVs, in which the large anodic current (red curve) starting at 0.8 V vs. RHE shows that CO can be oxidized without a metal ion in solution.
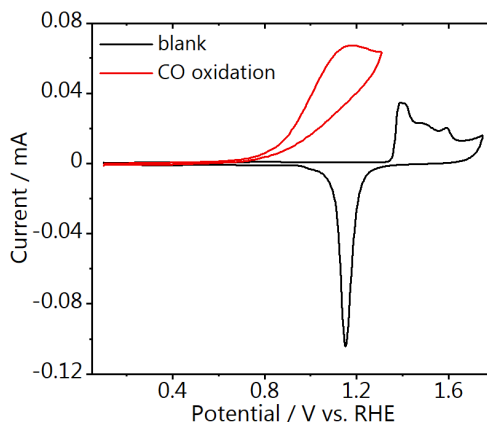
Fig. E.3. CO oxidation voltammetry on gold recorded in 0.1 M H_2SO_4 after saturation the electrolyte with CO (50 mV s^{-1}).

E.2.4 CO_2 reduction in 1mM H_2SO_4 + µM Cs$^+$

CVs were recorded directly after the CO_2 reduction cathodic scan from 0 to – 1.2 V vs. RHE in 1 mM H_2SO_4 in order to semi-quantitatively determine the amount of CO produced with and without the addition of different amounts of Cs$^+$. The three subsequently cycles recorded are shown in Fig. E.4a-c and the first cycles are shown in the main text. The increase in the amount of CO produced over the 3 cycles for each concentration is likely due to an accumulation of CO_2 near the surface after CO oxidation. Additionally, considering a direct competition between proton and CO_2 reduction, an increase of the interfacial pH and consequent suppression of proton reduction, could lead to more CO produced.

E.2.5 CO_2 reduction in Li_2SO_4 + µM Cs$^+$

Li_2SO_4 was used as background electrolyte to investigate the effect of the Cs$^+$ concentration in the CO production. The cathodic and subsequently anodic cyclic voltammetry recorded can be seen in Fig. E.5.
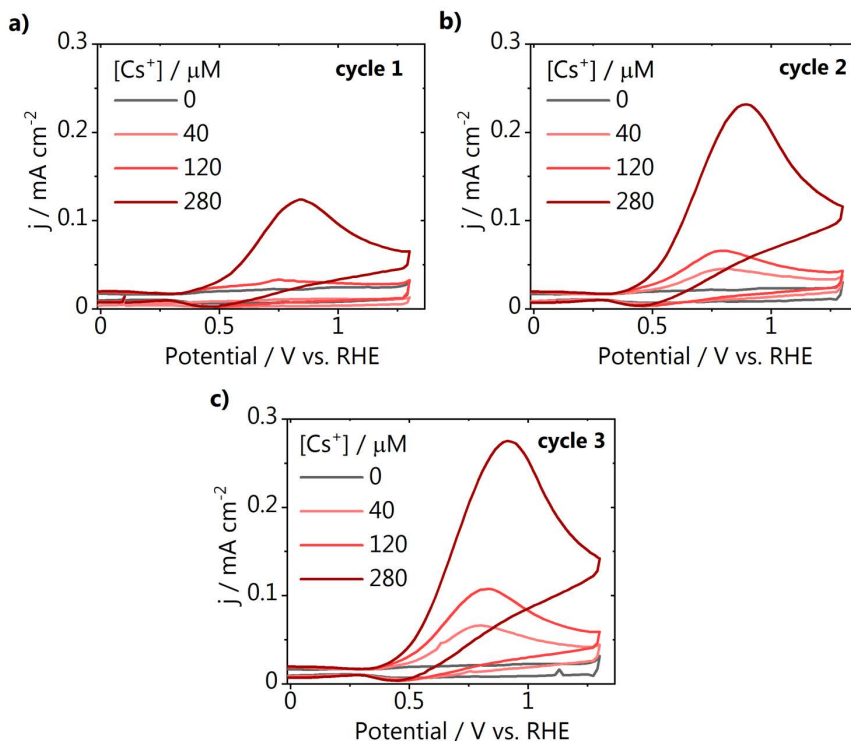
Fig. E.4. a) First, **b)** second and **c)** third cycles recorded at 50 mV s^{-1} on a gold electrode directly after a cathodic scan in CO_2 atmosphere when different amounts of Cs^+ were added to the 1 mM H_2SO_4 electrolyte.

E.3. SECM experiments

E.3.1 Capacitive approach curve fitting

A capacitive approach in air is performed before the SECM measurements in order to determine the tip-to-surface distance. Fig. E.6 shows the Pt-UME approach curves recorded before the SECM experiments performed using the gold, silver and copper samples. The fit is shown in red.

E

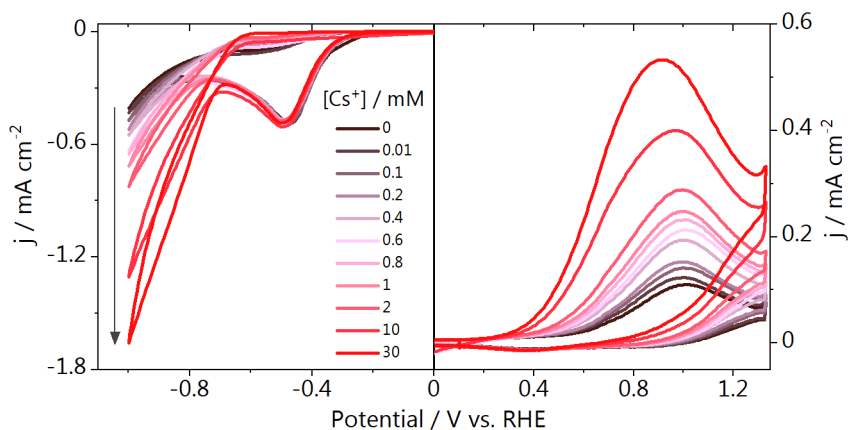**Fig. E.5.** Cyclic voltammetry recorded at 50 mV s^{-1} during CO_2 reduction on gold in Li_2SO_4 electrolyte contaning different concentrations of Cs^+. The total cation concentration in solution was kept 0.1 M and the pH = 3.
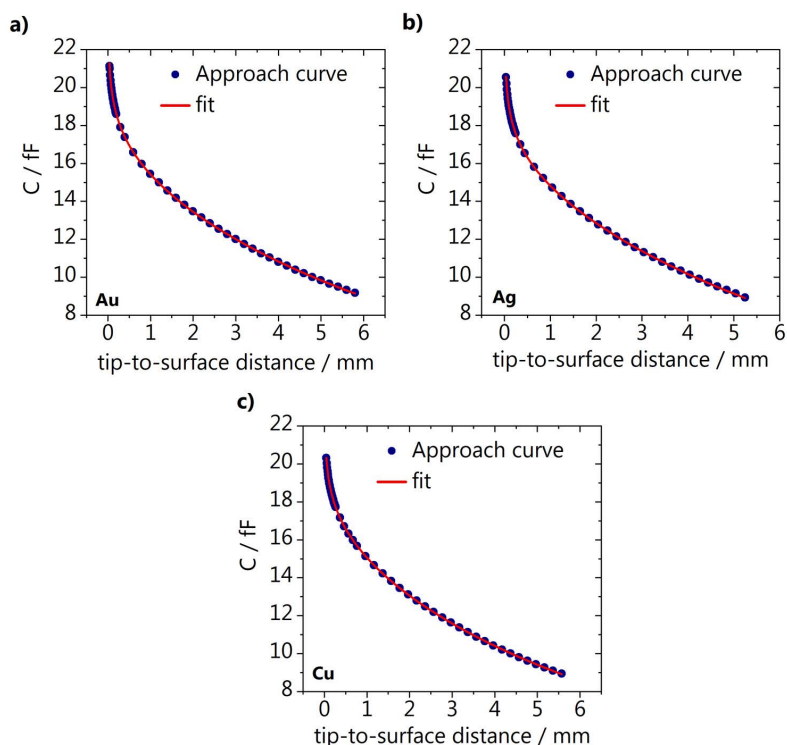

Fig. E.6. Capacitive approach curves recorded before the SECM experiments on **a)** gold, **b)** silver and **c)** copper.

E.3.2 Stability of the silver and copper electrodes

Fig. E.7 shows the instability of the silver and copper electrodes when potentials more cathodic than –0.8 and –1 V vs. RHE are applied to the sample, respectively. It shows different cycles of the Pt-UME voltammetry recorded subsequently, either after hydrogen evolution or CO_2 reduction are carried out at the sample. As can be seen in Fig. E.7a when CO_2 reduction is performed on silver in 1 mM H_2SO_4 at –1 V vs. RHE, CO is produced, at small amounts. This goes against what was observed in all the other experiments shown in the main text, in which CO_2 reduction does not take place at all without a metal ion in solution. The difference here, is that under this cathodic potential Ag^+ ions go into solution, enabling the CO_2 reduction reaction.[25] This happens as due to the SECM capacitive approach, the sample is exposed to air for a relatively long period of time, which likely leads to the formation of a very small amount of oxide. The presence of Ag^+ ions in the electrolyte can be confirmed looking at the 5th cycle recorded from the Pt-UME shown in Fig. E.7b, which presents voltammetric features characteristic of the underpotential deposition of Ag^+ on polycrystalline platinum.[26] The same happens with the copper sample when polarized more negatively than –1 V vs. RHE. Copper deposition is observed in the Pt-UME voltammetry and can be seen in Fig. E.7c.[27] These observations were made when either HER or CO_2 reduction were performed at the sample and are crucial for the correct execution and judgment of the experimental results. In between measurements, the SECM cell was always fully disassembled and thoroughly cleaned as here we observed that trace amounts of metal ions can already lead to the production of CO.

E.4. Model

An accurate density functional theory (DFT) modeling of the interaction between ions and water molecules close to the catalytic surface requires *ab initio* molecular dynamics (AIMD) simulations with a suitable number of explicit solvent molecules and a proper choice of the equilibration time. Generally, at least 4 water bilayers are required, as well as at least 10 ps of equilibration time.[13] Since platinum and gold present similar structural properties, we inherited an explicit solvation configuration equilibrated for 11 ps of AIMD on (3√3×3√3)*R*30° Pt(111) at 300 K (4 water bilayers, 72 water molecules).[13] The pre-equilibrated water molecules were inserted on top of a (3√3×3√3) *R*30° Au(111) (4 layers, 15.3 Å × 15.3 Å × 30.0 Å, 8 Å vacuum thickness) and let further equilibrate for 2 ps with time steps of 1 fs at 300 K on the gold supercell (Fig. E.8a). This system was named Au-H_2O, since it
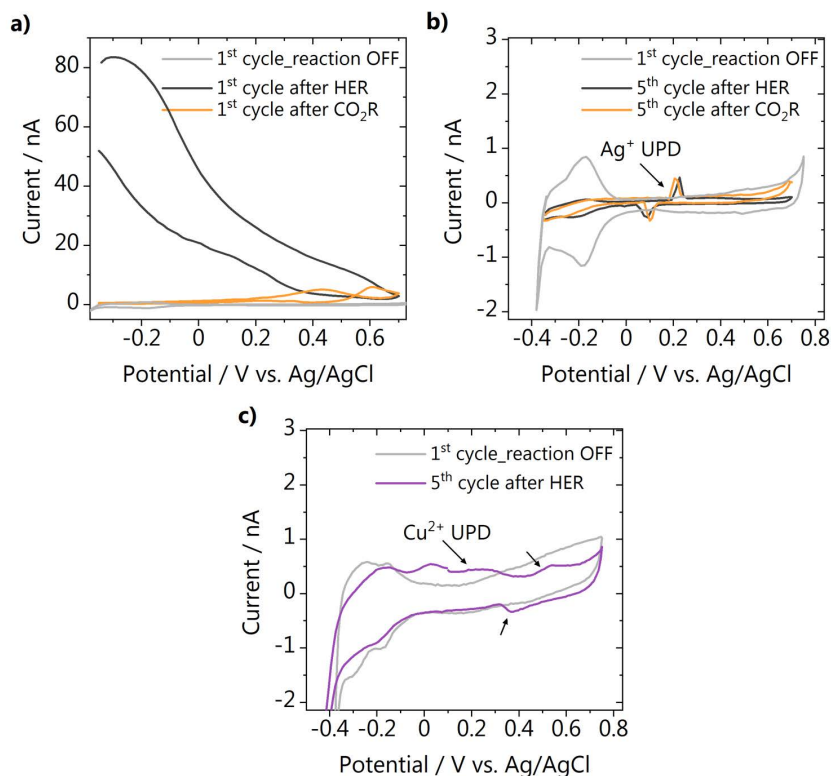
Fig. E.7. Pt-UME voltammetry **a)** after HER or CO_2 reduction are performed on silver in 1 mM H_2SO_4 and **b)** subsequent cycles from the same experiment showing the presence of Ag^+ ions in the electrolyte and **c)** similar observations on the copper electrode.

reproduces the cation-free experimental sample. After this equilibration, an alkali atom (Li, Na, K, or Cs) was inserted in a solvation cavity close to the surface (initial $d_{M\text{-surface}}$ = 3.3 Å, Fig. E.9) and the four systems were equilibrated for 2 ps at 300 K (Fig. E.8b). A hydrogen was removed from a water molecule in the fourth water bilayer, so that the +1 $|e^-|$ charge of the cation was balanced by the −1 $|e^-|$ charge of the resulting OH^-. These systems were classified as Au-H_2O-M^+ where M^+ stands for Li^+, Na^+, K^+, and Cs^+. Given the thickness of the solvation layer, around 1.4 nm, Au geometrical area, 2.0 nm², and the number of water molecules, 72, the cation surface concentration is between 0.5 (1/N_A mol of cation within V = 3.29 nm³) and 0.8 M (1/72 of water molar concentration, 55.5 M). Finally, a CO_2 molecule was inserted close to the surface for both Au-H_2O and Au-H_2O-M^+ systems, with a surface coverage of 0.04 ML (1 molecule for 27 Au surface atoms), as shown in Fig. E.8c. Upon interaction with solvation molecules and cation during 2 additional ps

at 300 K, CO_2 adsorbed on the surface *via* a $\eta^2_{C,O}$ conformation (bidentate through carbon and one oxygen) and the second oxygen coordinated to the alkali cation or to water molecules through H-bonds. These final systems were labelled Au-H_2O-CO_2 and Au-H_2O-M^+-CO_2.

E.4.1 Cation-water radial distribution functions

Cation-water radial distribution functions, $g_{M^+\text{-}H2O}(r)$ were obtained for the 2 ps equilibration of the Au-H_2O-M^+ systems to account for the density of water molecules around the alkali metal center, M^+. We first calculated the distribution of distances, $\eta(r)$, defined as the number of H_2O oxygens at a distance between r and $r + \Delta r$ for all the molecular dynamics steps, where r is the position vector from the central cation and Δr is its differential. We then normalized $\eta(r)$ for the expected surface density of cations ρ corresponding to 2D annulus formed by the solvation layer, Eq. E.6:

$$g(r)_{2D} = \frac{\eta(r)}{2\pi r \cdot \Delta r \cdot \rho}$$

Eq. E.6

where $g(r)$ is the radial distribution function (dimensionless), $\eta(r)$ the distribution of distances (dimensionless), r the position vector, Δr its differential (both in Å), and ρ the cation surface density (Å^{-2}). Cation-water radial distribution functions are reported in Fig. E.10 and the parameters of the Lorentzian fit on the first solvation shell peaks are shown in Table E.1. A Lorentzian fit was applied through Eq. E.7 and it was preferred to a Gaussian fit since it was numerically more stable:

$$g(r) = g(r)_0 + \left(\frac{2A}{\pi}\right) \cdot \left(\frac{w}{4(r-d_{M^+\text{-}O})^2 + w^2}\right)$$

Eq. E.7

where $g(r)$ is the radial distribution function, r the position vector (Å), w the full width at half maximum (Å), $d_{M^+\text{-}O}$ the cation-oxygen bond length (Å), whilst $g(r)_0$ (dimensionless) and A (Å) are fit parameters.

For larger alkali cations, the first solvation shell becomes softer as indicated by the broadening of the first $g_{M^+\text{-}H2O}(r)$ peak and the increase of w (Table E.1). For Cs^+ the transition between first, second, and third solvation shell is continuous, therefore this alkali metal can easily modify its coordination. The parameters of the Lorentzian fit (dashed lines) and the consequent estimation of the cation-oxygen distances in the first solvation shell are reported in Table E.1 and agree with previous experimental and theoretical reports.[28,29] The cation-oxygen bond length ($d_{M^+\text{-}O}$) and its associated uncertainty are obtained from the fit parameters on the $g(r)$ first

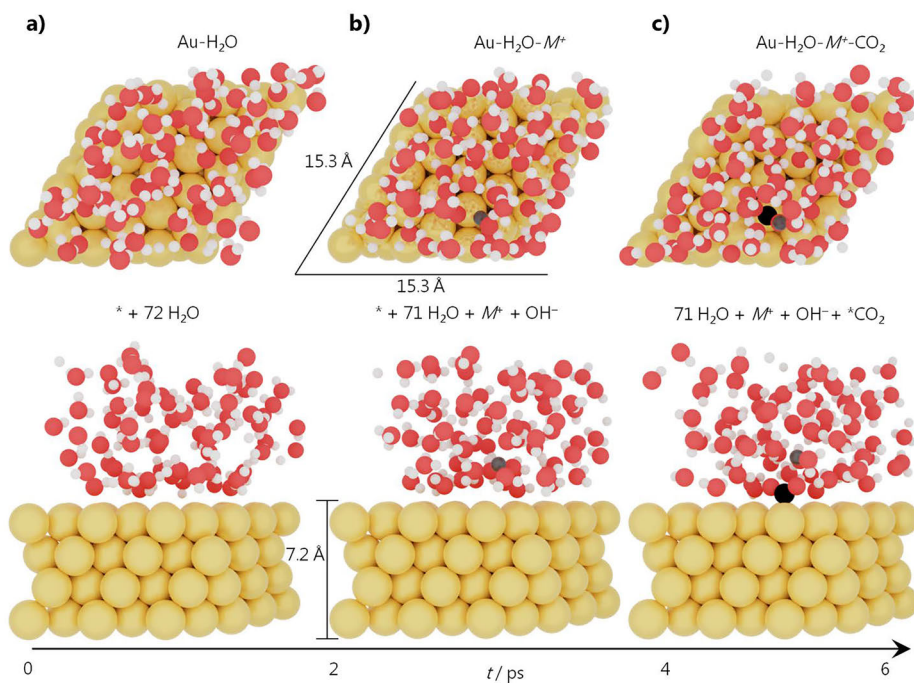peaks. The term $d_{M^+-O(S.A.)}$ stands for averages of state-of-the-art values for cation-water distances.[28,29]

Fig. E.8. Input models for *ab initio* molecular dynamics simulation carried out on a $(3\sqrt{3}x3\sqrt{3})R30°$ Au(111) supercell (15.3 Å x 15.3 Å x 30.0 Å) with 72 water molecules. **a)** The Au-H_2O system equilibrated for 2 ps (1 fs time step) at 300 K. **b)** Insertion of an alkali cation (Li^+, Na^+, K^+, Cs^+) close to the surface and equilibration for another 2 ps at 300 K. **c)** Addition of a CO_2 molecule to the system, that interacts with the gold surface *via* a $\eta^2_{C,O}$ conformation with one oxygen coordinated to the alkali cation, and AIMD further carried out for 2 ps at 300 K. The portrayed cation is Li^+.
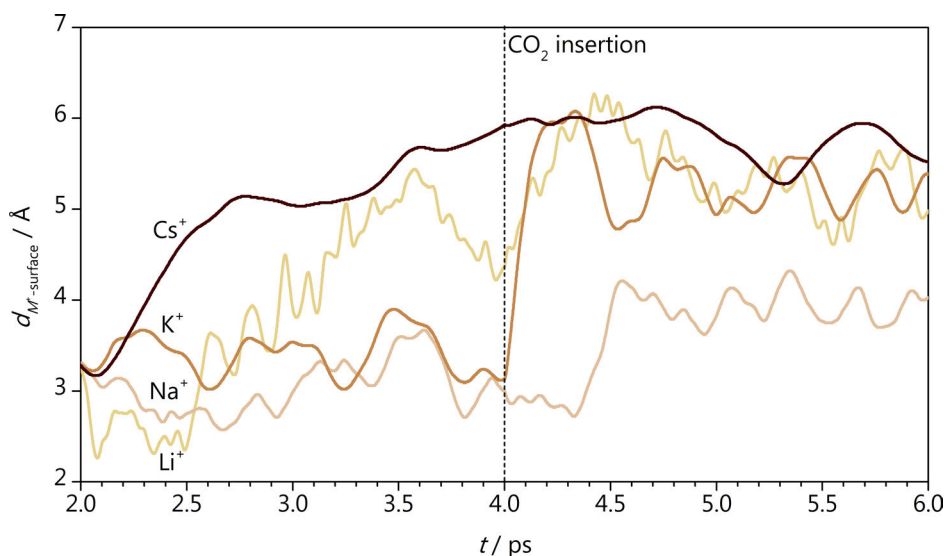
Fig. E.9. Distance between cation (M^+) and surface calculated during equilibration of the Au-H_2O-M^+ system (from 2 to 4 ps) and upon insertion of CO_2 in the vicinity of the cation (from 4 to 6 ps).
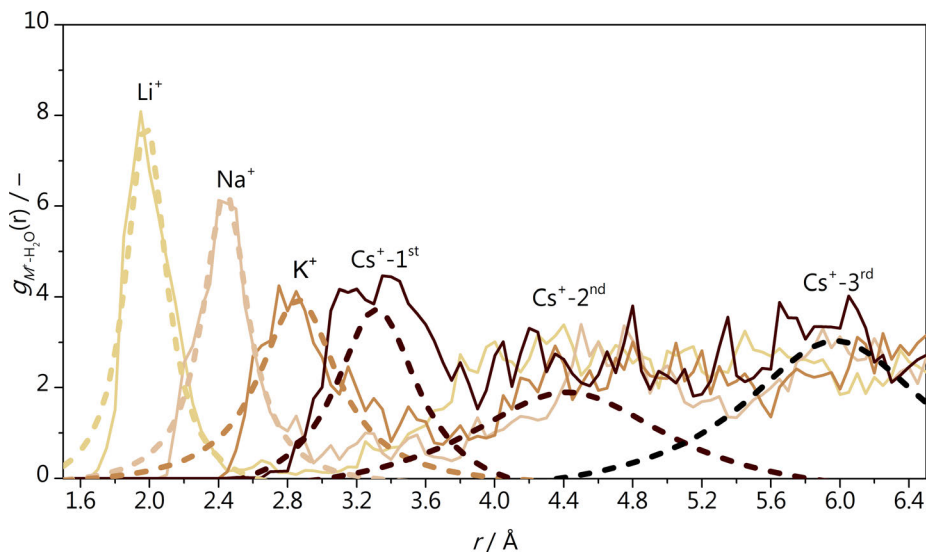

Fig. E.10. Cation solvation shells during 2 ps equilibration of the Au-H_2O-M^+, described by the cation-water radial distribution functions.

Table E.1. Parameters of the Lorentzian fit and distances between cation and water molecules in the first solvation shell, estimated from the position of the first peak of cation-water radial distribution functions, Fig. E.10. $g(r)_0$, A, w(Å), χ^2_v and $d_{M+\text{-O}}$ (Å) are fit parameters with the associated fit uncertainties. The state-of-the-art values for cation-water distances, $d_{M+\text{-O(S.A.)}}$ (Å), and associated uncertainties are taken from Ref. 9.

M^+	$g(r)_0$ / −	A / Å	w / Å	χ^2_v / −	$d_{M+\text{-O}}$ / Å	$d_{M+\text{-O(S.A.)}}$ / Å
Li$^+$	−0.39 ± 0.16	3.7 ± 0.3	0.28 ± 0.02	0.34	1.981 ± 0.007	2.08 ± 0.07
Na$^+$	−0.22 ± 0.08	3.3 ± 0.2	0.32 ± 0.02	0.12	2.440 ± 0.005	2.36 ± 0.06
K$^+$	−0.22 ± 0.12	3.6 ± 0.4	0.55 ± 0.06	0.22	2.86 ± 0.02	2.80 ± 0.08
Cs$^+$-1st	−0.53 ± 0.12	3.9 ± 0.6	0.58 ± 0.07	0.21	3.32 ± 0.02	3.14 ± 0.08
Cs$^+$-2nd	−0.53 ± 0.12	6 ± 2	1.5 ± 0.4	0.21	4.42 ± 0.08	−
Cs$^+$-3rd	−0.53 ± 0.12	7 ± 2	1.3 ± 0.4	0.21	5.97 ± 0.06	−

E.4.2 Cation coordination number

To obtain the coordination number $N_{M+\text{-O}}$ of the alkali cations M^+, we assigned a bond value equal to one if the cation-oxygen distance $r_{M+\text{-O}}$ was equal or lower than the cation-oxygen bond length $d_{M+\text{-O}}$, Table E.1. Otherwise, the bond value was set to zero if $r_{M+\text{-O}}$ was larger than a certain threshold $th_{M+\text{-O}}$: 2.5, 3.0, 3.5, 4.0 Å for Li$^+$, Na$^+$, K$^+$, and Cs$^+$, respectively (Fig. E.10). Between these extremes, $N_{M+\text{-O}}$ was calculated through Eq. E.8 following a decay controlled by the error function (erf), Eq. E.9.[30] In Eq. E.8, $N_{M+\text{-O}}$ is the cation coordination number (dimensionless), $r_{M+\text{-O}}$ is the cation-oxygen distance (Å), $d_{M+\text{-O}}$ the cation-oxygen bond length (Å), $th_{M+\text{-O}}$ the cation-oxygen threshold (Å) and avg stands for average. In Eq. E.9, t (dimensionless) is the variable of integration and 0 and z represent the integration limits.

$$N_{M+\text{-O}} = \frac{1}{2} - \frac{1}{2}\text{erf}\left(\frac{r_{M+\text{-O}} - \text{avg}(d_{M+\text{-O}}, th_{M+\text{-O}})}{0.2\ \text{Å}}\right) \qquad \text{Eq. E.8}$$

$$\text{erf}(z) = \frac{2}{\sqrt{\pi}}\int_0^z \exp(-t^2)\,dt \qquad \text{Eq. E.9}$$

E.4.3 Cation-induced electric field

We estimated the cation-induced electric field following a similar procedure as introduced by Chen et al.[31] First, we calculated the electrostatic potential induced by the cation upon removal of the CO_2 intermediate through Eq. E.10, where $U_{surf+solv+ion}$, $U_{surf+solv}$, U_{ion} indicate the electrostatic potential for the overall system (surface, solvation and ion), the environment (surface and solvation), and the ion alone respectively. Then, assuming the cation as a point charge, we define the local electric field E_{el} through Eq. E.11, where $U(r)$ is the cation-induced electrostatic

potential difference at a given coordinate $\vec{r}$. $\vec{r}_{ads}$ and $\vec{r}_{M+}$ represent the adsorbate and cation positions, respectively. The additional negative sign is introduced to assess the electric field induced on a negatively charged adsorbate, such as $*CO_2^-$.

$$U(\vec{r}) = U_{surf+solv+ion} - U_{surf+solv} - U_{ion} \qquad \text{Eq. E.10}$$

$$-\vec{E}_{el} = -\left(-\frac{U(\vec{r}_{ads}) - U(\vec{r}_{M+})}{\|\vec{r}_{ads} - \vec{r}_{M+}\|}\right)\hat{r} \qquad \text{Eq. E.11}$$

We calculated the local electric field around the $*CO_2^-$ adsorbate for different cation configurations over the last 1 ps of AIMD simulation. We applied Eq. E.10 to estimate $\vec{E}_{el}$ at the position of C, O_1, and O_2 and then we plotted the averaged value versus the average between cation-(C, O_1, O_2) distances and cation-water coordination numbers. The electric field distribution is affected by both d(M^+,{C,O_1,O_2}) and the instantaneous coordination number $N(M^+-O(H_2O))$ and highest intensities are reported for low cation-water coordination numbers and short distances, in agreement with a recent theoretical characterization for electrochemical CO_2 reduction on gold.[32]

Table E.2. Cation coordination numbers to oxygen atoms in water ($N_{M+-O(H2O)}$) and CO_2 ($N_{M+-O(CO2)}$) in presence and absence of adsorbed CO_2 as calculated through Eq. E.8. Cation coordination to water molecules or CO_2 was calculated for Au-H_2O-M^+ and Au-H_2O-M^+-CO_2 during 2 ps AIMD at 300 K. Coordination numbers are reported as averages with their associated standard deviation $\sigma(N_{M^+-O})$, median, maximum, and minimum values.

M^+	$N_{M+-O(H2O)}$ (Au-H_2O-M^+)				$N_{M+-O(H2O)}$ (Au-H_2O-M^+-CO_2)				$N_{M+-O(CO2)}$ (Au-H_2O-M^+-CO_2)			
	Mean	Median	Max	Min	Mean	Median	Max	Min	Mean	Median	Max	Min
Li^+	2.8 ± 0.8	2.9	3.9	0.3	3.2 ± 0.5	3.3	3.9	1.8	0.1 ± 0.3	0.0	1.0	0.0
Na^+	3.2 ± 0.5	3.0	4.7	2.1	2.3 ± 0.4	2.3	3.0	1.2	0.9 ± 0.2	1.0	1.0	0.0
K^+	3.5 ± 0.9	3.4	4.9	1.1	3.6 ± 0.6	3.7	4.9	1.7	0.9 ± 0.4	1.0	2.0	0.0
Cs^+	5.8 ± 1.2	5.9	8.0	2.9	5.4 ± 0.9	5.4	6.9	3.6	1.3 ± 0.5	1.1	2.0	0.0

Table E.3. Average CO_2 adsorption Gibbs free energy ΔG_{*CO2} (eV) and cation induced stabilization, $\Delta\Delta G_{*CO2}$ (eV). ΔG_{*CO2} are reported with their associated standard deviations $\sigma(\Delta G_{*CO2})$. The systems under study were Au-H_2O-CO_2 and Au-H_2O-CO_2-M^+ equilibrated for 1 and 2 ps AIMD respectively. The explicit solvent layer includes 72 H_2O molecules. Those containing cations have a water molecule replaced by M^+OH.

System	ΔG_{*CO2} / eV	$\Delta\Delta G_{*CO2}$ / eV
H_2O	+0.80 ± 0.18	−
Li^+	+0.16 ± 0.24	−0.64
Na^+	+0.28 ± 0.18	−0.53
K^+	+0.41 ± 0.12	−0.39
Cs^+	+0.23 ± 0.21	−0.58

Table E.4. Average CO_2 adsorption Gibbs free energy ΔG_{*CO2} (eV), CO_2 activation angle α (degrees), Bader charges for CO_2 intermediate and cation M^+, either coordinated to CO_2 or in the reference system (CO_2 removed), reported in elementary charge ($|e^-|$) and net CO_2 surface normal electric dipole moment $\vec{p}$ reported in $|e^-|$Å. Uncertainties are given as the standard deviation of the data. For cation Bader charges, $\Delta q \leq 0.01\ |e^-|$.

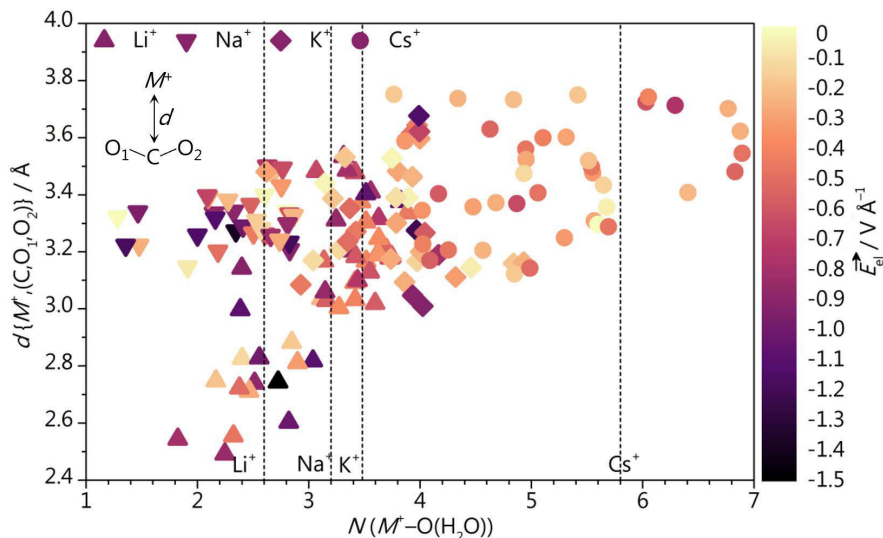| System	ΔG_{*CO2} / eV	α / °	q_{CO2} / $|e^-|$	$q_{M+(CO2)}$ / $|e^-|$	$q_{M+(ref)}$ / $|e^-|$	$\vec{p}_{CO2}$ / $|e^-|$Å
H_2O	+0.80 ± 0.18	137 ± 5	−0.47 ± 0.10	−	−	+0.40 ± 0.09
Li^+	+0.16 ± 0.24	133 ± 5	−0.67 ± 0.08	−0.91	−0.90	+0.66 ± 0.11
Na^+	+0.28 ± 0.18	134 ± 5	−0.65 ± 0.08	−0.91	−0.90	+0.54 ± 0.08
K^+	+0.41 ± 0.12	136 ± 3	−0.58 ± 0.09	−0.91	−0.90	+0.54 ± 0.09
Cs^+	+0.23 ± 0.21	131 ± 4	−0.71 ± 0.08	−0.91	−0.91	+0.65 ± 0.13

Fig. E.11. Cation-induced electric field as a function of the cation-water coordination number, $N(M^+–O(H_2O))$, (horizontal axis) and the average between cation-(C,O_1,O_2) distances (vertical axis) for different AIMD configurations. ▲, ▼, ◆, and ● represent Li^+, Na^+, K^+, and Cs^+ respectively. Dashed lines represent average cation-water coordination numbers and are taken from Table E.2.

E.4.4 Electric dipole effects

Intermediates with large electric dipole moments are affected by electrostatic fields across the electrical double layer (EDL), and their Gibbs free energy of adsorption changes according to Eq. E.12.[33] Thus, the stabilization (or destabilization) of adsorbates depends on their net electric dipole moment $\vec{p}$ and their relative orientation with respect to the electric field $\vec{E}_{el}$ within the EDL. The electric field is caused by the electric potential U applied to the electrode with respect to its potential of zero charge U_{pzc} (+0.2 V vs. SHE for polycrystalline gold[34]), and the contribution of neighboring ions, $\vec{E}_{el-ion}$, which is in the order of 1 V Å^{-1}.[18,31] In Eq. E.12 d stands for the thickness of the EDL, which is usually assumed around 3 Å.[19,31,33]

$$\Delta G = +\vec{p} \cdot \vec{E}_{el} = +\vec{p} \cdot \left(\frac{U-U_{pzc}}{d}\hat{z} + \vec{E}_{el-ion}\right)$$ Eq. E.12

Given the electric dipole moments calculated for adsorbed CO_2 (Table E.4), we estimated that the stabilization for CO_2^- adsorption due to dipole/electric field interactions adds up to 0.6 eV in the presence of a partially desolvated neighboring

cation ($\vec{E}_{el}$ = 1 V Å^{-1}, Fig. E.12). These values agree with the change in the Gibbs free energy of adsorption for CO_2^- due to cation-CO_2 interaction (Fig. 8.7 in Chapter 8). In the absence of a cation, a cathodic potential as negative as –3.0 V vs. RHE is required to induce an equivalent electric field. Therefore, under standard CO_2 reduction conditions the cation is key to open the reduction reaction pathway *via* explicit ionic bond with negatively charged intermediate and explicit, short-range dipole/cation-induced electric field effect.
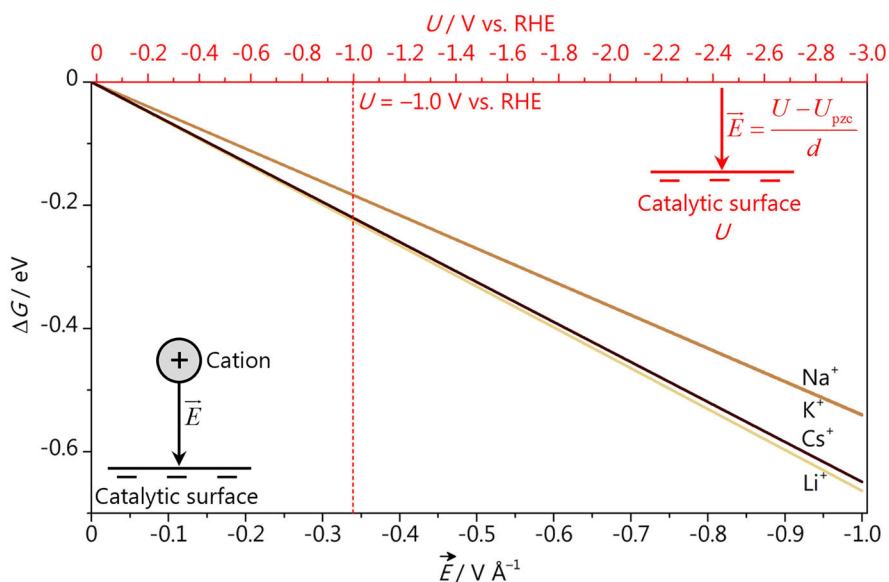

Fig. E.12. Stabilization of CO_2 adsorption due to the interaction between CO_2 dipole moment and local electric field generated by the cation (bottom axis, inset on the left). Top *x*-axis (red, inset on the right) reports the cathodic potential needed to achieve an equivalent electric field in absence of cation, according to Eq. E.12 and assuming an EDL thickness, *d*, of 3 Å.[19,31,33] Red dashed line indicates the potential applied during the study of CO production vs. Cs$^+$ concentration on gold (Fig. 8.2 in Chapter 8).

References

(1)   Monteiro, M. C. O.; Koper, M. T. M. *Electrochim. Acta* 2019, *325*, 134915.

(2)   Do, U. P.; Seland, F.; Johannessen, E. A. *J. Electrochem. Soc.* 2018, *165* (5), H219–H228.

(3)   Monteiro, M. C. O.; Jacobse, L.; Touzalin, T.; Koper, M. T. M. *Anal. Chem.* 2020, *92* (2), 2237–2243.

(4)   Jacobse, L.; Raaijman, S. J.; Koper, M. T. M. *Phys. Chem. Chem. Phys.* 2016, *18* (41), 28451–28457.

(5)   Kresse, G.; Furthmüller, J. *Phys. Rev. B* 1996, *54*, 11169–11186.

(6)   Kresse, G.; Furthmüller, J. *Comput. Mater. Sci.* 1996, *6*, 15–50.

(7)   Perdew, J. P.; Burke, K.; Ernzerhof, M. *Phys. Rev. Lett.* 1996, *77*, 3865–3868.

(8)   Grimme, S. *J. Comput. Chem.* 2006, *27*, 1787–1799.

(9)   Bucko, T.; Hafner, J.; Lebègue, S.; Ángyán, J. G. *J. Phys. Chem. A* 2010, *114*, 11814–11824.

(10)   Almora-Barrios, N.; Carchini, G.; Błoński, P.; López, N. *J. Chem. Theory Comput.* 2014, *10*, 5002–5009.

(11)   Blöchl, P. E. *Phys. Rev. B* 1994, *50*, 17953–17979.

(12)   Kresse, G.; Joubert, D. *Phys. Rev. B* 1999, *59*, 1758–1775.

(13)   Bellarosa, L.; García-Muelas, R.; Revilla-López, G.; López, N. *ACS Cent. Sci.* 2016, *2* (2), 109–116.

(14)   Marx, D.; Hutter, J. Cambridge University Press, 2009.

(15)   Nosé, S. *J. Chem. Phys.* 1984, *81*, 511–519.

(16)   Hoover, W. G. *Phys. Rev. A* 1985, *31*, 1695–1697.

(17)   Makov, G.; Payne, M. *Phys. Rev. B* 1995, *51*, 4014–4022.

(18)   Resasco, J.; Chen, L. D.; Clark, E.; Tsai, C.; Hahn, C.; Jaramillo, T. F.; Chan, K.; Bell, A. T. *J. Am. Chem. Soc.* 2017, *139* (32), 11277–11287.

(19)   Nørskov, J. K.; Rossmeisl, J.; Logadottir, A.; Lindqvist, L.; Kitchin, J. R.; Bligaard, T.; Jónsson, H. *J. Phys. Chem. B* 2004, *108* (46), 17886–17892.

(20)   Haynes, W. M. 95th ed.; CRC Press: New York, 2014.

(21)   Lide, D. R. 84th ed.; Lide, D. R., Ed.; CRC Press, 2003; Vol. 85.

(22)   Álvarez-Moreno, M.; de Graaf, C.; López, N.; Maseras, F.; Poblet, J. M.; Bo, C. *J. Chem. Inf. Model.* 2015, *55* (1), 95–103.

(23)   Dattila, F. *ioChem-BD* 2021, DOI 10.19061/iochem-bd-1-194.

(24)   Monteiro, M. C. O.; Jacobse, L.; Koper, M. T. M. *J. Phys. Chem. Lett.* 2020, *11* (22), 9708–9713.

(25)   Henckel, D. A.; Counihan, M. J.; Holmes, H. E.; Chen, X.; Nwabara, U. O.; Verma, S.; Rodríguez-López, J.; Kenis, P. J. A.; Gewirth, A. A. *ACS Catal.* 2021, *11* (1), 255–263.

(26)   Macao, L. H.; Santos, M. C.; Machado, S. A. S.; Avaca, L. A. *J. Chem. Soc. - Faraday Trans.* 1997, *93* (22), 3999–4003.

(27)   Lukaszewski, M.; Soszko, M.; Czerwiński, A. *Int. J. Electrochem. Sci.* 2016, *11* (6), 4442

(28)   Waegele, M. M.; Gunathunge, C. M.; Li, J.; Li, X. *J. Chem. Phys.* 2019, *151* (16), 160902.

(29)   Marcus, Y. *Chem. Rev.* 1988, *88* (8), 1475–1498.

(30)   Dattila, F.; García-Muelas, R.; López, N. *ACS Energy Lett.* 2020, *5*, 3176–3184.

(31)   Chen, L. D.; Urushihara, M.; Chan, K.; Nørskov, J. K. *ACS Catal.* 2016, *6* (10), 7133–7139.

(32)   Zhu, Q.; Wallentine, S.; Deng, G.; Baker, L. R. 2021, DOI: 10.26434/chemrxiv.14410655

(33)   McCrum, I. T.; Bondue, C. J.; Koper, M. T. M. *J. Phys. Chem. Lett.* 2019, *10* (21), 6842–6849.

(34)   White, R. E.; Bockris, J. O.; Conway, B. E. Kluwer Academic Publishers, 2002.

E

F

Methods and supporting information to Chapter 9

F.1 Methods

F.1.1 Electrode preparation

Gold disc electrodes were cut from a polycrystalline gold foil (0.5 mm thick, MaTecK, 99.995%) and prepared by polishing and flame annealing according to the procedure we have previously described.[1] The gold electrode cleanliness was assured by Scanning Electron Microscopy (SEM) performed using an Apreo SEM (ThermoFisher Scientific). Micrographs were obtained using an acceleration voltage of 10 kV and an electron beam current of 0.4 nA. Additionally, elemental analysis of the surface composition was performed using Energy Dispersive X-Ray Spectrometry (EDX) (Oxford Instruments X-Max^N 150 Silicon Drift detector). The EDX data was processed using the Pathfinder™ X-ray Microanalysis software v1.3. The SEM micrographs and EDX spectra are shown in Fig. F.1. Establishing surface cleanliness is crucial when studying cation effects on CO_2RR and HER as we have previously shown that, for instance, polishing alumina particles can contaminate the gold surface and promote water reduction by the release of Al^{3+} ions in an acidic electrolyte.[1]

F.1.2 Materials

Appropriate amounts of the following salts were employed to prepare the electrolytes used in this work: Li_2SO_4 (Alfa Aesar, anhydrous, 99.99%, metal basis), Na_2SO_4 (Alfa Aesar, anhydrous, 99.99%, metal basis), K_2SO_4 (Sigma Aldrich, anhydrous, 99.99%, metal basis), Cs_2SO_4 (Alfa Aesar, Puratronic®, 99.997%, metals basis), $BeSO_4$ (Alfa Aesar, tetrahydrated, 99.99%, metal basis), $MgSO_4$ (Sigma Aldrich, ≥ 99.99%, trace metal basis), $Al_2(SO_4)_3$ (Sigma Aldrich, 99.99%, trace metal basis), $Nd_2(SO_4)_3$ (Sigma Aldrich, 99.99%, trace metal basis), $Ce_2(SO_4)_3$ (Sigma Aldrich, ≥ 99.99%, trace metal basis), $LiClO_4$ (Sigma Aldrich, 99.99%, trace metal basis), $CsClO_4$ (Sigma Aldrich, 99.99%, trace metal basis), $Mg(ClO_4)_2$ (American Elements, 99.99%), $Ca(ClO_4)_2$ (American Elements, tetrahydrated, 99.99%), $Ba(ClO_4)_2$ (Sigma Aldrich, 99.999%), Li_2CO_3 (Merck, 99.99%, trace metal basis), $NaHCO_3$ (Sigma Aldrich, ≥99.7%, ACS reagent), $KHCO_3$ (Sigma Aldrich, ≥99.95%, trace metal basis), Cs_2CO_3 (Merck, 99.9%, trace metal basis), H_2SO_4 (Merck, Suprapur, 96%). The carbonate and bicarbonate electrolytes were purified by long term electrolysis prior to the experiments. Two large surface area gold electrodes were used and a potential of –2 V was applied for 12 hours, similarly to the procedure reported elsewhere.[2] The pH of the electrolytes prepared was certified using a glass-

electrode pH meter (Lab 855, SI Analytics) calibrated with standard buffer solutions (Radiometer Analytical). The experiments were performed in a one-compartment, three-electrode cell with the gold working electrode in hanging meniscus configuration. The glassware used in this work was stored in potassium permanganate solution (1 g L^{-1} $KMnO_4$ dissolved in 0.5 M H_2SO_4) overnight and cleaned by immersion in dilute piranha. Subsequently, the glassware was boiled at least five times in ultrapure water (>18.2 MΩ cm, Millipore Milli-Q). A gold wire (0.8 mm thick, Mateck, 99.9%) was used as counter electrode and a reversible hydrogen electrode (RHE) or a Hydroflex (Gaskatel) as reference, connected to the cell via a Luggin capillary.

F.1.3 Electrochemical measurements

Experiments were carried out using a Bio-Logic potentiostat/galvanostat/EIS (SP-300). The gold electrode was characterized before each experiment by recording a cyclic voltammogram between 0 and 1.75 V vs. RHE in 0.1 M H_2SO_4 at 50 mV s^{-1}. The gold electrochemical surface area (ECSA) was determined by calculating the charge corresponding to the gold oxide reduction. This value was converted to ECSA using the charge density associated with the reduction of a monolayer of gold oxide (386 μC cm^{-2}).[3] Hydrogen evolution or CO_2 reduction were conducted after purging the electrolyte with either argon or CO_2 for at least 20 minutes. During the experiments, the respective gas flow was kept above the electrolyte, to avoid oxygen diffusion into the solution. Before each measurement, the solution resistance was determined by Electrochemical Impedance Spectroscopy (EIS) and the electrode potential was compensated for 85% of the ohmic drop. The potential opening CO_2 reduction experiments were performed by cycling the gold electrode from 0.1 V vs. RHE to different negative potentials and in the reverse scan up to 1.3 V vs. RHE. In between two different potential steps the electrode potential was held at 0.1 V vs. RHE for four minutes to recover from the concentration (pH) gradients developed in the diffusion layer during the cathodic scan.

F.1.4 Density functional theory modeling

Density functional theory (DFT) simulations were performed using the Vienna Ab Initio Simulation Package(VASP),[4,5] with the PBE density functional.[6] To properly account for dispersion, we applied the DFT-D2 method,[7,8] with the C_6 coefficients reparametrized from one of our groups.[9] Inner electrons were represented by PAW

pseudopotentials[10,11] and the monoelectronic states for valence electrons were expanded as plane waves with a kinetic energy cutoff of 450 eV. *Ab initio* molecular dynamics were applied on the Au/water/cation system (see Computational model) for 4 ps (1 fs time step) in a canonical NVT ensemble at 300 K regulated by a Nosé-Hoover thermostat.[12–15]. To account for the self-interaction error due to the localized f electrons of Nd^{3+}, we applied a Hubbard correction U_{eff} = 6.76 eV − 0.76 eV following the Dudarev´s approach,[16] taken from a study of electronic and magnetic properties of a Nd adatom.[17]

F.2 Experimental

F.2.1 Gold electrode characterization

Scanning Electron Microscopy (SEM) and Energy Dispersive X-Ray Spectroscopy (EDX) of the gold electrode used in this study.
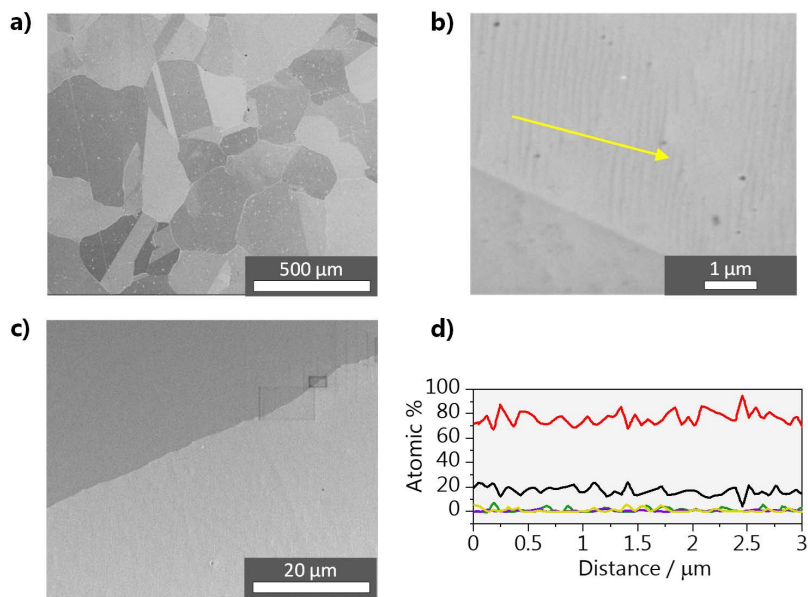
Fig. F.1. a)-c) SEM micrographs and **d)** EDX line spectra of the gold electrode (region marked with a yellow arrow) used for the experiments after polishing with diamond suspension and flame annealing. The lines refer to the following signals: ━ (black) C K, ━ (green) O K, ━ (purple) Al K and ━ (red) Au M.
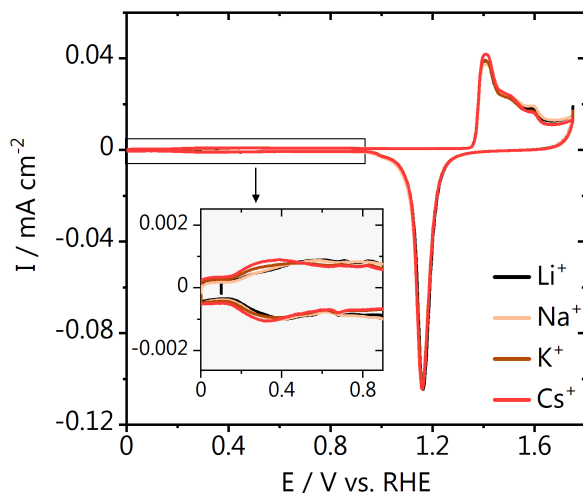
F.2.2 Potential opening experiments at pH 3 (0.1 M M_2SO_4)

Fig. F.2. Blank voltammetry of the gold electrode after flame annealing taken at 50 mV s^{-1} in 0.1 H$_2$SO$_4$.
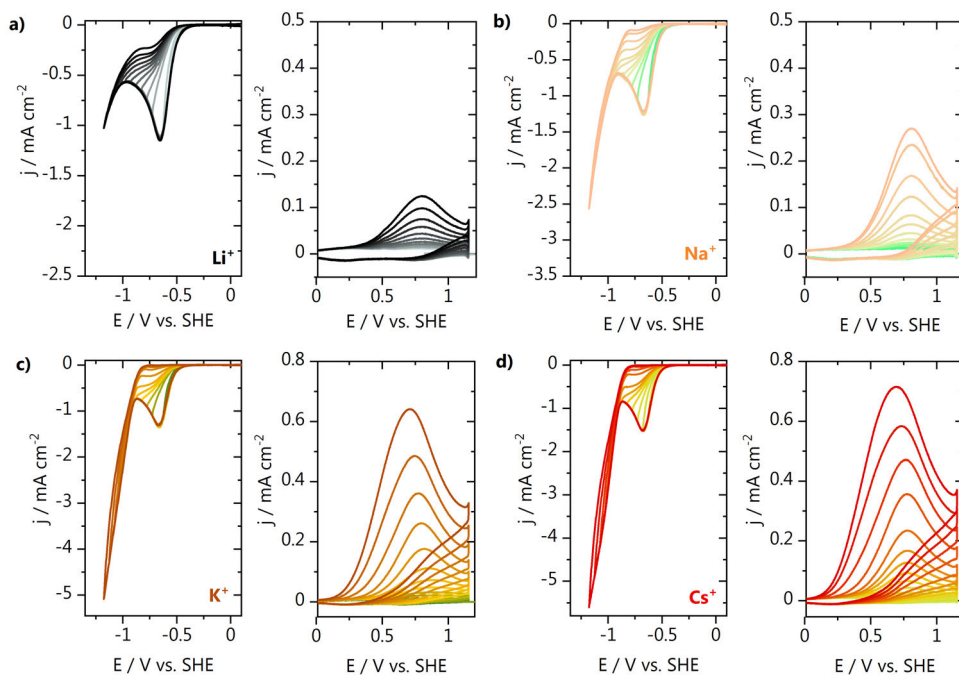

Fig. F.3. a)-d) Consecutive cathodic/anodic voltammetry of the CO_2 reduction potential opening experiments in 0.1 M M_2SO_4 with M^{n+} = Li$^+$, Na$^+$, K$^+$, Cs$^+$ at pH = 3.

F.2.3 HER and CO$_2$RR experiments at pH 6.8 (0.1 M *M*HCO$_3$)

Blank voltammetry of the gold electrode taken before the experiments performed at pH 6.8 in 0.1 M *M*HCO$_3$ electrolytes with M^{n+} = Li$^+$, Na$^+$, K$^+$ and Cs$^+$.
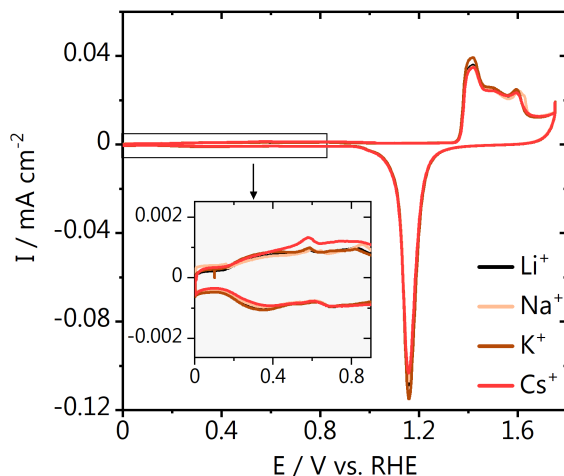

Fig. F.4. Blank voltammetry of the gold electrode after flame annealing taken at 50 mV s^{-1} in 0.1 H$_2$SO$_4$.

Similarly to our experiments in acidic media, in bicarbonate the CO produced in the cathodic scan can also be detected in the positive-going scan. The inset of Fig. F.5b, shows the CO produced after the gold electrode is polarized negatively and that the highest amount of CO is produced in the Cs$^+$ and K$^+$ electrolytes. The two peaks observed in the CO oxidation voltammetry in bicarbonate are due to diffusion limitation by two different species, namely, CO and OH$^-$, as a function of the local pH. In our previous work, we find that between pH 7 and 11, CO oxidation by water and OH$^-$ gives rise to the first and second peak observed in the voltammetry, respectively, and that the current of the second peak is diffusion limited by the OH$^-$ concentration, since it is lower than the CO concentration at this pH.[18]
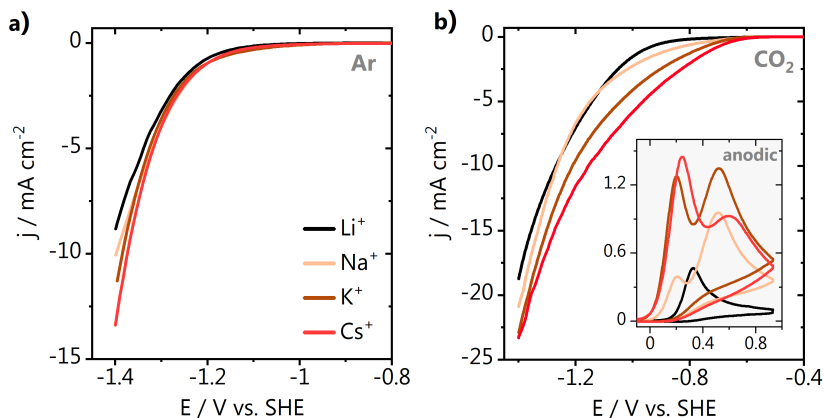
Fig. F.5. Cyclic voltammetry of **a)** water reduction and **b)** CO_2 reduction in 0.1 M MHCO$_3$, pH 9 (argon atmosphere) and pH 7 (CO_2 atmosphere).

F.2.4 Hydrogen evolution in electrolytes containing multivalent cations

Blank voltammetry of the gold electrode before the experiments performed at pH 3 in 0.1 M Li$_2$SO$_4$ + 1 mM M^{n+} electrolytes with M^{n+} = Li$^+$, Cs$^+$, Be^{2+}, Mg^{2+} , Al^{3+} , Nd^{3+} , Ce^{3+} and 0.2 M LiClO$_4$ + 2 mM M^{n+} with M = Ca^{2+}, Ba^{2+}.
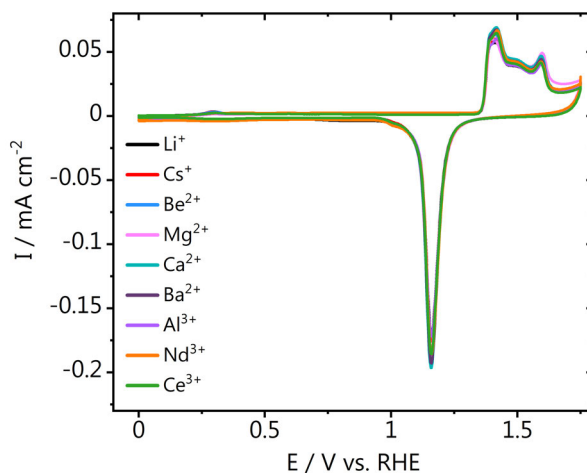

Fig. F.6. Blank voltammetry of the gold electrode after flame annealing taken at 50 mV s^{-1} in 0.1 H$_2$SO$_4$. The blank CVs were taken before the HER experiments performed in the presence of the different cations.

CVs of the gold electrode during hydrogen evolution performed at pH 3 in 0.1 M Li_2SO_4 + 1 mM M^{n+} electrolytes with M^{n+} = Li^+, Cs^+, Be^{2+}, Mg^{2+}, Al^{3+}, Nd^{3+}, Ce^{3+} and 0.2 M $LiClO_4$ + 2 mM M^{n+} with M^{n+} = Ca^{2+}, Ba^{2+}. All electrolytes were saturated with Argon prior to the measurements.
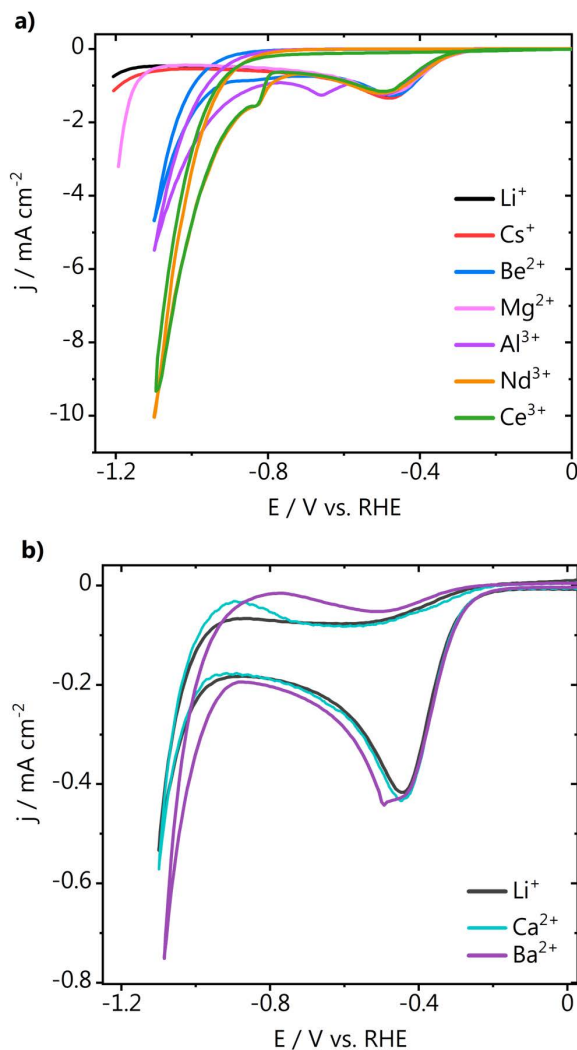

Fig. F.7. Cyclic voltammetry of HER in **a)** 0.1 M Li_2SO_4 or **b)** 0.1 M $LiClO_4$ electrolyte solutions containing different cations.

Relationship between cation acidity and Gibbs free energy of hydration.[19]
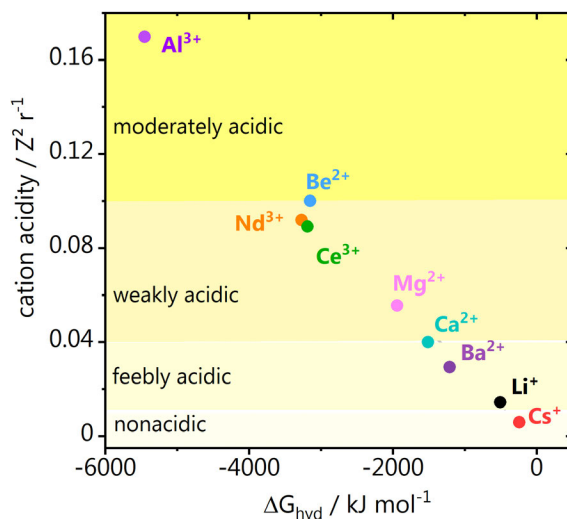

Fig. F.8. Cation acidity and Gibbs free energy of hydration for the different multivalent cations used in this work.

Fig. F.9 shows the CVs of HER and the effect of cation hydrolysis on the first and second regimes of proton reduction and on hydroxide deposition.

F.3 Density functional theory modeling

We carried out density functional theory (DFT) simulations through the Vienna Ab Initio Package (VASP).[4,5] We chose the PBE density functional[6] including dispersion through the DFT-D2 method,[7,8] with our reparametrized C_6 coefficients.[9] Inner electrons were represented by PAW pseudopotentials[10,11] and the monoelectronic states for the valence electrons were expanded as plane waves with a kinetic energy cutoff of 450 eV. Since Nd presents a localized f electron, which leads to self-interaction error, we applied a Hubbard correction U_{eff} = 6.76 eV − 0.76 eV to the Nd atom following the Dudarev's approach.[16] This value was taken from a previous computational work, where the authors assessed electronic and magnetic properties for a Nd adatom.[17]

We modeled the experimental system as in Chapter 8.[15] We employed a $3\sqrt{3}\times3\sqrt{3}$–$R30°$ Au(111) supercell, which included 4 layers with 15.3 Å × 15.3 Å lateral dimensions and overall thickness 30.0 Å (8 Å vacuum). The solvation layer accounted for 72 H_2O molecules within 15 Å and it was retrieved from our work mentioned above.[15] During that study,[15,20] the system was optimized for more than
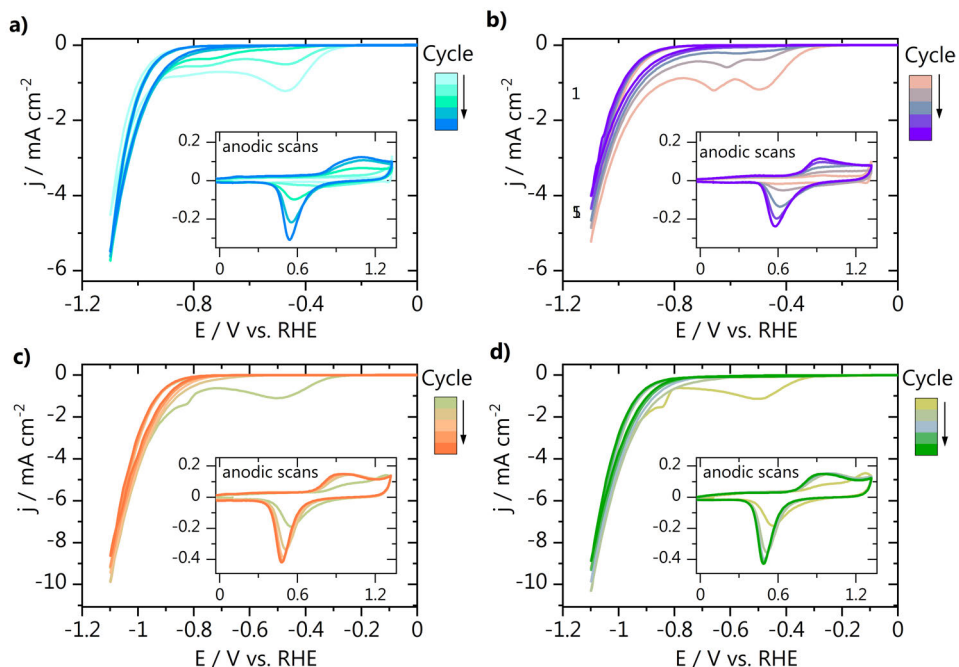
Fig. F.9. Hydrogen evolution cyclic voltammetry performed at pH 3 in 0.1 M Li_2SO_4 + 1 mM M^{n+} electrolytes with M^{n+} being **a)** Be^{2+}, **b)** Al^{3+}, **c)** Nd^{3+}, **d)** Ce^{3+}. An anodic scan recorded directly after HER is shown in the graph inset.

10 ps via AIMD simulation in a canonical NVT ensemble at 300 K regulated by a Nosé-Hoover thermostat.[12–15]. We introduced two cations M^{n+} (Li^+, Cs^+, Mg^{2+}, Ba^{2+}, Al^{3+}, Nd^{3+}) within the first solvation layer, whilst we removed $2n$ hydrogens from water molecules in the fourth water bilayer to keep charge balance (n = cation charge). Considering the thickness of the solvation layer (1.4 nm), the geometrical area (2.0 nm^2) and the overall number of solvent molecules (72), a cation surface coverage of 0.08 ML (2/27) is equivalent to a surface concentration between 1.0 ($2/N_A$ mol within a volume of 3.29 nm^3) and 1.6 M (2/72 of water molar concentration, 55.5 M). Besides, to better mimic explicit electrostatic effects, we applied an electric field of –0.3 V $Å^{-1}$,[9,21] equivalent to a potential of –0.9 V vs. potential of zero charge (U_{PZC}), assuming an electrical double layer thickness of 3 Å.[22,23] Since the U_{PZC} for polycrystalline gold is reported as +0.2 V vs SHE,[24] the applied electric field is equivalent to an electric potential of –0.7 V vs. SHE, Eq. F.1.

$$U \text{ (vs. SHE)} = U_{PZC} + \vec{E}_{EDL} \cdot d_{EDL}$$

Eq. F.1

The Au/water/cation systems underwent 2 ps of AIMD simulations. Finally, we added either a CO_2 or an additional water molecule (0.04 ML, 1/27) to the equilibrated Au/water and Au/water/cations model, which adsorbed on the surface close to one of the cations. Besides, to check a reference case with proton as the cation, we replaced the 2 optimized Li^+ atoms in the $Au/H_2O/Li^+$ systems with H^+. The resulting 6 Au/water/M^{n+}/*ads* and 1 Au/water/H^+/*ads* systems (*ads* = *CO_2, *H_2O) were further optimized for 2 ps to assess the activation of CO_2 and H_2O in the presence and absence of a metal cation. Since cations, adsorbates CO_2, and the explicit solvation later were placed only on one side of the slab, we applied an additional dipole correction to remove spurious contributions arising from the asymmetric slab model.[25]

F.3.1 Cation-water radial distribution functions

We obtained the cation-water radial distribution functions, $g_{M^{n+}-H2O}(r)$ from the 2 ps equilibration of the Au/water/M^{n+} systems to estimate the density of water molecules around the two M^{n+} centers introduced in the supercell. First, we calculated the distribution of distances of H_2O oxygens from the cation, $\eta(r)$, defined for all the molecular dynamics steps within an interval $(r, r + \Delta r)$, where r is the position vector from M^{n+} and Δr is its differential. We then normalized $\eta(r)$ for the surface density of cations ρ corresponding to 2D annulus formed by the solvation layer, Eq. F.2.

$$g(r)_{2D} = \frac{\eta(r)}{2\pi r \cdot \Delta r \cdot \rho}$$

Eq. F.2

In Eq. F.2, $g(r)$ is the radial distribution function (dimensionless), $\eta(r)$ the distribution of distances (dimensionless), r the position vector, Δr its differential (both in Å), and ρ the cation surface density (Å^{-2}). Cation-water radial distribution functions are reported in Fig. F.10 and the parameters of the Lorentzian fit on the first solvation shell peaks are shown in Table F.1. A Lorentzian fit was applied through Eq. F.3, as in Ref. 15.

$$g(r) = g(r)_0 + \left(\frac{2A}{\pi}\right) \cdot \left(\frac{w}{4(r-d_{M-O})^2 + w^2}\right)$$

Eq. F.3

where $g(r)$ is the radial distribution function, r the position vector (Å), w the full width at half maximum (Å), d_{M+-O} the cation-oxygen bond length (Å), whilst $g(r)_0$ (dimensionless) and A (Å) are fit parameters. The parameters of the Lorentzian fit

and the resulting estimation of the cation-oxygen distances in the first solvation shell are reported in Table F.1 and agree with previous experimental and theoretical reports.[26,27] The cation-oxygen bond length (d_{M-O}) and its associated uncertainty are obtained from the fit parameters on the $g(r)$ first peaks. The term $d_{M-O(S.A.)}$ stands for averages of state-of-the-art values for cation-water distances.[26,27]
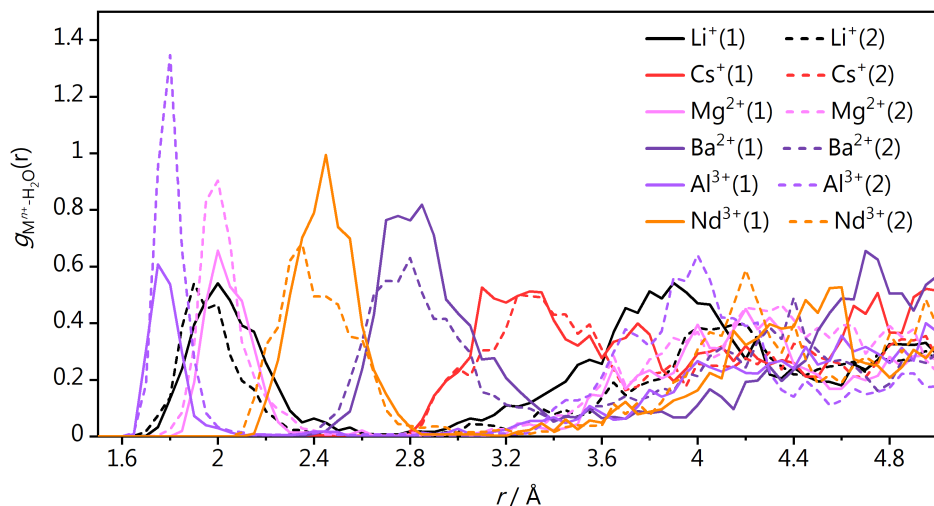

Fig. F.10. Cation solvation shells during 2 ps equilibration (0-2 ps) of the Au/water/M^{n+}, described by the cation-water radial distribution functions.

Table F.1. Parameters of the Lorentzian fit and distances between cation and water molecules in the first solvation shell, estimated from the position of the first peak of cation-water radial distribution functions, Fig. F.10, for an AIMD equilibration of 2 ps. $g(r)_0$, A, w (Å) and χ^2_v are fit parameters. Uncertainty associated with fit parameters is given as standard deviation of the data, whilst uncertainty related to averages of state-of-the-art values for cation-water distances, $d_{M-O(S.A.)}$, is taken from Ref. 26 and 27.

M^{n+}	$g(r)_0$	A / Å	w / Å	χ^2_v	d_{M-O} / Å	$d_{M-O(S.A.)}$ / Å
Li$^+$(1)	−0.030 ± 0.009	0.281 ± 0.018	0.31 ± 0.02	1.1E−03	2.021 ± 0.006	2.08 ± 0.07
Li$^+$(2)	−0.022 ± 0.008	0.206 ± 0.013	0.233 ± 0.018	1.1E−03	1.945 ± 0.005	
Cs$^+$(1)	−0.09 ± 0.02	0.35 ± 0.05	0.48 ± 0.07	3.5E−03	3.275 ± 0.017	3.14 ± 0.08
Cs$^+$(2)	−0.057 ± 0.013	0.34 ± 0.04	0.46 ± 0.05	2.7E−03	3.326 ± 0.015	
Mg^{2+}(1)	−0.031 ± 0.012	0.214 ± 0.017	0.196 ± 0.018	2.1E−03	2.028 ± 0.005	2.09 ± 0.04
Mg^{2+}(2)	−0.023 ± 0.011	0.241 ± 0.013	0.154 ± 0.010	2.0E−03	1.996 ± 0.003	
Ba^{2+}(1)	−0.028 ± 0.013	0.49 ± 0.03	0.36 ± 0.03	3.6E−03	2.826 ± 0.007	2.81
Ba^{2+}(2)	−0.025 ± 0.010	0.40 ± 0.02	0.40 ± 0.03	1.8E−03	2.798 ± 0.008	
Al^{3+}(1)	−0.012 ± 0.007	0.124 ± 0.008	0.110 ± 0.10	9.6E−04	1.772 ± 0.002	1.887 ± 0.015
Al^{3+}(2)	−0.026 ± 0.011	0.232 ± 0.011	0.102 ± 0.006	2.4E−03	1.791 ± 0.002	
Nd^{3+}(1)	−0.042 ± 0.011	0.41 ± 0.02	0.259 ± 0.015	2.4E−03	2.445 ± 0.004	2.472 ± 0.033
Nd^{3+}(2)	−0.039 ± 0.015	0.37± 0.03	0.34 ± 0.03	3.1E−03	2.384 ± 0.009	

F.3.2 Cation coordination number

To obtain the coordination number $N_{\text{M-O}}$ of the multivalent cations M^{n+}, we assigned a bond value equal to one if the cation-oxygen distance $r_{\text{M-O}}$ was equal or lower than the cation-oxygen bond length $d_{\text{M-O}}$, Table F.1. Otherwise, the bond value was set to zero if $r_{\text{M-O}}$ was larger than a certain threshold $th_{\text{M-O}}$: 2.5, 3.5, 2.4, 3.5, 2.0, 2.8 Å for Li^+, Cs^+, Mg^{2+}, Ba^{2+}, Al^{3+}, Nd^{3+} respectively (Fig. F.10). Between these extremes, $N_{\text{M-O}}$ was calculated through Eq. F.4 following a decay controlled by the error function (erf), Eq. F.5.[28] In Eq. F.4, $N_{\text{M-O}}$ is the cation coordination number (dimensionless), $r_{\text{M-O}}$ is the cation-oxygen distance (Å), $d_{\text{M-O}}$ the cation-oxygen bond length (Å), $th_{\text{M-O}}$ the cation-oxygen threshold (Å) and avg stands for average. In Eq. F.5, t *(dimensionless)* is the variable of integration and 0 and z represent the integration limits.

$$N_{\text{M-O}} = \frac{1}{2} - \frac{1}{2}\,\text{erf}\left(\frac{r_{\text{M-O}} - \text{avg}(d_{\text{M-O}}, th_{\text{M-O}})}{0.2\,\text{Å}}\right) \qquad \text{Eq. F.4}$$

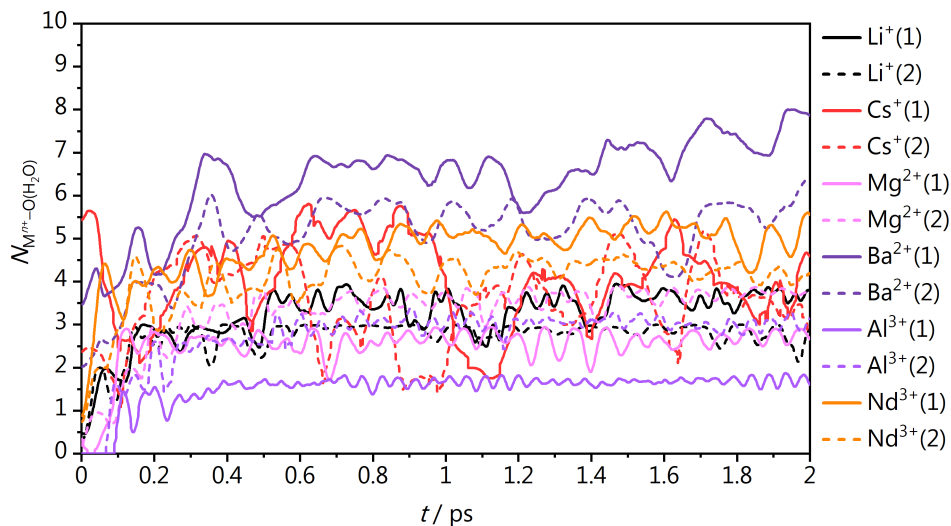$$\text{erf}(z) = \frac{2}{\sqrt{\pi}}\int_0^z \exp(-t^2)\,dt \qquad \text{Eq. F.5}$$

F

Fig. SF.11. Cation coordination numbers to oxygen atoms in water ($N_{\text{M-O(H}_2\text{O)}}$) during equilibration of the Au/water/M^{n+} system (from 0 to 2 ps).

Table F.2. Cation coordination numbers to oxygen atoms in water ($N_{\text{M-O(H}_2\text{O)}}$) as calculated through Eq. F.4 for Au/water/M^{n+} during 2 ps AIMD at 300 K (Fig. F.11). Coordination numbers are reported as averages with their associated standard deviation $\sigma(N_{\text{M-O}})$, median, maximum, and minimum values.

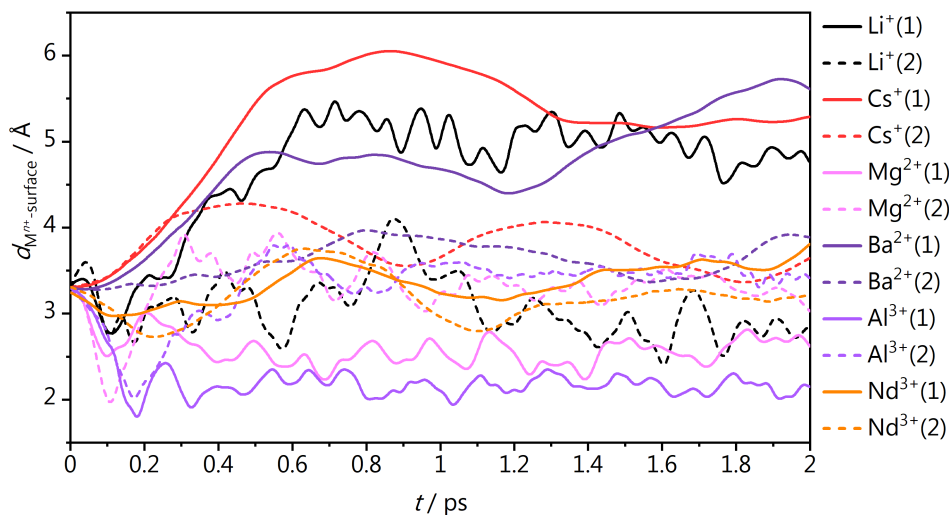| M^{n+} | $N_{\text{M-O(H}_2\text{O)}}$ (Au/water/M^{n+}) | | | |
	Mean	Median	Max	Min
Li$^+$(1)	3.5 ± 0.3	3.6	3.9	2.5
Li$^+$(2)	2.8 ± 0.2	2.9	3.0	2.1
Cs$^+$(1)	3.7 ± 0.9	3.9	5.4	1.7
Cs$^+$(2)	3.7 ± 0.7	3.7	5.2	2.0
Mg^{2+}(1)	2.6 ± 0.2	2.7	2.9	1.9
Mg^{2+}(2)	3.6 ± 0.2	3.7	3.9	3.0
Ba^{2+}(1)	6.9 ± 0.6	6.9	8.0	5.6
Ba^{2+}(2)	5.4 ± 0.5	5.6	6.5	4.1
Al^{3+}(1)	1.68 ± 0.08	1.7	1.9	1.5
Al^{3+}(2)	3.03 ± 0.14	3.1	3.3	2.4
Nd^{3+}(1)	5.1 ± 0.3	5.1	5.6	4.2
Nd^{3+}(2)	4.3 ± 0.2	4.3	4.7	3.7

Fig. F.12. Distance between cation (M^{n+}) and surface calculated during equilibration of the Au/water/M^{n+} system (from 2 to 4 ps).

### F.3.3 Cation accumulation at the Outer Helmholtz layer

To assess the thermodynamics of cation accumulation at outer Helmholtz plan (OHP), we applied the methodology introduced by Resasco et al.[29] The energy of a solvated cation at the bulk electrolyte can be referenced to the energy of the bulk metal following the principles of the Computational Hydrogen Electrode.[30] In the following lines, we define such methodology for the case of alkali cations, which can be easily generalized to multivalent species. At the standard reduction potential U^0,[31] a cation M^+ is in equilibrium with its reduced state M, Eq. F.6. Thus, we can derive the energy of the cation/electron pair at a given potential U vs SHE from the DFT energy of the bulk alkali metal, Eq. F.7.

$$M^+ + e^- \leftrightarrow M, \, U = U^0 \qquad \text{Eq. F.6}$$
$$E_{M^+ + e^-} = E_M - |e^-| \, (U - U^0) \qquad \text{Eq. F.7}$$

We can instead estimate the energy of a cation at the OHP at $U = 0$ V vs SHE from our *ab initio* molecular dynamics simulations, since we specifically inserted two metals at the OHP, which donate their valence electron to the solvation layer,

Eq. F.8. * accounts for the gold surface and the label env for the environment, i.e. the solvation layer and the second cation. Thus, we can calculate the thermodynamic driving force for one of the two cations to accumulate at the OHP as in Eq. F.9 for 50 AIMD snapshots after 1 ps equilibration (every 20 fs from 1 ps to 2 ps).

$$* + \text{env} + M \rightarrow * + \text{env} + M^+ + e^-, E_{M^+ + e^-} \text{(OHP)} \qquad \text{Eq. F.8}$$
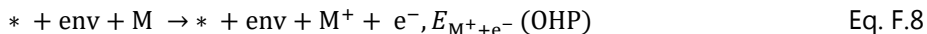
$$\Delta E = E_{M^+ + e^-}\text{(OHP)} - E_{M^+ + e^-}\text{(bulk)} \qquad \text{Eq. F.9}$$

Table F.3. Fit parameters for linear correlations shown in Fig. F.13.

$$E_{\text{OHP}} - E_{\text{bulk}} = a + b * d_{M^{n+}-\text{surface}}$$

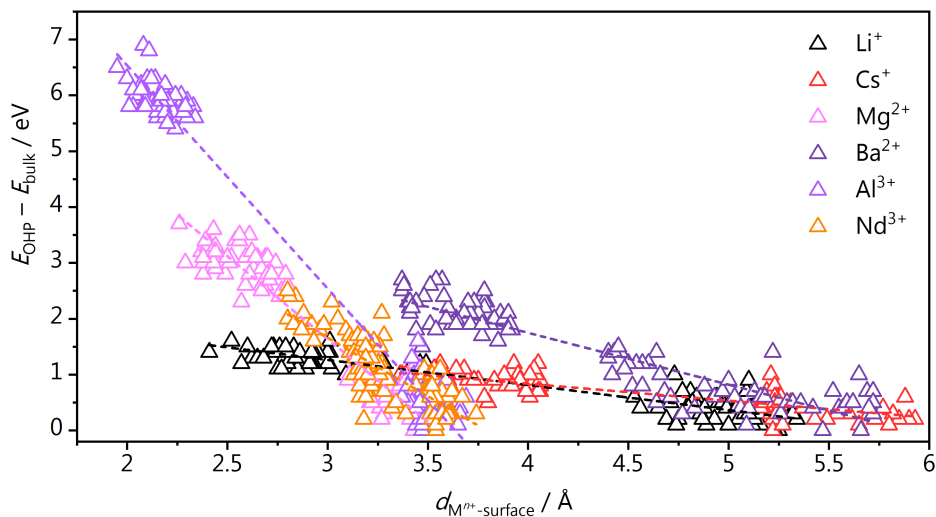| M^{n+}	a / eV	b / eV Å^{-1}	R^2
Li$^+$	+2.61 ± 0.07	−0.45 ± 0.02	0.87
Cs$^+$	+2.05 ± 0.09	−0.30 ± 0.02	0.70
Mg^{2+}	+10.5 ± 0.3	−2.97 ± 0.08	0.93
Ba^{2+}	+5.5 ± 0.2	−0.93 ± 0.04	0.84
Al^{3+}	+14.5 ± 0.2	−4.00 ± 0.06	0.98
Nd^{3+}	+8.0 ± 0.5	−2.1 ± 0.2	0.65

Fig. F.13. Correlation between the thermodynamic driving force for cation accumulation at the OHP estimated at U = 0 V versus SHE and cation-surface distance. The data points have been referenced to the minimum for each cation, respectively −2.4, −2.2, −6.7, −8.1, −11.4, −8.5 eV for Li$^+$, Cs$^+$, Mg^{2+}, Ba^{2+}, Al^{3+}, and Nd^{3+}. All the data points are therefore negative, confirming that cation accumulation at the OHP is an exothermic process.
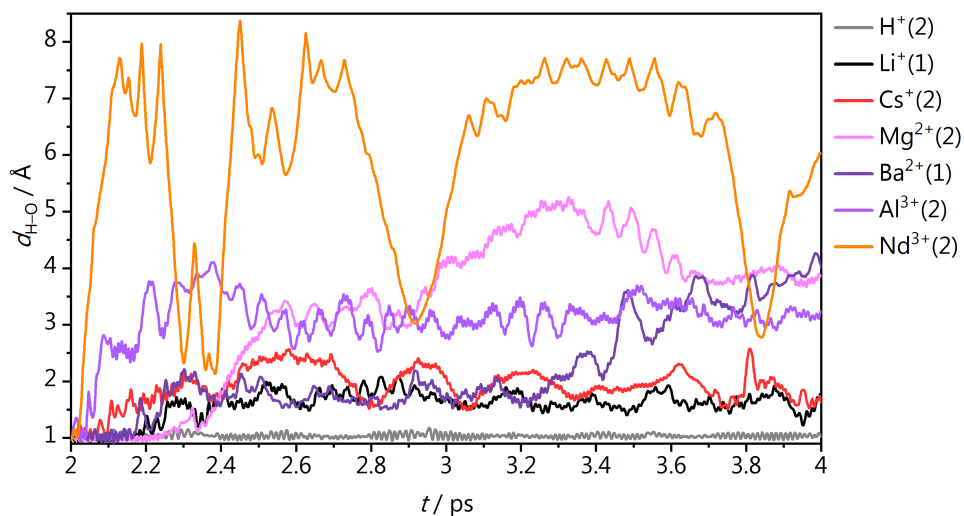
Fig. F.14. H-O Distances in the adsorbed water molecule for the Au/water/M^{n+}/*H$_2$O system (from 2 to 4 ps). For all the metal cations *H$_2$O dissociates into OH$^-$ and H$^+$ after less than 0.3 ps.
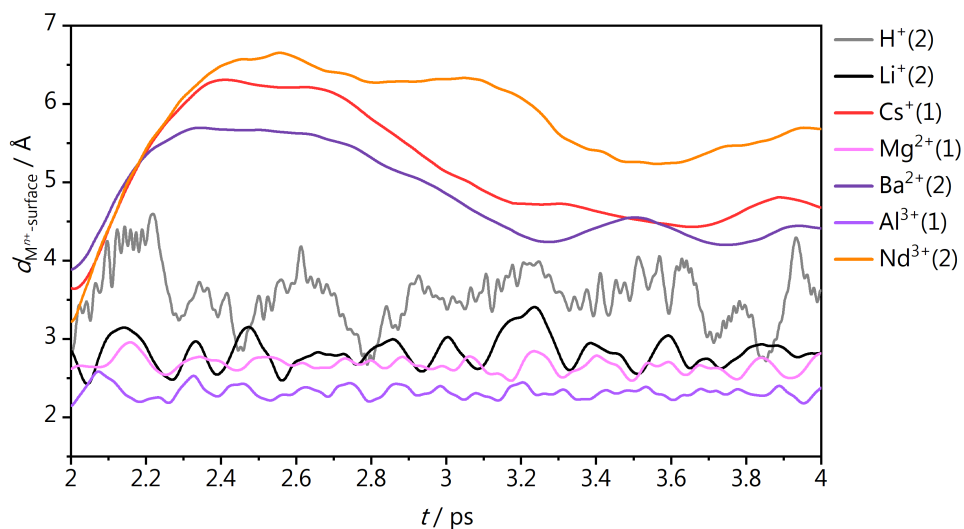
F

Fig. F.15. Distance between cation (M^{n+}) and surface calculated for the Au/water/M^{n+}/*H$_2$O system (from 2 to 4 ps).
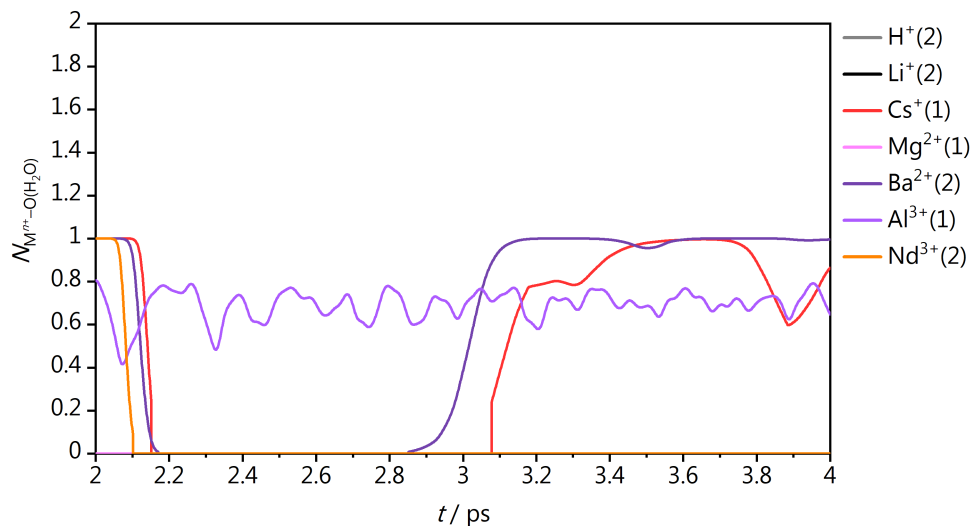
Fig. F.16. Cation coordination numbers to oxygen atoms in adsorbed H$_2$O ($N_{M-O(H2O)}$) for the Au/water/M^{n+}/*H$_2$O system (from 2 to 4 ps).
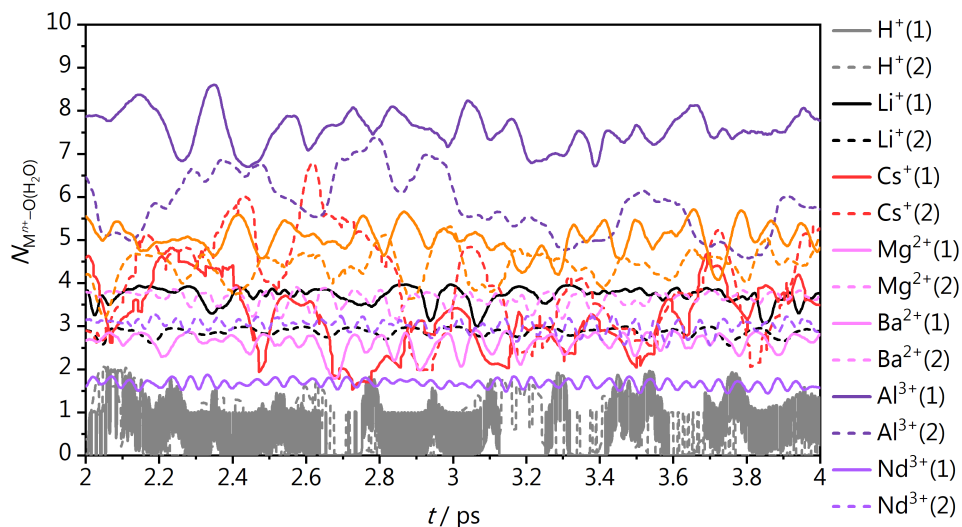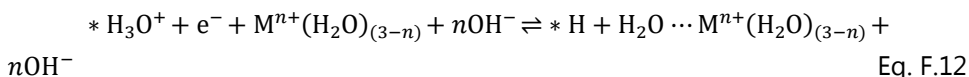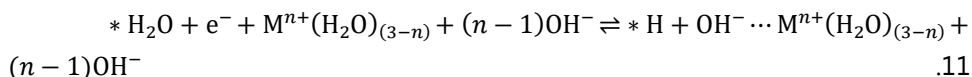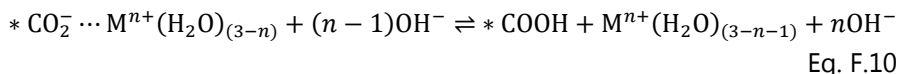

Fig. F.17. Cation coordination numbers to oxygen atoms in solvent molecules ($N_{M-O(H2O)}$) for the Au/water/M^{n+}/*H$_2$O system (from 2 to 4 ps).

Table F.4. Cation coordination numbers to oxygen atoms in adsorbed H_2O ($N_{M\text{-}O(H2O)}$) as calculated through Eq. F.4 for Au/water/M^{n+}/H_2O during 2 ps AIMD at 300 K (Fig. F.16-F.17). Coordination numbers are reported as averages with their associated standard deviation $\sigma(N_{cat\text{-}O})$, median, maximum, and minimum values.

M^{n+}	$N_{M\text{-}O(H2O)}$ (Au/water/M^{n+}/*H_2O)				$N_{M\text{-}O(CO2)}$ (Au/water/M^{n+}/*H_2O)			
	Mean	Median	Max	Min	Mean	Median	Max	Min
H^+	0.6 ± 0.6	0.2	2.1	0.0	0.0 ± 0.0	0.0	0.0	0.0
Li^+	2.87 ± 0.09	2.9	3.0	2.6	0.0 ± 0.0	0.0	0.0	0.0
Cs^+	4.0 ± 1.1	4.0	6.8	2.0	0.5 ± 0.4	0.6	1.0	0.0
Mg^{2+}	2.6 ± 0.2	2.7	2.9	1.8	0.0 ± 0.0	0.0	0.0	0.0
Ba^{2+}	5.8 ± 0.7	5.8	7.4	4.6	0.6 ± 0.5	0.9	1.0	0.0
Al^{3+}	1.67 ± 0.09	1.7	1.9	1.4	0.7 ± 0.1	0.7	0.8	0.4
Nd^{3+}	4.4 ± 0.4	4.4	5.3	3.2	0.0 ± 0.2	0	1.0	0

F.3.4 Determination of the activation barriers.

To estimate the activation energies for H_2O and H_3O^+ dissociation and CO_2 protonation, we considered an Au/2-3H_2O/M^{n+}/*ads* system, with simplified cation solvation shell with 2-3 water molecules. Eq. F10-12 define the processes for 3 water molecules in the solvation shell. We then removed $n - 1$ protons (n for H_3O^+ dissociation) from the system to keep an extra electron in the system ($n = 1, 2, 3$ for proton and alkali, divalent and trivalent cations respectively). Then, we let *CO_2, H, *H_3O^+, *H_2O, H_2O + *H and OH^- + *H adsorb close to the cation, and we further optimized the overall system Au/2-3H_2O/M^{n+}/*ads* (*ads* = *CO_2, *COOH, H_3O^+, *H_2O, H_2O + *H and OH^- + *H). Activation energies were calculated trough the Nudged Elastic Band (NEB) method and all of them exhibit a single imaginary vibrational frequency.[29] Gibbs free energies were calculated at 298.15 K by correcting DFT energies for entropic contributions. The energy references were chosen as CO_2(g), H_2(g) and H_2O(g) and single point calculations for the Au/2-3H_2O/M^{n+} system.

$$* CO_2^- \cdots M^{n+}(H_2O)_{(3-n)} + (n-1)OH^- \rightleftharpoons * COOH + M^{n+}(H_2O)_{(3-n-1)} + nOH^-$$

Eq. F.10

$$* H_2O + e^- + M^{n+}(H_2O)_{(3-n)} + (n-1)OH^- \rightleftharpoons * H + OH^- \cdots M^{n+}(H_2O)_{(3-n)} +$$
$$(n-1)OH^-$$

.11

$$* H_3O^+ + e^- + M^{n+}(H_2O)_{(3-n)} + nOH^- \rightleftharpoons * H + H_2O \cdots M^{n+}(H_2O)_{(3-n)} +$$
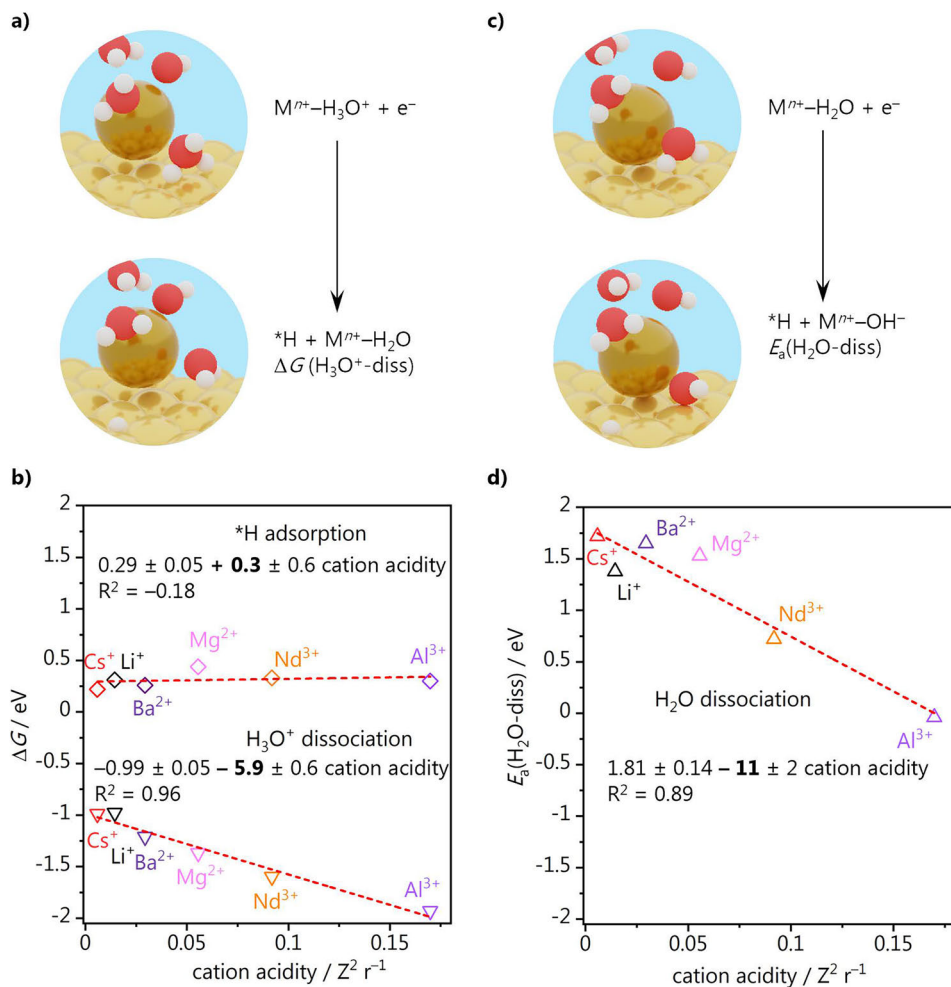$$nOH^-$$

Eq. F.12

Fig. F.18. a)-b) Gibbs free energy for *H adsorption (diamonds) and H_3O^+ dissociation (down-pointing triangles, Eq. F.12) vs. cation acidity, calculated with 3 H_2O molecules in cation solvation shell. **c)-d)** Activation barrier for water dissociation (up-pointing triangles, Eq. F.11) vs. cation acidity, calculated as average of the calculated values for 2 and 3 H_2O molecules in cation solvation shell. In the schemes, Au, Cs, H, and O atoms are portrayed as yellow, dark yellow, white, and oxygen spheres, respectively.
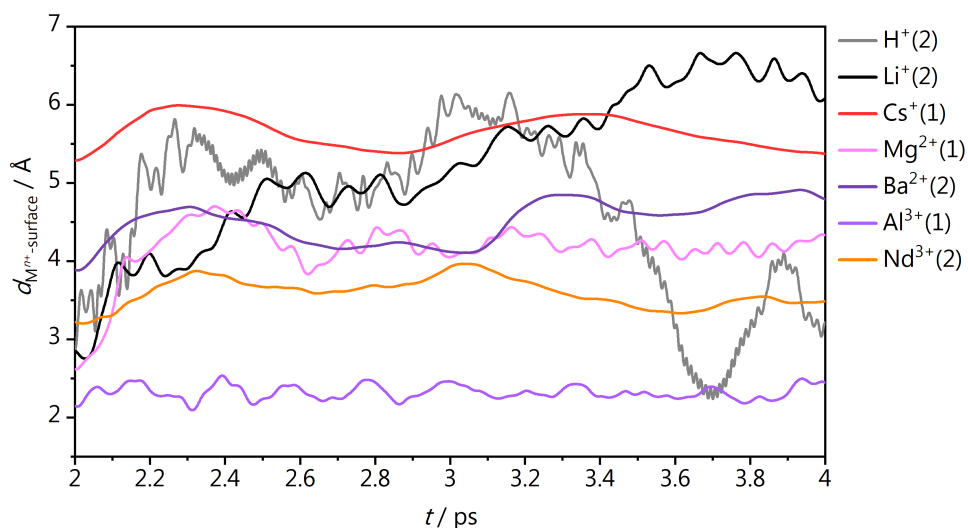
Fig. F.19. Distance between multivalent cation (M^{n+}) and surface calculated for the Au/water/M^{n+}/*CO_2 system (from 2 to 4 ps).

Table F.5. Cation coordination numbers to oxygen atoms in solvent molecules ($N_{M-O(H2O)}$) and adsorbed CO_2 ($N_{M-O(CO2)}$) as calculated through Eq. F.3 for Au/water/M^{n+}/*CO_2 during 2 ps AIMD at 300 K (Fig. F.16-F.17). Coordination numbers are reported as averages with their associated standard deviation $\sigma(N_{M-O})$, median, maximum, and minimum values.

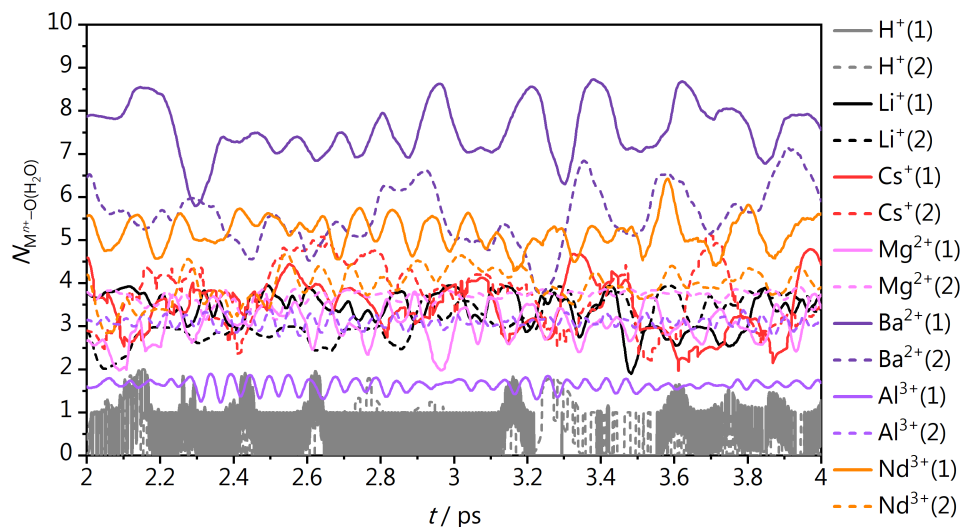| M^{n+}	$N_{M-O(H2O)}$ (Au/water/M^{n+}/*CO_2)				$N_{M-O(H2O)}$ (Au/water/M^{n+}/*CO_2)			
	Mean	Median	Max	Min	Mean	Median	Max	Min
H^+	0.5 ± 0.6	0.1	1.9	0.0	$0 \pm 3E{-}4$	0.0	0.01	0.0
Li+	3.1 ± 0.5	3.0	3.9	2.0	0.0 ± 0.2	0.0	1.0	0.0
Cs^+	3.5 ± 0.6	3.5	4.8	2.0	0.7 ± 0.4	0.8	1.8	0.0
Mg^{2+}	3.0 ± 0.4	3.0	3.8	2.0	0.6 ± 0.4	0.7	1.0	0.0
Ba^{2+}	5.6 ± 0.7	5.5	7.1	3.8	0.9 ± 0.2	1.0	1.0	0.1
Al^{3+}	1.63 ± 0.12	1.6	1.9	1.2	0.5 ± 0.2	0.5	0.9	0.0
Nd^{3+}	3.9 ± 0.4	3.9	4.7	2.8	0.9 ± 0.2	0.9	1.0	0

Fig. F.20. Cation coordination numbers to oxygen atoms in solvent molecules ($N_{\text{M-O(H2O)}}$) for the Au/water/M^{n+}/*CO_2 system (from 2 to 4 ps).
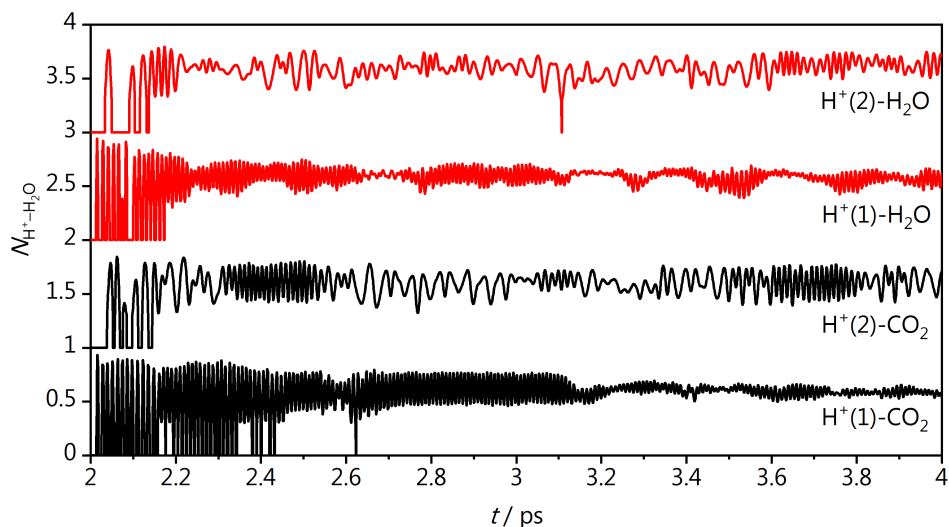

Fig. F.21. Bond formation between H^+ and neighboring water molecule for Au/water/H^+/*CO_2 system and Au/water/H^+/*H_2O system (from 2 to 4 ps). Proton is not effective as a CO_2 reduction promoter, since it combined with a neighboring water molecule to form a H_3O^+ after less than 0.2 ps.
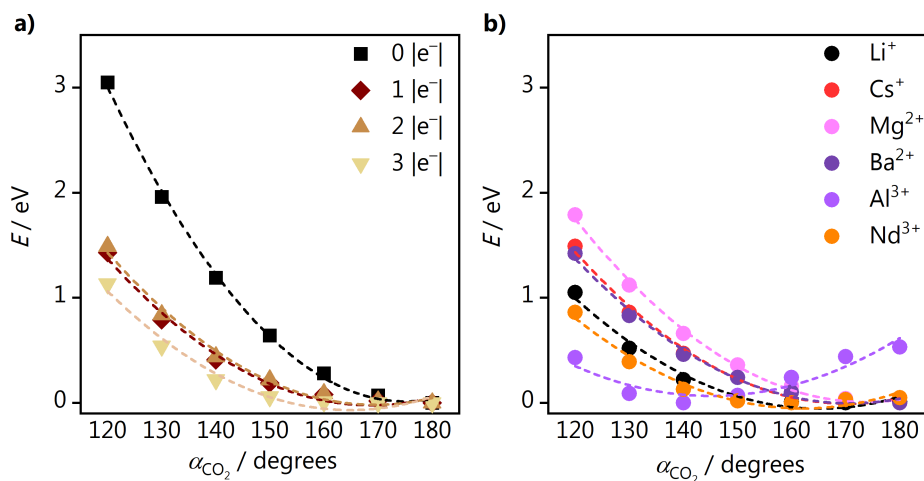
Fig. F.22. DFT energy of **a)** a free CO_2 and **b)** a CO_2 coordinated to a multivalent cation as a function of the CO_2 activation angle, α. Lower α values indicate CO_2 activation. $M^{n+}\cdots O(CO_2)$ distances have been set according to AIMD results (Table F.1). Different colors highlight **a)** additional electrons in the simulation cell (from 1 to 3) and **b)** different cation species. Dashed lines represent a quadratic fit over the data points.

Table F.6. Fit parameters for quadratic correlations shown in Fig. F.21:

$$E = a + b * \alpha_{CO_2} + c * \alpha_{CO_2}{}^2$$

System	a / eV	b / eV degrees^{-1}	c / eV degrees^{-2}	R^2
CO_2 (0 $|e^-|$)	+30 ± 1	−0.35 ± 0.02	+9.9E-04 ± 6E-05	0.998
CO_2 (1 $|e^-|$)	+17 ± 2	−0.20 ± 0.02	+5.9E-04 ± 7E-05	0.98
CO_2 (2 $|e^-|$)	+17 ± 2	−0.20 ± 0.02	+5.9E-04 ± 7E-05	0.985
CO_2 (3 $|e^-|$)	+15 ± 2	−0.19 ± 0.03	+5.6E-04 ± 9E-05	0.97
$Li^+\cdots CO_2$ (1 $|e^-|$)	+14 ± 2	−0.17 ± 0.02	+5.2E-04 ± 7E-05	0.97
$Cs^+\cdots CO_2$ (1 $|e^-|$)	+17 ± 1	−0.19 ± 0.02	+5.7E-04 ± 7E-05	0.988
$Mg^{2+}\cdots CO_2$ (2 $|e^-|$)	+18 ± 1	−0.209 ± 0.014	+6.0E-04 ± 5E-05	0.996
$Ba^{2+}\cdots CO_2$ (2 $|e^-|$)	+16 ± 1	−0.18 ± 0.02±	+5.3E-04 ± 6E-05	0.989
$Al^{3+}\cdots CO_2$ (3 $|e^-|$)	+10 ± 2	−0.13 ± 0.03	+4.52E-04 ± 1.1E-04	0.77
$Nd^{3+}\cdots CO_2$ (3 $|e^-|$)	+13 ±2	−0.16 ± 0.02	+4.9E-04 ± 7E-05	0.96

F

References

(1)   Monteiro, M. C. O.; Koper, M. T. M. *Electrochim. Acta* 2019, *325*, 134915.

(2)   Li, X.; Gunathunge, C. M.; Agrawal, N.; Montalvo-Castro, H.; Jin, J.; Janik, M. J.; Waegele, M. M. *J. Electrochem. Soc.* 2020, *167* (10), 106505.

(3)   Do, U. P.; Seland, F.; Johannessen, E. A. *J. Electrochem. Soc.* 2018, *165* (5), H219–H228.

(4)   Kresse, G.; Furthmüller, J. *Phys. Rev. B* 1996, *54*, 11169–11186.

(5)   Kresse, G.; Furthmüller, J. *Comput. Mater. Sci.* 1996, *6*, 15–50.

(6)   Perdew, J. P.; Burke, K.; Ernzerhof, M. *Phys. Rev. Lett.* 1996, *77*, 3865–3868.

(7)   Grimme, S. *J. Comput. Chem.* 2006, *27*, 1787–1799.

(8)   Bucko, T.; Hafner, J.; Lebègue, S.; Ángyán, J. G. *J. Phys. Chem. A* 2010, *114*, 11814–11824.

(9)   Almora-Barrios, N.; Carchini, G.; Błoński, P.; López, N. *J. Chem. Theory Comput.* 2014, *10*, 5002–5009.

(10)   Blöchl, P. E. *Phys. Rev. B* 1994, *50*, 17953–17979.

(11)   Kresse, G.; Joubert, D. *Phys. Rev. B* 1999, *59*, 1758–1775.

(12)   Marx, D.; Hutter, J. Cambridge University Press, 2009.

(13)   Nosé, S. *J. Chem. Phys.* 1984, *81*, 511–519.

(14)   Hoover, W. G. *Phys. Rev. A* 1985, *31*, 1695–1697.

(15)   Monteiro, M. C. O.; Dattila, F.; Hagedoorn, B.; García-Muelas, R.; López, N.; Koper, M. T. M. *Nat. Catal.* 2021, *4* (8), 654–662.

(16)   Dudarev, S. L.; Botton, G. A.; Savrasov, S. Y.; Humphreys, C. J.; Sutton, A. P. *Phys. Rev. B* 1998, *57* (3), 1505–1509.

(17)   Kozub, A. L.; Shick, A. B.; Máca, F.; Kolorenč, J.; Lichtenstein, A. I. *Phys. Rev. B* 2016, *94* (12), 125113.

(18)   Monteiro, M. C. O.; Jacobse, L.; Koper, M. T. M. *J. Phys. Chem. Lett.* 2020, *11* (22), 9708–9713.

(19)   Lide, D. R. 84th ed.; Lide, D. R., Ed.; CRC Press, 2003; Vol. 85.

(20)   Bellarosa, L.; García-Muelas, R.; Revilla-López, G.; López, N. *ACS Cent. Sci.* 2016, *2* (2), 109–116.

(21)   Feibelman, P. J. *Phys. Rev. B* 2001, *64* (12), 125403.

(22)   McCrum, I. T.; Bondue, C. J.; Koper, M. T. M. *J. Phys. Chem. Lett.* 2019, *10* (21), 6842–6849.

(23)   Chen, L. D.; Urushihara, M.; Chan, K.; Nørskov, J. K. *ACS Catal.* 2016, *6* (10), 7133–7139.

(24)   White, R. E.; Bockris, J. O.; Conway, B. E. Kluwer Academic Publishers, 2002.

(25)   Makov, G.; Payne, M. *Phys. Rev. B* 1995, *51*, 4014–4022.

(26)   Waegele, M. M.; Gunathunge, C. M.; Li, J.; Li, X. *J. Chem. Phys.* 2019, *151* (16), 160902.

(27)   Marcus, Y. *Chem. Rev.* 1988, *88* (8), 1475–1498.

(28)   Dattila, F.; García-Muelas, R.; López, N. *ACS Energy Lett.* 2020, *5*, 3176–3184.

(29)   Resasco, J.; Chen, L. D.; Clark, E.; Tsai, C.; Hahn, C.; Jaramillo, T. F.; Chan, K.; Bell, A. T. *J. Am. Chem. Soc.* 2017, *139* (32), 11277–11287.

(30)   Nørskov, J. K.; Rossmeisl, J.; Logadottir, A.; Lindqvist, L.; Kitchin, J. R.; Bligaard, T.; Jónsson, H. *J. Phys. Chem. B* 2004, *108* (46), 17886–17892.

(31)   Haynes, W. M. 95th ed.; CRC Press: New York, 2014.

(32)   Henkelman, G.; Jónsson, H. *J. Chem. Phys.* 2000, *113* (22), 9978–9985.

F

G
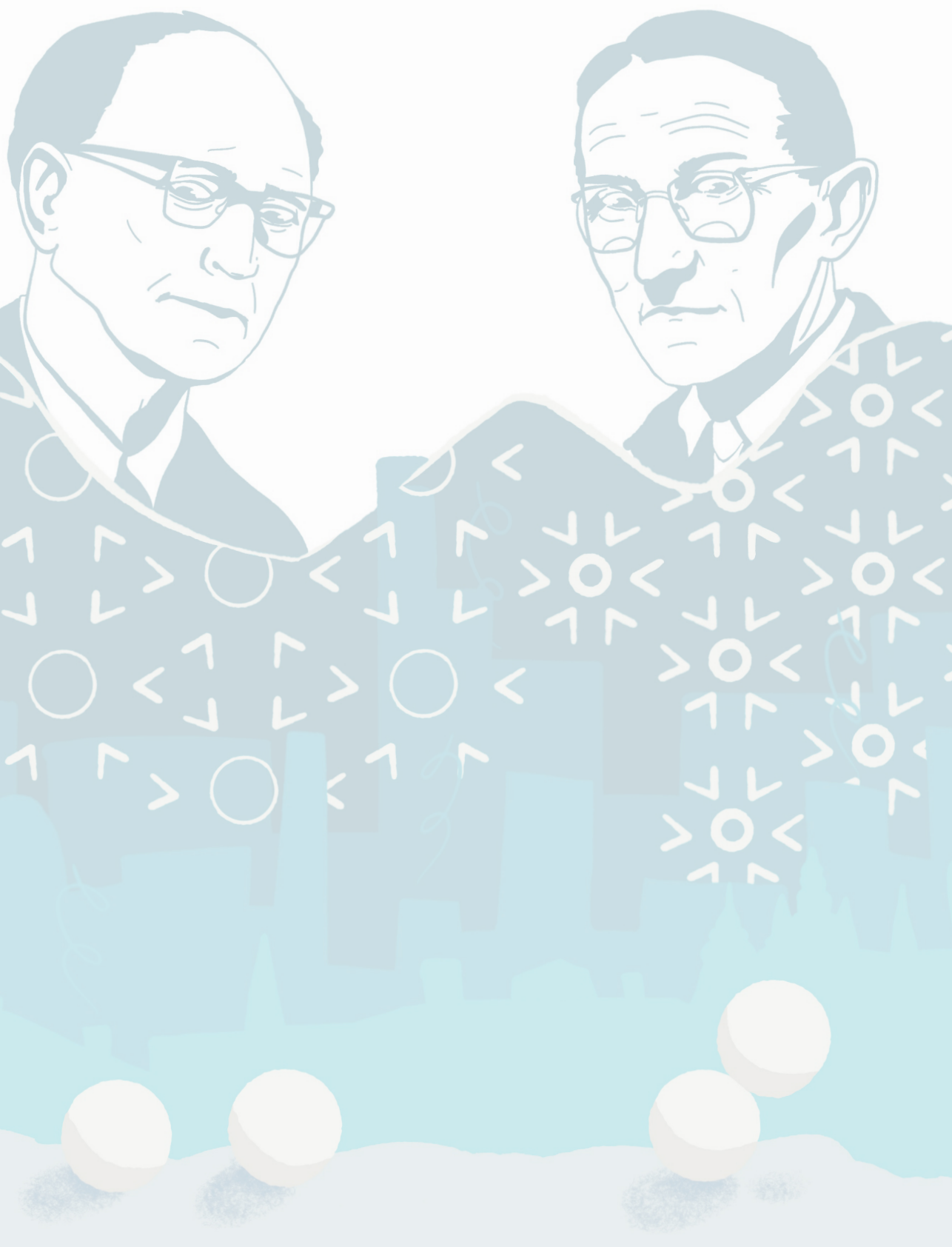
Methods and supporting information to Chapter 10

G.1 Methods

G.1.1 Materials

The following chemicals were used to prepare the electrolytes used in this work: Li_2SO_4 (Sigma Aldrich, 99.99 % metal basis), K_2SO_4 (Alfa Aesar, Puratronic, 99.997 %, metals basis), H_2SO_4 (Merck, Suprapur, 96%), $LiClO_4$ (Sigma Aldrich, 99.99%, trace metal basis), $KClO_4$ (Sigma Aldrich, ≥99.99%, trace metal basis), LiOH (Sigma Aldrich, 99.995%, monohydrate), NaOH (Merck, 30% solution, Suprapur®), KOH (Merck, 99.995%, Suprapur®). The sulfate salts were used for the experiments in acidic media and the hydroxides for the experiments in alkaline media. For the measurements in alkaline media in which the cation concentration is varied, appropriate amounts of perchlorate salts were added to the electrolyte. Gold and platinum disc electrodes were cut from a polycrystalline gold (0.5 mm thick, MaTecK, 99.995%) and platinum (0.5 mm thick, MaTecK, 99.99%) foil and prepared according to the method described in Chapter 7. All glassware used was cleaned by immersion in a potassium permanganate solution overnight (1 g/L $KMnO_4$ dissolved in 0.5 M H_2SO_4), followed by immersion in dilute piranha. The glassware was further boiled in ultrapure water at least five times before use.

G.1.2 Electrochemical measurements

All electrochemical measurements were carried out using a BioLogic two-channel potentiostat/galvanostat/ EIS (SP-300). The hanging meniscus and rotating disc electrode (RDE) experiments were carried out in a one compartment glass cell. A gold (0.5 mm diameter, MaTeck, 99.9%) or a platinum (0.5 mm diameter, MaTeck, 99.9%) wire was used as counter electrode (depending on the working electrode) and a reversible hydrogen electrode (Gaskatel, HydroFlex) as reference. Argon (6.0 purity, Linde) was purged through the solution for 20 minutes prior to the experiments. The argon flow was kept also during the experiments in order to avoid oxygen diffusing into the electrolyte. Before the measurements, the gold electrode was prepared by flame annealing, using the procedure described in our previous work.[1] The platinum electrode was also flame annealed and subsequently cycled 200 times between 0.06 and 1.65 V vs. RHE in 0.1 M H_2SO_4 at 1 V s^{-1}, in order to yield a reproducible blank voltammogram. Blank CVs were recorded in argon saturated 0.1 M H_2SO_4 prior to every measurement. The electrochemically active surface area (ECSA) of gold was calculated based on the charge corresponding to the gold oxide reduction and a surface charge density of 386 μC cm^{-2}.[2] For platinum, the integral of the hydrogen desorption region 0.06 < E < 0.6 V was used

(after subtraction of the double layer charge), and the ECSA was calculated based on the specific charge of 230 μC cm^{-2} reported for a polycrystalline Pt surface in sulfuric acid.[3] RDE experiments were performed using a MSR Electrode Rotator (Pine Research Instrumentation) equipped with a AFE6M shaft, and a gold and a platinum disk (diameter = 5 mm, Pine Research Instrumentation). The rotating disc electrodes were polished with a polycrystalline diamond suspension of 0.25 μm (MetaDi, Buehler) and then sonicated (Bandelin Sonorex RK 52H) in ethanol and ultrapure water (>18.2 MΩ cm, Millipore Milli-Q) for 10 minutes before the measurements. For all hydrogen evolution experiments, the solution resistance was determined by performing Potentiometric Electrochemical Impedance Spectroscopy (PEIS) and the electrode potential was always automatically compensated for 85% of the ohmic drop.

G.2 Hydrogen evolution in acidic media

In mildly acidic media (pH = 3), we see first a cathodic current due to proton reduction ($2H^+ + 2e^- \rightarrow H_2$) on both gold (Fig. G.1a) and platinum (Fig. G.1b) followed by a peak due to diffusion limitation. On gold, the reaction kinetics is not affected by the cation identity, and is only dependent on the proton concentration at the reaction interface, as we also observed in our recent work.[4] On platinum, we see that K^+ slightly increases the rate of the reaction, as higher currents are obtained at low overpotentials, where the reaction is only kinetically limited. In acidic media, an often used descriptor for HER on platinum is the hydrogen binding energy and the free energy of hydrogen adsorption ($\Delta G_{H,ads}$), which on platinum is close to zero. A way to probe the hydrogen binding energy on Pt is by recording the blank voltammetry, as we show in Fig. G.1c in Li^+ and K^+ containing electrolyte. We see a positive shift of 10 mV in the underpotential hydrogen (H_{upd}) peak (between 0.2 and 0.3 V vs. RHE) in K^+ electrolyte, which has been previously ascribed to an increase in the hydrogen binding energy.[5] However, work from our group on Pt(553) shows that there is a cation dependence of the potential of the {110}-step related H_{upd} peak. It shows through experiments and Density Functional Theory (DFT) that alkali-metal cations adsorbed near the step, weaken low coverage hydroxide adsorption, shifting the step associated peak to more positive potentials.[6] Therefore, we cannot ascribe the shift we observe in Fig. G.1c to changes in the hydrogen binding energy, but actually to a cation–OH_{ads}–H_{ads} interaction.[6] In Fig. G.1a and Fig. G.1b, at more negative potentials, as proton reduction reaches diffusion limitation and the interfacial pH becomes more alkaline, water reduction starts to takes place ($2H_2O$

+ 2e$^-$ → H$_2$ + 2OH$^-$). We see that on both metal surfaces the water reduction reaction (in neutral to mildly alkaline media) is still promoted by K$^+$ cations, although the differences are more pronounced for gold than for platinum.
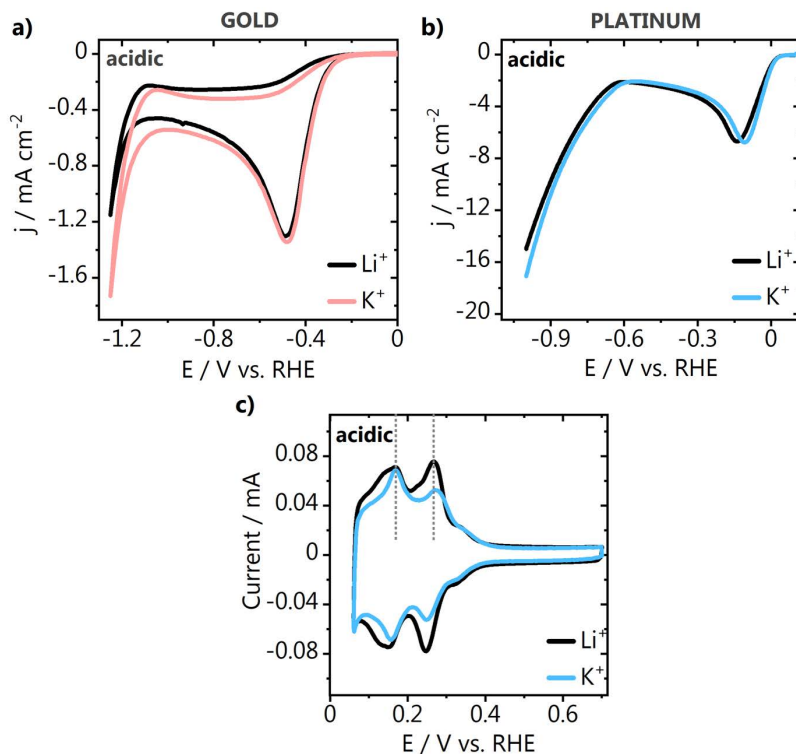

Fig. G.1. Stationary hydrogen evolution on **a)** gold and **b)** platinum in acidic media (0.1 M M_2SO_4, pH = 3), together with **c)** the blank voltammetry of the platinum electrode.
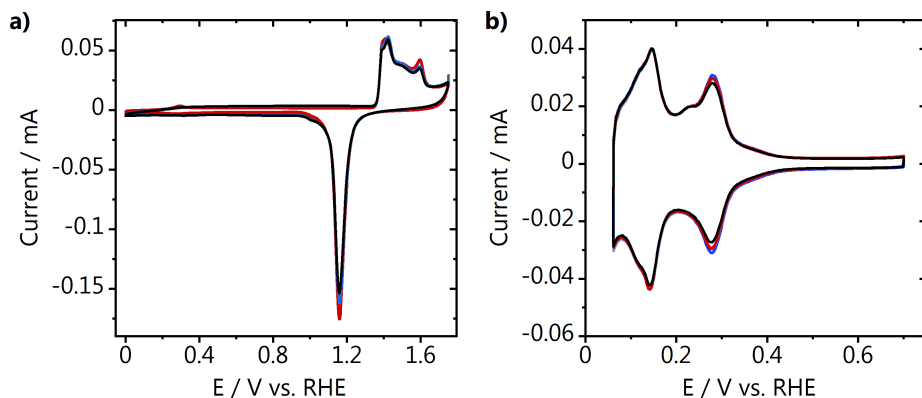
G.3   Blank voltammetry: stationary experiments

Fig. G.2. Blank voltammetry of the polycrystalline **a)** gold and **b)** platinum electrodes used for the stationary experiments in this work, recorded in 0.1 M H_2SO_4 at 50 mV s^{-1}. Several CVs are overlapped, which were recorded before the HER experiments carried out in different electrolytes, pH.

G.4   Blank voltammetry: rotating disc experiments
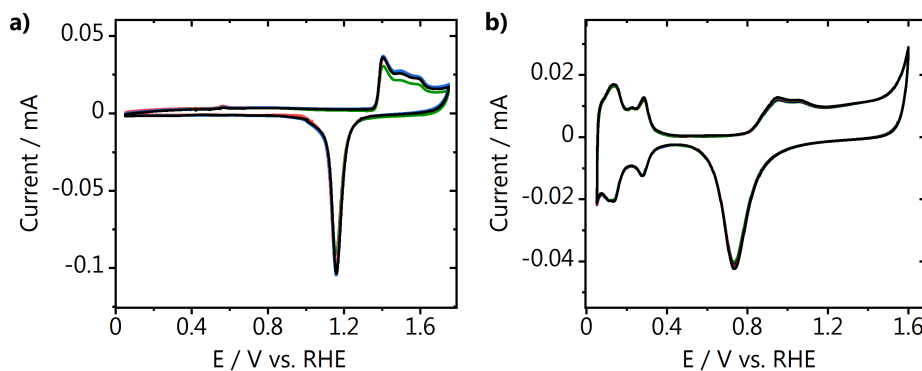
Fig. G.3. Blank voltammetry of the polycrystalline **a)** gold and **b)** platinum electrodes used for the rotating disc experiments in this work, recorded in 0.1 M H_2SO_4 at 50 mV s^{-1}. Several CVs are overlapped, which were recorded before the HER experiments carried out in different electrolytes, pH.
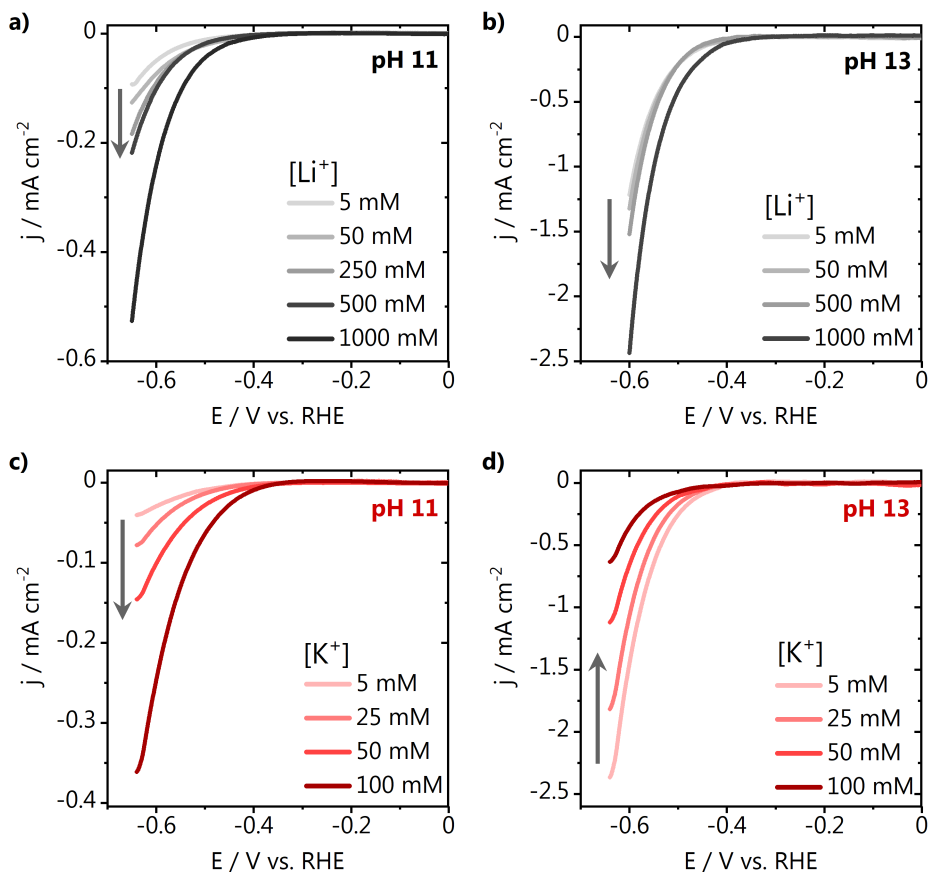
G.5   Cation concentration: cyclic voltammetry on gold

Fig. G.4. a)-d) Hydrogen evolution cyclic voltammograms recorded on polycrystalline gold in $MOH + X$ mM MClO$_4$, at different pH, with M = Li$^+$ or K$^+$ and X = 5, 25, 50 and 100, using a rotating disc electrode, at 25 mV s^{-1} and 2500 rpm.

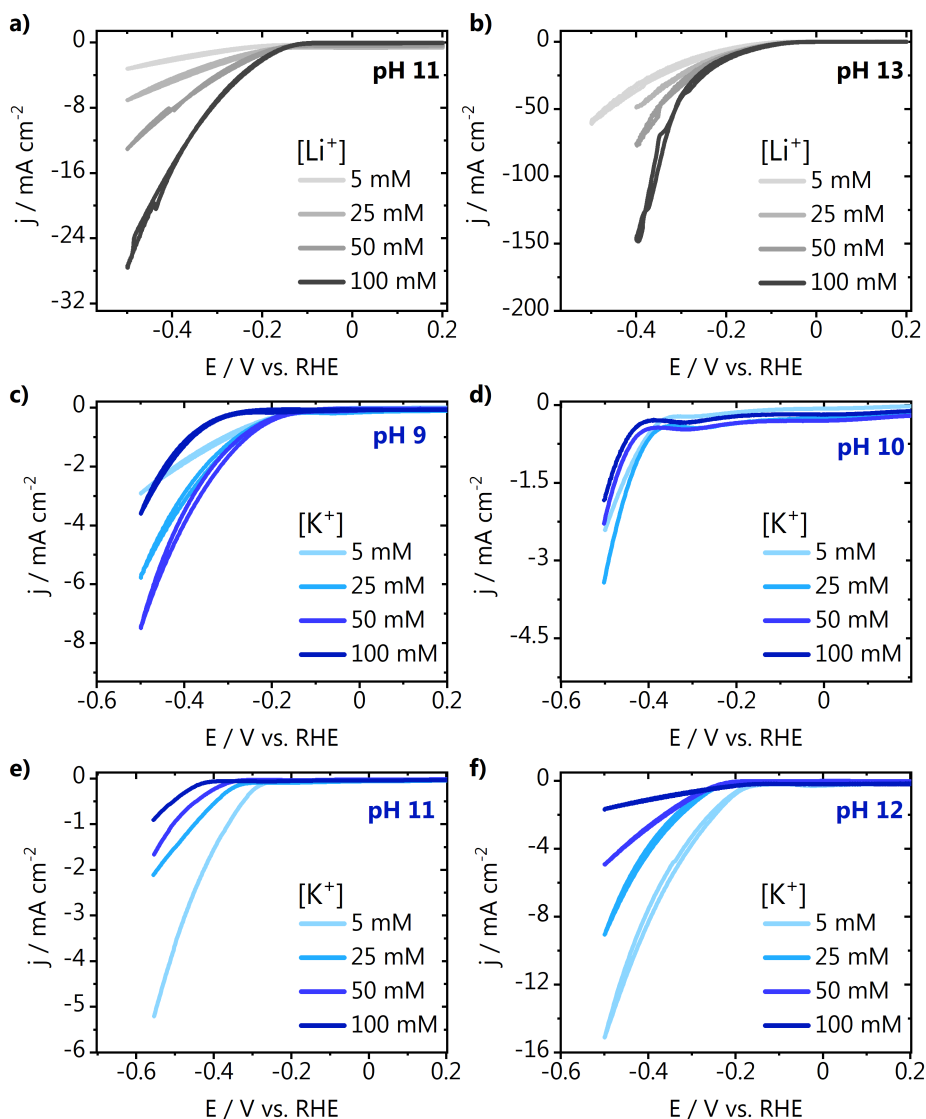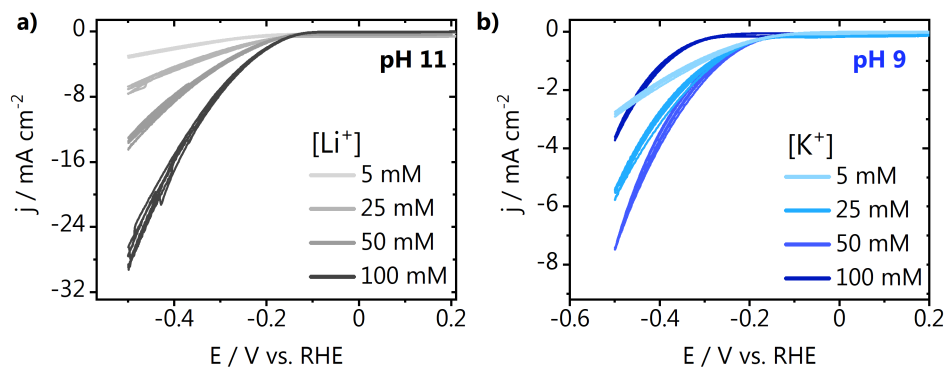## G.6 Cation concentration: cyclic voltammetry on platinum

Fig. G.5. a)-f) Hydrogen evolution cyclic voltammograms recorded on polycrystalline platinum in MOH + X mM MClO$_4$, at different pH, with M = Li$^+$ or K$^+$ and X = 5, 25, 50 and 100, using a rotating disc electrode, at 25 mV s^{-1} and 2500 rpm.

Fig. G.6. Five consecutive hydrogen evolution cyclic voltammograms recorded on polycrystalline platinum in MOH + X mM MClO$_4$, at different pH, with M as **a)** Li$^+$ or **b)** K$^+$ and X = 5, 25, 50 and 100, using a rotating disc electrode, at 25 mV s^{-1} and 2500 rpm.

References

(1)   Monteiro, M. C. O.; Koper, M. T. M. *Electrochim. Acta* 2019, *325*, 134915.

(2)   Do, U. P.; Seland, F.; Johannessen, E. A. *J. Electrochem. Soc.* 2018, *165* (5), 219–228.

(3)   Chen, Q.-S.; Solla-Gullón, J.; Sun, S.-G.; Feliu, J. M. *Electrochim. Acta* 2010, *55* (27), 7982–7994.

(4)   Monteiro, M. C. O.; Dattila, F.; Hagedoorn, B.; García-Muelas, R.; López, N.; Koper, M. T. M. *Nat. Catal.* 2021, *4* (8), 654–662.

(5)   Sheng, W.; Zhuang, Z.; Gao, M.; Zheng, J.; Chen, J. G.; Yan, Y. *Nat. Commun.* 2015, *6*, 6–11.

(6)   Chen, X.; McCrum, I. T.; Schwarz, K. A.; Janik, M. J.; Koper, M. T. M. *Angew. Chemie - Int. Ed.* 2017, *56* (47), 15025–15029.

H

Methods and supporting information to Chapter II

H.1   Synthesis and characterization of gas diffusion electrodes

The synthesis method for the gas diffusion layer (GDL) was adjusted from a patented method.[1] First, 15 g of acetylene black (Soltex, 75%-03) was mixed with 8.91 mL PTFE (FuelCellStore, Teflon™ PTFE DISP 30) and 60 mL of a 1:1 volume water/isopropyl alcohol (IPA). After mixing, a dough was obtained and rolled with a marble rolling pin before using a cross rolling technique to obtain the desired thickness. The PTFE dispersion was diluted by 50% with 1:1 volume water/IPA, applied to the back of the dough, and graphitized carbon was placed on top. A Carver heated press (Model number 4533) was used to press the structure at 140 °C and 10.25 Ton for 32.5 min. Then the temperature was raised to 308 °C at the same pressure and held for 32.5 minutes. Finally the temperature was raised to 317.5 °C at 13 ton and held for 32.5 min before removing the structure from the press. GDLs of 17.16 cm² were cut from the resulting structure. Commercial gold nanoparticles were used as catalyst (60% gold supported on vulcan XC-72 (carbon), FuelCellStore). The catalyst ink was prepared by suspending the particles in ethanol and adding 250 µL of a Nafion© solution under constant stirring. The inks were additionally sonicated for 30 minutes. The obtained ink was airbrushed on a 17 cm² GDL and let dry. The catalysts metal loading was calculated by weighing the electrodes before and after the spraying.

The gold GDEs topography and composition were characterized by Scanning Electron Microscopy (SEM) in an Apreo SEM (ThermoFisher Scientific). Micrographs were obtained using an acceleration voltage of 10 kV and an electron beam current of 0.8 nA. Energy Dispersive X-Ray Spectroscopy (EDX) was used for elemental analysis (Oxford Instruments X-MaxN 150 Silicon Drift detector). EDX data processing was done with the Pathfinder™ X-ray Microanalysis software v1.3. The data is displayed in atomic percentage for easier visualization, however the quantification was performed in automatic mode, without providing external standards.

H.2   Electrolysis measurements

The gas diffusion electrodes were mounted in a commercial two-compartment 10 cm² GDE flow cell (ElectroCell, Micro Flow Cell) for the bulk electrolysis. The anolyte and the catholyte were separated by a reinforced Nafion™ membrane N324. For all measurements the anolyte was a 0.5 M H_2SO_4 solution and the anode a dimensionally stable anode (DSA®, ElectroCell). The electrolyte flow rate was 30 mL min⁻¹, achieved with a peristaltic pump. A CO_2 flow of 50 mL min⁻¹

was employed for all the measurements. The following chemicals were used to prepare the electrolytes for bulk CO_2 electrolysis: Cs_2SO_4 (Sigma Aldrich, 98%), Li_2SO_4 (Sigma Aldrich, 98%), $KHCO_3$ (Acros Organics, 99.5%), H_2SO_4 (Acros Organics, for analysis ACS, 95% solution in water). Either 1 M Cs_2SO_4, Li_2SO_4, or $KHCO_3$ were used as catholyte. The pH of the solutions was adjusted with H_2SO_4 when necessary using a pH meter. Galvanostatic bulk electrolysis measurements were controlled using a power supply and each different current density was applied for one hour. The product analysis was performed using a gas chromatograph (Varian 4900 micro GC) equipped with four modules: COx module, MS5 (mol. sieve) module, PPQ (poraplotQ) module and 52C WAX module. Gaseous samples were taken from the headspace every 3 minutes. The current efficiencies shown throughout this work represent the average values obtained during 1 hour of electrolysis, with the corresponding standard deviation.
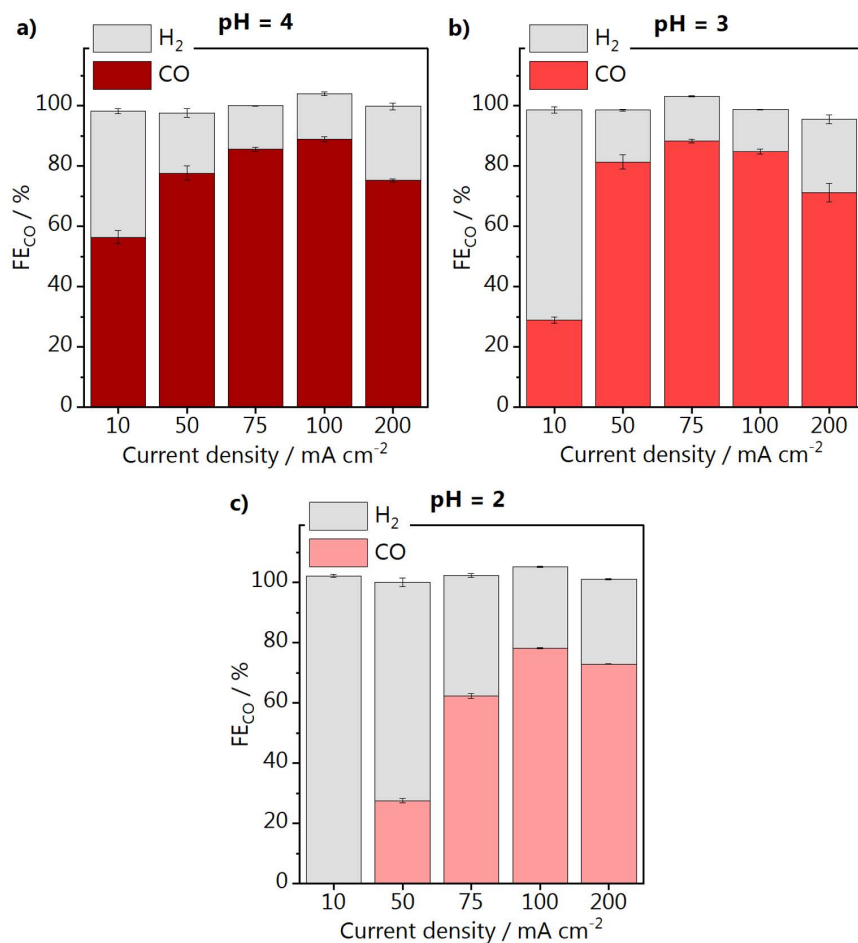
H

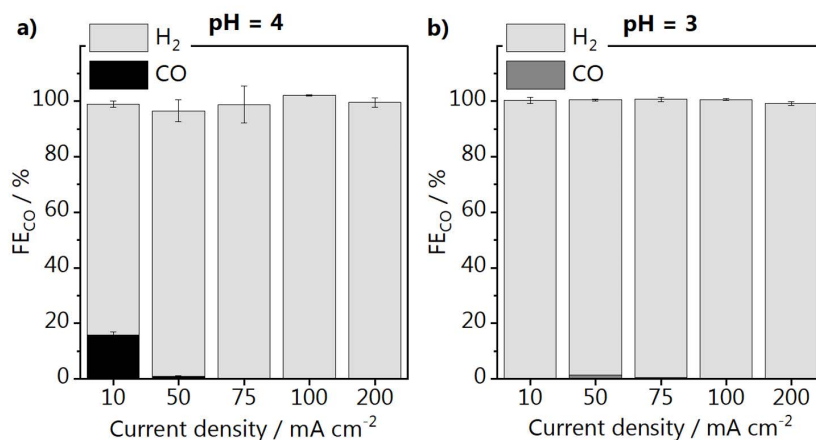## H.3 Faradaic efficiency for CO and H$_2$

Fig. H.1. Faradaic efficiencies for CO and H$_2$ obtained during one hour electrolysis at each current density displayed. The catholyte was 1 M Cs$_2$SO$_4$, **a)** pH 4, **b)** pH 3 and **c)** pH 2. Catalyst loading 2 mg cm^{-2}. Error bars are calculated based on three individual measurements.

Fig. H.2. Faradaic efficiencies for CO and H_2 obtained during one hour electrolysis at each current density displayed. The catholyte was 1 M Li_2SO_4, **a)** pH 4 and **b)** pH 3. Catalyst loading 2 mg cm^{-2}. Error bars are calculated based on three individual measurements.
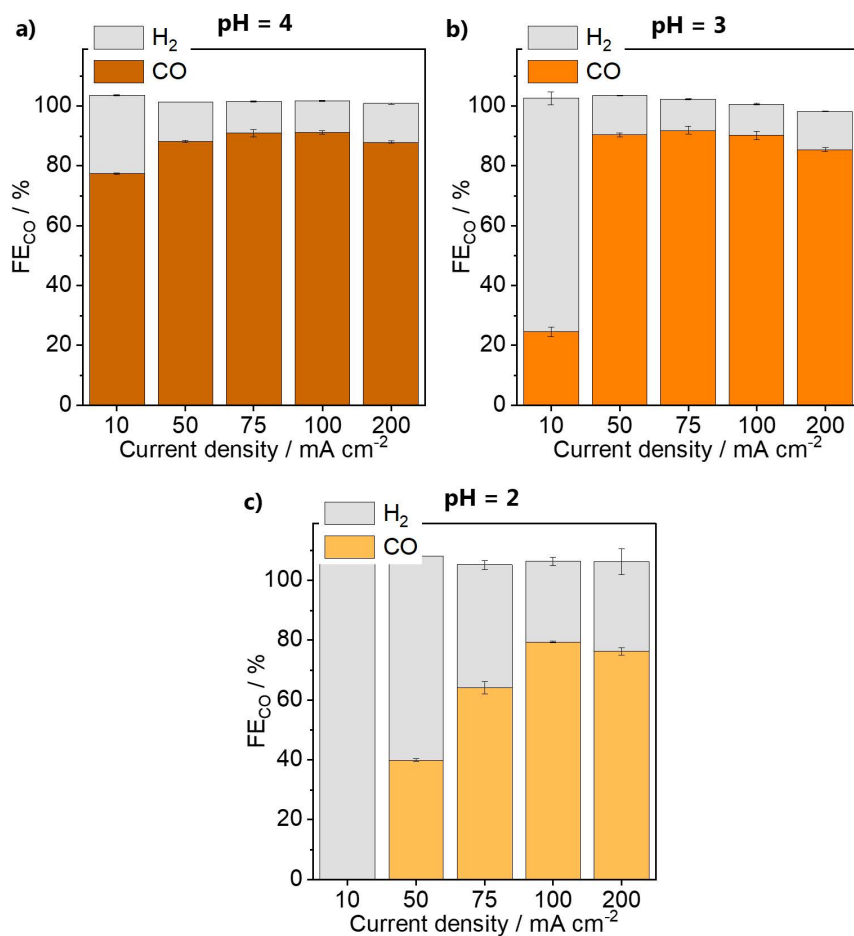
Fig. H.3. Faradaic efficiencies for CO and H_2 obtained during one hour electrolysis at each current density displayed. The catholyte was 1 M Cs_2SO_4; **a)** pH 4, **b)** pH 3 and **c)** pH 2. Catalyst loading 1 mg cm^{-2}. Error bars are calculated based on three individual measurements.

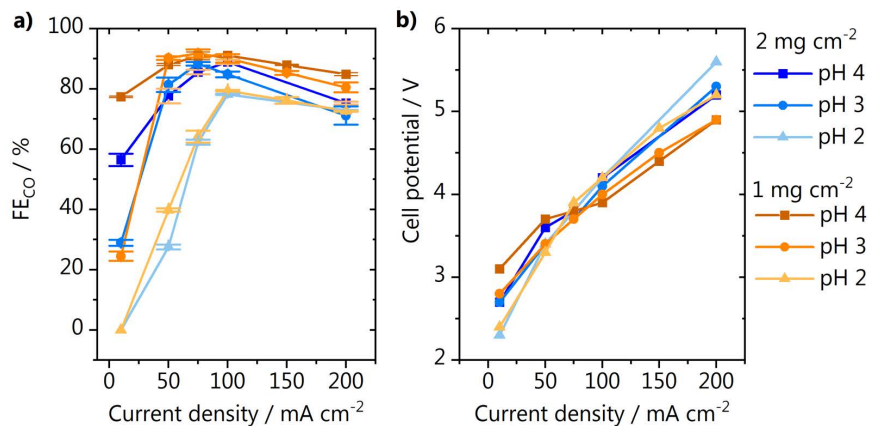## H.4   Effect of the catalyst loading

Fig. H.4. Electrolysis performed in 1 M Cs₂SO₄, catalyst loading 1 mg cm⁻² or 2 mg cm⁻², **a)** faradaic efficiency for CO and **b)** cell potential. The data points displayed are an average obtained during 1 hour electrolysis. Error bars are calculated based on three individual measurements.
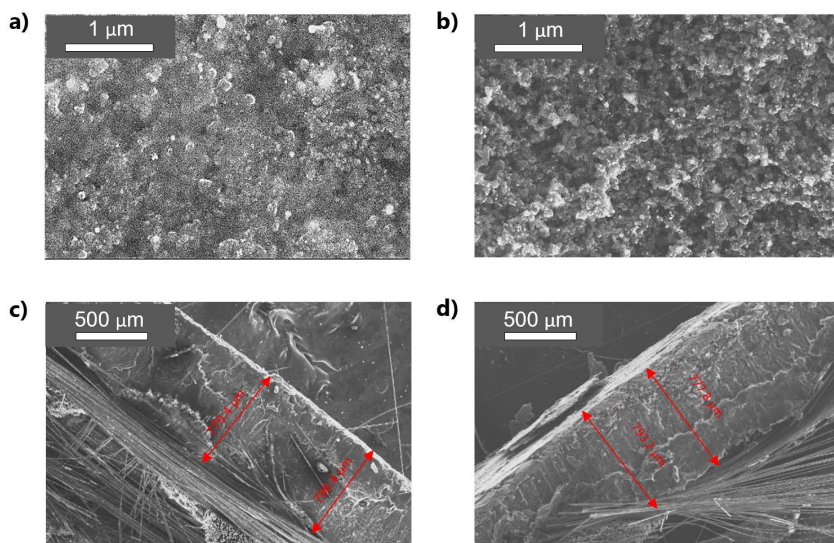

Fig. H.5. SEM micrograph of the gold GDEs. Top view of the **a)** 1 mg cm⁻² and **b)** 2 mg cm⁻² catalyst, and cross-section of the **c)** 1 mg cm⁻² and **d)** 2 mg cm⁻² catalyst.
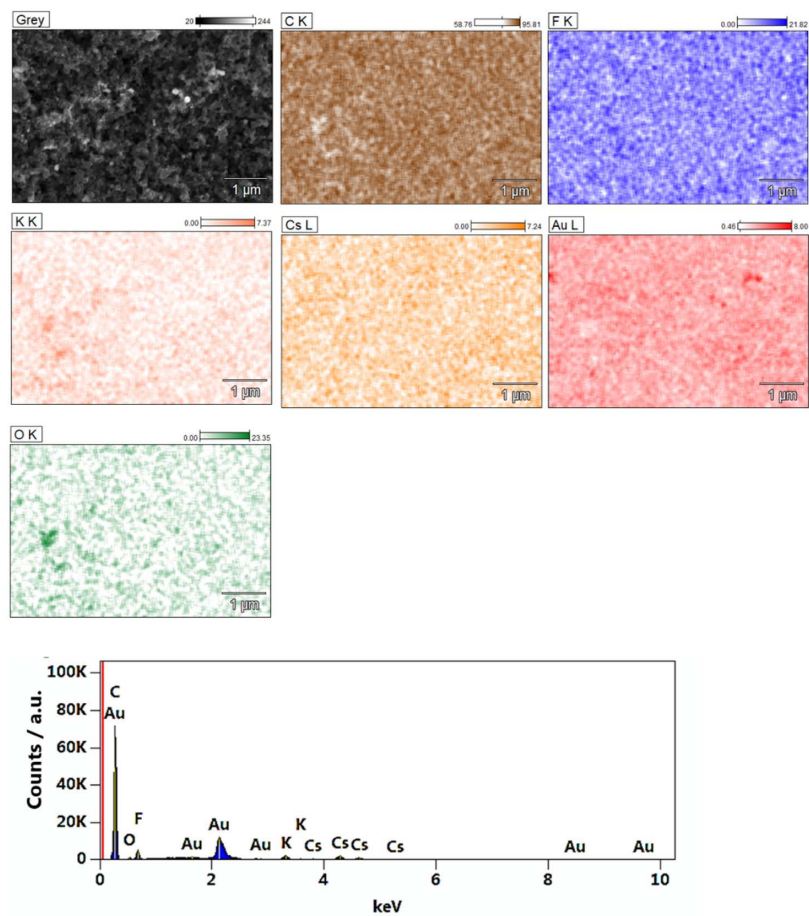
Fig. H.6. SEM micrograph, EDX elemental map and spectrum of the gold GDE with 1 mg cm^{-2} loading.
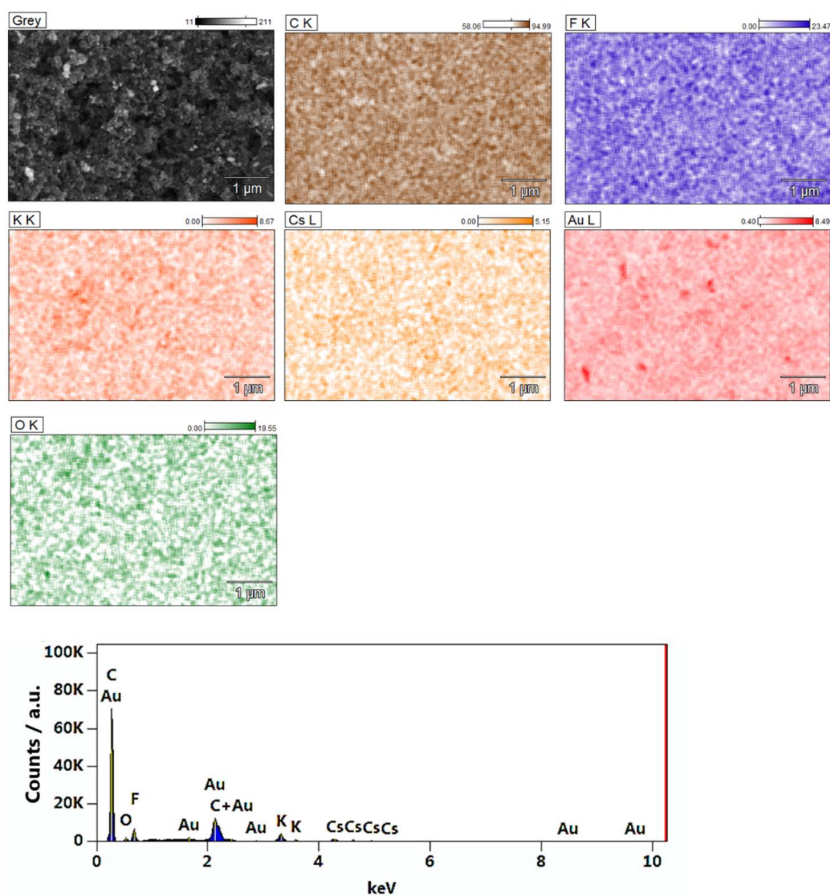
Fig. H.7. SEM micrograph, EDX elemental map and spectrum of the gold GDE with 2 mg cm^{-2} loading.
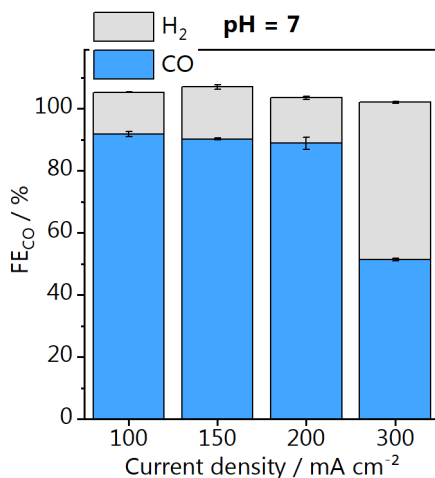
H.5 Comparison with neutral media

Fig. H.8. Faradaic efficiencies for CO and H_2 obtained during one hour electrolysis at each current density displayed. The catholyte was 1 M $KHCO_3$ (pH 7) and the catalyst loading 1 mg cm^{-2}. Error bars are calculated based on three individual measurements.

Fig. H.9. Energy consumption per ton of CO produced, based on the faradaic efficiencies and cell potentials obtained for electrolysis in 1 M Cs_2SO_4 or 1 M $KHCO_3$ at different current densities (catalyst loading 2 mg cm^{-2}).
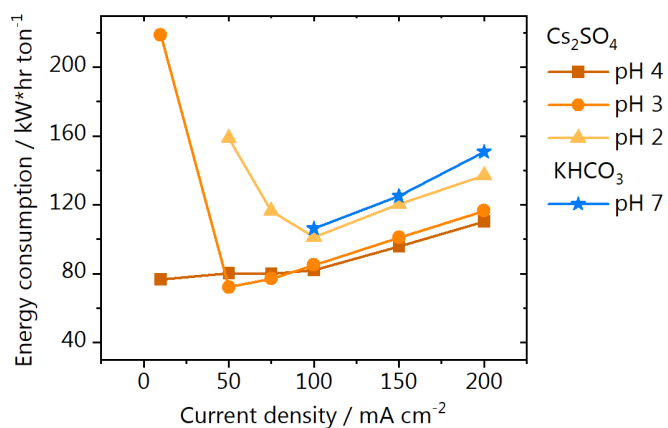
Energy consumption per ton of CO produced, based on the faradaic efficiencies and cell potentials obtained for electrolysis in 1 M Cs_2SO_4 or 1 M $KHCO_3$ at different current densities (catalyst loading 2 mg cm^{-2}).

Energy efficiency calculation:

$$\varepsilon_{energy} = \frac{\left(E^0_{CO_2} + E^0_{O_2}\right) * FE_{CO}}{E_{Cell}}$$

Eq. H.1

where E^0 are the standard potentials of the cathode and anode reactions, *FE* is the faradaic efficiency as percentage, and *Ecell* is the cell potential in V.

Energy consumption calculation:

$$\frac{kW * h}{ton} = \frac{E_{cell} * n * F}{MW * FE_{CO} * 3.6}$$

Eq. H.2

where *n* is the number of electrons transferred (dimensionless), *F* is Faraday´s constant in C mol^{-1}, *MW* is the molecular weight of CO in g mol^{-1}.

H

H.6   Comparison with literature

Table H.1. Experimental details of the different work from literature, used for the comparison made in Figure 5 in the main text. Only GDEs with geometrical surface area equal or larger than 5 cm^2 were considered.

	Cathode (GDE)	Anode	Electrolyte	CO$_2$ flow (mL min^{-1})	Load (mg cm^{-2})	Cathode area (cm^2)	Ref
this work	Au nanoparticles	DSA®	1 M Cs$_2$SO$_4$	50	1	10	this work
Haas 2018	Ag GDE Covestro	Ir-MMO/Ti sheet	0.1 M K$_2$SO$_4$ + 1.5 M KHCO$_3$	52 and 10.5	n.a.	10	[1]
Verma 2018	MWNT/PyPBI/Au on Sigracet® 35 BC	IrO$_2$	2 M KHCO$_3$ or 2 M KOH	17	1	5	[2]
Verma 2016	Ag NP on Sigracet® 35 BC	IrO$_2$	1 M KHCO$_3$	17	2	10	[3]
Duarte 2019	Ag NP on Sigracet® 39 BC	platinized Ti	2 M KHCO$_3$	77	0.75	10	[4]
Jeanty 2018	Ag GDE Covestro	n.a.	0.4 M K$_2$SO$_4$	21	n.a.	7.67	[5]

References

(1)   Philips, M. F.; Davide, A.; Figueiredo, M. C.; Krasovic, J. WO2020165074A1, 2020.

(2)   Haas, T.; Krause, R.; Weber, R.; Demler, M.; Schmid, G. *Nat. Catal.* 2018, *1* (1), 32–39.

(3)   Verma, S.; Hamasaki, Y.; Kim, C.; Huang, W.; Lu, S.; Jhong, H. R. M.; Gewirth, A. A.; Fujigaya, T.; Nakashima, N.; Kenis, P. J. A. *ACS Energy Lett.* 2018, *3* (1), 193–198.

(4)   Verma, S.; Lu, X.; Ma, S.; Masel, R. I.; Kenis, P. J. A. *Phys. Chem. Chem. Phys.* 2016, *18* (10), 7075–7084.

(5)   Duarte, M.; De Mot, B.; Hereijgers, J.; Breugelmans, T. *ChemElectroChem* 2019, *6* (22), 5596–5602.

(6)   Jeanty, P.; Scherer, C.; Magori, E.; Wiesner-Fleischer, K.; Hinrichsen, O.; Fleischer, M. *J. CO2 Util.* 2018, *24* (March), 454–462.

H

Methods and supporting information to Chapter 12

I.1 Synthesis and characterization of gas diffusion electrodes

I.1.1 Nanoparticle synthesis

The procedure for preparing the gold nanoparticles was adapted from Kimling et al.[1] Gold nanoparticles supported on carbon were synthesized by dissolving 0.034 g of $HAuCl_4$ trihydrate (>49% Au, Fisher Scientific) in 95 mL of water and 0.097 g of trisodium citrate dihydrate (≥99%, Sigma-Aldrich) in 5 mL of water. The Au solution was brought to a boil under vigorous stirring, and the citrate solution was pre-heated. As soon as the gold solution boiled, the pre-heated 5 mL of citrate solution was added. Upon addition, the solution, which was initially yellow, turns transparent, then black and finally, after 15 min dark red. After the solution cooled down, still under vigorous stirring, an amount of VXC72 Vulcan carbon (Cabot) was added to yield a metal loading of 60% Au on the carbon support. The solution was then tip sonicated for 20 min at 31% amplitude with a MS73 ultrasonic probe (Bandelin) and kept stirring overnight. Once all the Au nanoparticles were supported on the carbon, the solution became transparent. The Au/C particles were filtered and rinsed several times with water.

I.1.2 Gas diffusion electrodes spraying

A catalyst ink stock solution was prepared by first adding 28.9 mg of Au/C nanoparticles to a solution containing 2.43 ml water and 2.43 ml ethanol to spray the 60% Au/C gold nanoparticles on carbon-based gas diffusion electrodes (GDEs). This mixture was tip sonicated for 5 min with a MS73 ultrasonic probe. Then 139 µL Nafion 5% solution (Sigma Aldrich) was added, and the ink was sonicated for another 5 min. For spraying, the ink was diluted 100 times with water. A gas diffusion layer (H23C2, Freudenberg) was cut to 4 x 10 cm sheets and used as substrate. The ink was deposited on the substrate using the spray-coating apparatus previously described.[2,3] The H23C2 substrates were placed on a heating block at 100 °C for quickly evaporating the solvent, hence reducing the possible formation of agglomerates. A template was used in order to limit the sprayed area to 1 x 3 cm. The spraying parameters were controlled with software written in Microsoft Visual Basic 6.0. The Au/C catalyst gradients were realized by adjusting the volume of ink dispensed along the substrate stepwise, using a defined array as a function of the XY position of the spray-tip. The total loading was determined by the number of times the procedure was repeated over the entire area of the

substrate. Fig. I.1 shows a photograph of one of the gas diffusion electrodes after spraying, indicating the Au/C nanoparticle gradient deposited in the exposed area.
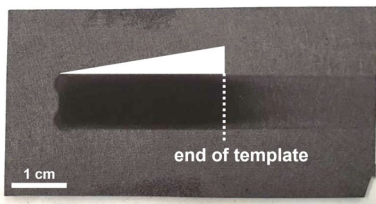

Fig. I.1. Photograph of the gas diffusion electrode after spraying showing a 1 x 3 cm^2 catalyst loading gradient.

I.1.3 Characterization of the gas diffusion electrodes

Scanning electron microscopy (SEM) and energy-dispersive X-ray spectroscopy (EDX) characterization of the GDEs and Au-nanoelectrode was performed using a Quanta 3D ESEM (FEI) at 20 kV acceleration voltage in high-vacuum mode. The Au-nanoelectrode was mounted on a customized metallic holder, and electric contact between the different samples and the metallic holder was established using a conductive carbon tape to minimize electrostatic charging. Focused ion beam (FIB) milling of the GDE substrate was performed for GDE-B to obtain a cross-sectional analysis of the pore structure. In the first step, the FIB milling process was used to mill a hole into the substrate from the top to create a ramp with a slope of approximately 45° using a FIB current of 65 nA for 2 h. This is a prerequisite for EDX analysis of the cross-sectional view later. In a 90° angle to this cut, another ramp with a 45° slope was milled into the substrate using the same parameters. The sample was then tilted by 2°, and a FIB cross-section polishing procedure was applied for about 10 min to obtain the shown cross-sectional view inside the substrate. EDX of the exposed cross-section after FIB milling was conducted at an acceleration voltage of 30 kV.

I.1.4 Au-nanoelectrode preparation

Au-nanoelectrodes suitable for the approach via shear-force based distance feedback were fabricated with a laser puller (Model 2000, Sutter Instruments). As already mentioned in the main text, the adhesion properties of untreated gold wires to the capillary glass walls are not sufficient for the reliable production of well-sealed Au SECM tips. Therefore, we modified the adhesion characteristics of the gold wire (50 μm diameter, >99.99 %, Goodfellow) by electrochemically coating it

with a thin layer of platinum. Platinum deposition was performed in a 3-electrode electrochemical setup with the Au wire as working electrode, a Pt mesh as counter electrode, and a Ag/AgCl/3 M KCl as reference electrode. A commercial Pt plating solution (Met-Pt 209, Metalor) was used as electrolyte. Contact with the electrolyte was made with the gold wire at 0 V, and then three potential pulses of 100 ms to −1 V and 500 ms to 0 V were performed. The coated Au-wire was further immersed into the plating solution for 2 h without any applied bias voltage, and then thoroughly rinsed with water. Once dried at ambient atmosphere, 1 cm long pieces of Pt-plated gold wire were positioned in the centre of soda-lime glass capillaries (Hilgenberg) with an inner diameter of 0.5 mm and an outer diameter of 1 mm. Next, the filled glass capillaries were fixed in a laser puller. Both capillary inlets were connected to a vacuum pump (Laboport, KNF Neuberger) to avoid the inclusion of air bubbles during the subsequent sealing step. During sealing of the Au wire in 7-9 heating/cooling cycles (20 s and 40 s, laser ON/OFF), the puller bars were fixed with a metal clamp to prevent a continuous pulling force on the capillary. The following laser puller parameters were used during the sealing step: heat: 260; filament: 5; velocity: 90; delay: 140; pull: 0. After confirming a visually complete Au/glass seal with the help of an optical microscope, the capillary was reinserted into the laser puller for the hard pull step. In this step, the Au/glass composite was liquified by laser heating and pulled into two parts using the following parameter set: heat: 300; filament: 5; velocity: 90; delay: 140; pull: 90-110. The resulting long-tapered glass/Au tips were electrically contacted by conductive 2-component epoxy glue (Polytec EC 151-L, Polytec PT). The glue was filled into the glass capillary using the tip of a Cu-wire (outer diameter of 0.3 mm) up to the non-sealed section of the Au wire. One end of the Cu wire was left inside the filled capillary while curing the glue at 90 °C for 1 h. The tip was polished in a homemade polishing setup which individually rotates the electrode and a hard disc covered with an abrasive film to expose the cross-section of the gold wire. The tip was also subsequently polished on the following abrasive layers: P2000 sandpaper (Starcke), 0.5 µm and 0.1 µm diamond lapping film (661X, 3M Deutschland). Prior to polishing on each lapping film, the Au tip was ultrasonicated in EtOH/water for 10 min.

I.1.5 Shear-force based approach

The local detection of CO during CO_2 reduction over gold GDEs requires approaching the Au-nanoelectrodes to a sub-µm distance from the substrate. Such precise positioning is done by shear-force distance-controlled scanning

electrochemical microscopy (SECM). Its approach feedback mechanism is based on short-range hydrodynamic forces, which occur in the order of a few 100 nm away from solid surfaces.[4] During the approach of a resonantly oscillating SECM tip towards a solid surface, those forces modulate the tip´s oscillation characteristics, which serve as feedback for determining the absolute surface position. To assure a successful approach, all setup components are located inside of a homemade faraday cage to allow for shielding of electrical noise, with the exception of the lock-in amplifier and the potentiostat. Vacuumed polystyrene panels (Vaku-Isotherm) are used to cover the inner walls of the faraday cage to maintain a constant temperature around the measurement cell. Vibrational noise during SECM measurements was minimized by mounting the faraday cage on an actively damped table (Newport RS 2000). The precise approach of the Au-nanoelectrode towards different spots of the GDE surface was facilitated by a positioning system combining both a stepper motor and a piezo positioning unit. A coarse alignment of the SECM tip in the X, Y and Z coordinates was established via stepper motor (OWIS) controlled µm-screws. The pre-approach in the Z-direction was visually controlled with the help of a video microscope (monochrome USB camera, The ImagingSource). After the pre-approach, a piezo positioning unit (PI) enabled further approach in nanometer increments. In parallel to the approach, the oscillation magnitude of the resonantly vibrating Au tip was recorded as feedback signal. Such shear-force-based distance control loops require mounting two piezo elements (Piezomechanik Pickelmann) to the Au tip glass body. Both piezo elements were connected to a lock-in amplifier (Ametek 7280) via BNC connectors. One of those piezo elements served as the detection element for the magnitude of the oscillation at the tip apex and was mounted as close as possible to the tip´s taper. The second piezo unit had the function to generate a tip oscillation at a defined frequency by applying an AC voltage via the lock-in amplifier. This excitation piezo was mounted in a distance of 1-1.5 cm above the detection piezo and was displaced by an angle of around 45°. To establish a reliable distance control, it is crucial to identify a tip resonance frequency with high sensitivity towards the tip-to-surface distance. For that purpose, before every experiment, a frequency spectrum in the range from 200-500 kHz (linear ramp over 300 s, 200 mV magnitude) was recorded while the tip was kept in the pre-approach position above the GDE substrate. Subsequently, electrolyte (1 M $KHCO_3$) was filled into the electrochemical cell, so that the Au tip got immersed into this differently oscillating medium. Another frequency spectrum was then recorded and compared to the one

in air. Resonant frequencies with significantly different oscillation magnitudes in both scans indicate possible tip frequencies for the shear-force based approach, since only resonant frequencies originating from the tip, and not from other system components such as the electrode holder, are altered by a change of the oscillation medium. Once a stable tip resonance frequency is identified, it is constantly set at the excitation piezo. During that defined oscillation, the tip is approached in nanometer increments towards the surface while continually monitoring the oscillation magnitude. The approach is automatically terminated once a magnitude change of 3 % of the lock-in value is detected by the software. This rapid change in magnitude is a characteristic feature in the approach curve, demonstrating that the tip reached a distance within the shear-force interaction region (in the order of 100 nm from the sample surface).

I.2   SECM experiments

SECM experiments using the shear-force approach method were performed in an electrochemical cell made of polyetheretherketon (PEEK) as shown in Fig. I.2. The GDE substrate was mounted between the electrolyte compartment (upper part of the cell) and a gas compartment with the help of an O-ring. The GDE was electrically contacted using Cu tape which was fixed along all GDE edges to minimize the electrical resistance. The gas compartment was connected to gas inlet and outlet Swagelok connectors allowing for a flow of gaseous CO_2 towards the GDE backside during the experiment. The flow rate of CO_2 into the gas compartment was controlled via a GFC17 mass flow controller (Aalborg). The gas outlet was fed via a tube into a water-filled glass column in order to adjust the GDE backpressure (overpressure with respect to atmosphere) via the immersion depth of that tube. Electrochemical measurements were conducted using an analogue bi-potentiostat (IPS PG 100, IPS Peter Schrems) which was controlled by an in-house software. The GDE substrate and SECM tip were connected as working electrodes 1 and 2, as indicated in Fig. I.2 by WE1 and WE2, respectively. The counter electrode (CE) was constructed from two dimensionally stable anodes (48 x 10 x 1 mm, MMO Type 197, Umicore), which were placed at two opposite edges of the electrolyte reservoir by means of a Au wire ring. The reference electrode (RE) was a homemade Ag/AgCl/3 M KCl with the filling solution reservoir separated from the electrolyte via a ceramic frit. The Ag-wire (99.995 %, ChemPur) was electrochemically coated with AgCl from a 3 M KCl solution (VWR Chemicals) containing 0.1 M HCl (Sigma

Aldrich) solution applying 5 V for 1 min and 10 V for 10 min vs. a Pt counter electrode. A fresh 1 M $KHCO_3$ electrolyte solution (99.7 %, Sigma-Aldrich) was used for each measurement, and was cleaned from metal cation impurities prior to use with the help of a Chelex-100 (Bio-Rad) resin as reported elsewhere.[5] For each SECM experiment, the CO_2 flow was switched on after filling the electrolyte (prior to the frequency scan in liquid) to prevent gas from breaking through dry GDE pores. After finding a suitable tip resonance frequency, the tip was positioned in the low loading region of the GDE (next to the left edge of the spraying template, Fig. I.1). After ensuring the tip functionality within the shear-force interaction region by cyclic voltammetry (example in Fig. I.7), an array scan along the first 1.7 cm of the sprayed Au/C loading gradient was performed in hopping mode. At each X-Y coordinate of that scan, a shear-force based approach was performed to account for topological differences along the gradient towards higher catalyst loadings, with the substrate held at –0.6 V. Once the distance feedback criterion was met, different potentials were subsequently applied to the GDE for 60 s while recording both the GDE and Au tip current. After the final potential was applied, the GDE was held again at –0.6 V, and the Au tip was retracted by 100 µm before moving to the next X-Y position of the GDE to avoid collision with surface features.

I.3 Characterization of the gas diffusion electrodes

The volume of ink dispensed using the spray-coater along the substrate is shown in Fig. I.3 for GDE-A (shallow catalyst gradient) and GDE-B (steep catalyst gradient). SECM measurements were performed along 1.7 cm of the substrates, corresponding approximately to the area highlighted in yellow in Fig. I.3. The two GDEs were characterized by SEM and EDX at different X-positions along the Au/C catalyst gradient. Results are shown in Fig. I.4 and Fig. I.5, for GDE-A and GDE-B, respectively.
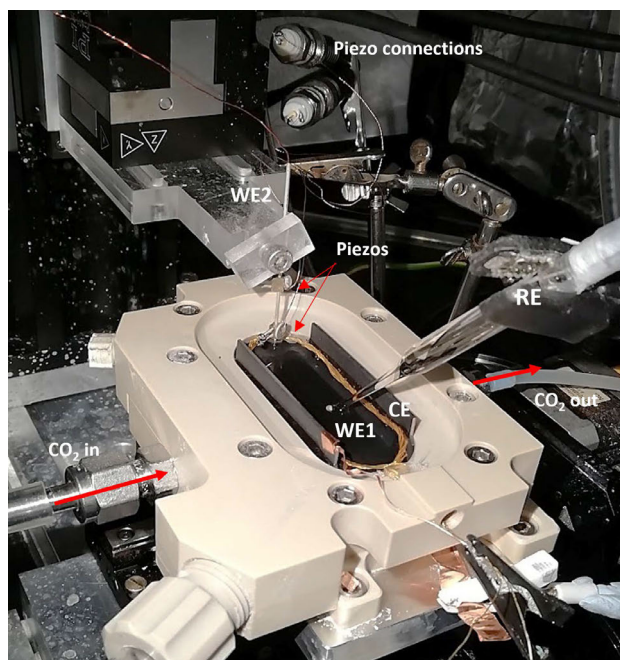
Fig. I.2. Electrochemical cell mounted in the SECM setup. The GDE substrate and the Au nanoelectrode are indicated as WE1 and WE2, together with the Ag/AgCl reference electrode (RE) and the DSA counter electrode (CE). The piezo elements and connectors are also indicated in the image, as well as the CO_2 gas inlet and outlet.
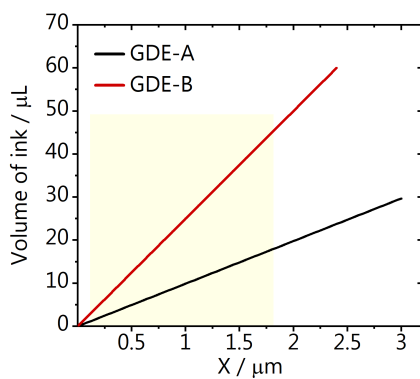

Fig. I.3. Volume of ink dispensed along the gas diffusion layer creating a more (GDE-B) or less (GDE-A) steep catalyst gradient.
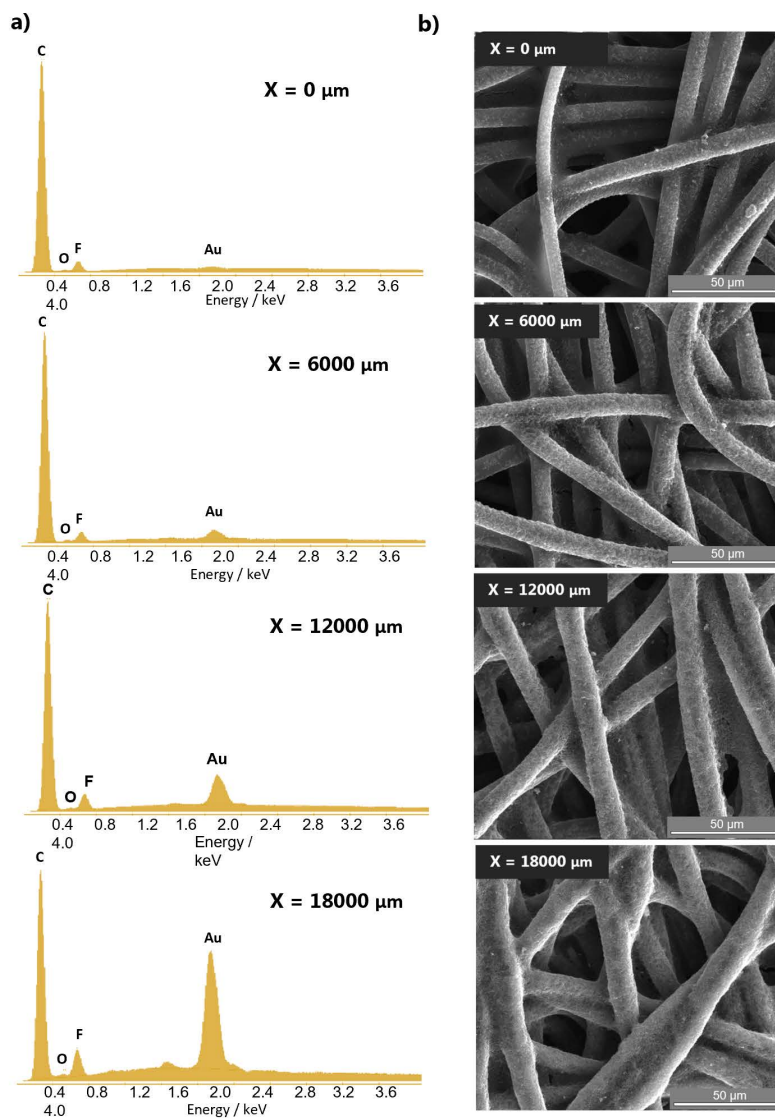
Fig. I.4. a) EDX spectra and **b)** SEM micrographs obtained at different X-positions along the catalyst gradient of GDE-A.
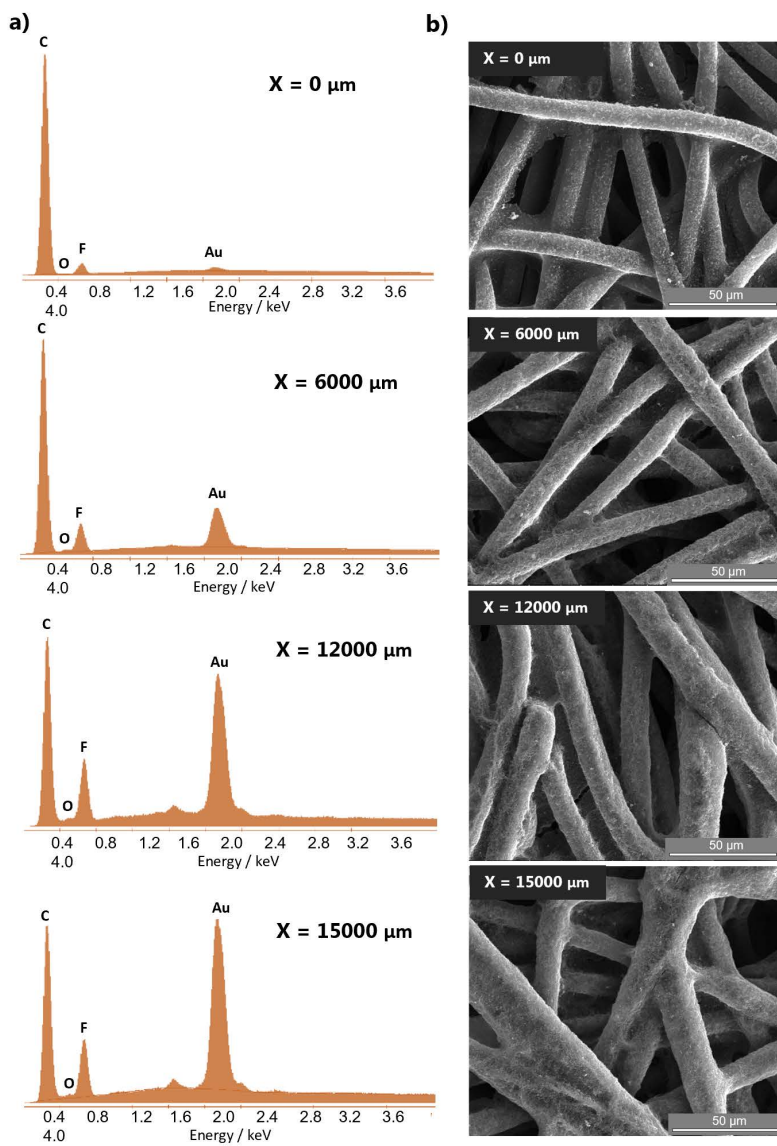
Fig. I.5. a) EDX spectra and **b)** SEM micrographs obtained at different X-positions along the catalyst gradient of GDE-B.

I.4   Shear-force approach

For positioning of the tip above the gas diffusion electrodes, first, a frequency spectrum of the gold nanoelectrode (Fig. I.6a) is recorded in air and then in electrolyte in order to determine the resonance frequencies characteristic from the tip. Using one of these frequencies, e.g. shown in Fig. I.6b (and marked in yellow in Fig. I.6a), an approach curve (Fig. I.6c) is performed to place the tip ~100 nm from the surface. Approach curves were performed at every XY position of the substrates before the measurements.
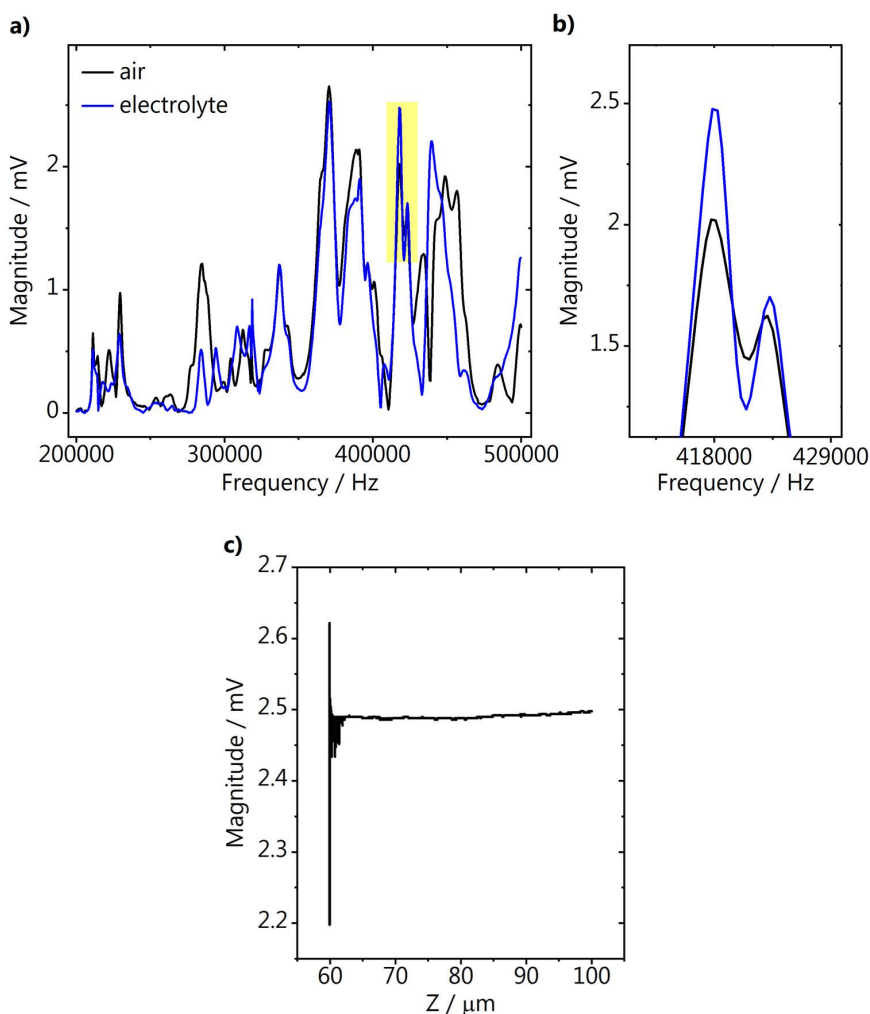
Fig. I.6. a) Frequency spectra recorded in air and electrolyte, **b)** zoom in of the tip resonance frequency used for the approach curve (yellow area from a)), **c)** approach curve.

I.5   Gold nanoelectrode response

The blank voltammetry of the gold nanoelectrode was recorded in the shear-force interaction region (~100 nm from the surface) before each measurement to assure a clean and reproducible Au surface. An example of a blank CV is shown in Fig. I.7a. CVs were also recorded while applying different potentials to the bare gas diffusion layer (without catalyst) in CO_2 saturated electrolyte (Fig. I.7b). No CO is produced by the bare substrate, and a reproducible double layer charging current is observed between 0 and 0.55 V vs Ag/AgCl.
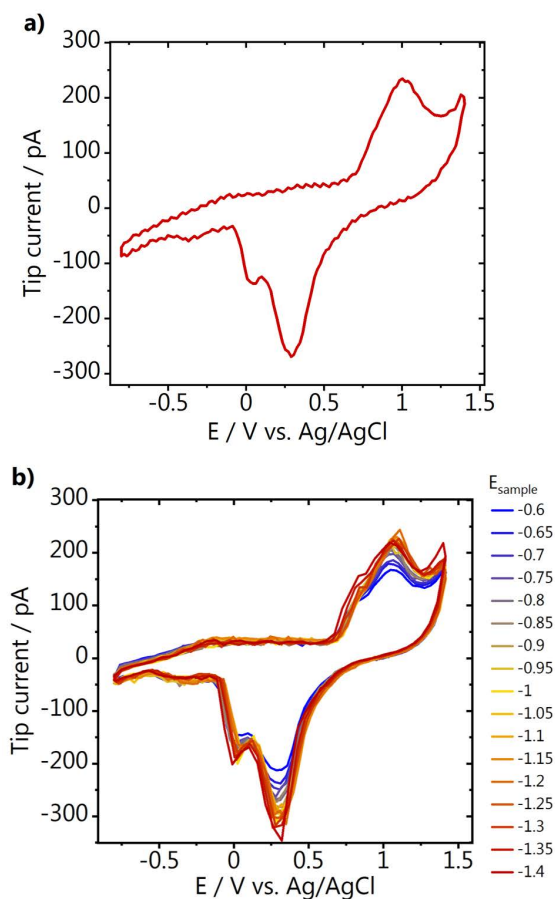
Fig. I.7. a) Blank CV of the gold nanoelectrode and b) voltammetry recorded in the shear-force interaction region while stepping the GDE potential. The sample potentials reported (E_{sample}) are versus Ag/AgCl, and the CVs were recorded in 1 M $KHCO_3$, CO_2 saturated, at 200 mV s^{-1}.

The gold nanoelectrode CVs were also recorded after flowing a calibration gas containing 1% CO for 10 seconds through the cell (Fig. I.8a). Two characteristic plateaus show the diffusion-limited oxidation of CO.[6] Additionally, voltammetric features of the gold oxidation and the overpotential of the oxygen evolution reaction (OER) can be observed. In Fig. I.8b, the voltammetric response of the Au nanoelectrode is shown while different potentials were applied to the gas diffusion electrode.
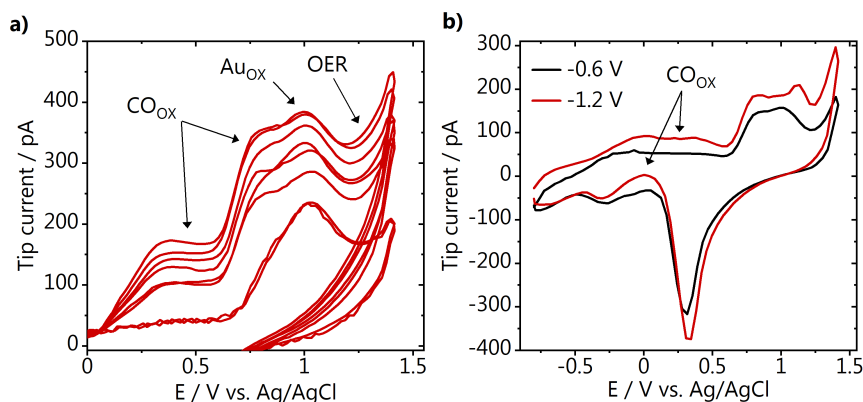

Fig. I.8. CVs of the gold nanoelectrode **a)** after feeding a calibration gas containing 1 % CO though the substrate for 10 s and **b)** upon applying different potentials to the GDE. The sample potentials reported are versus Ag/AgCl, and the CVs were recorded in 1 M $KHCO_3$, CO_2 saturated, at 200 mV s^{-1}.

I.6   SECM array scans

An example of how bubbles affect the current measured at the gold nanoelectrode is shown in Fig. I.9, where the sample (GDE-A) was held at –1.15 V vs. Ag/AgCl.
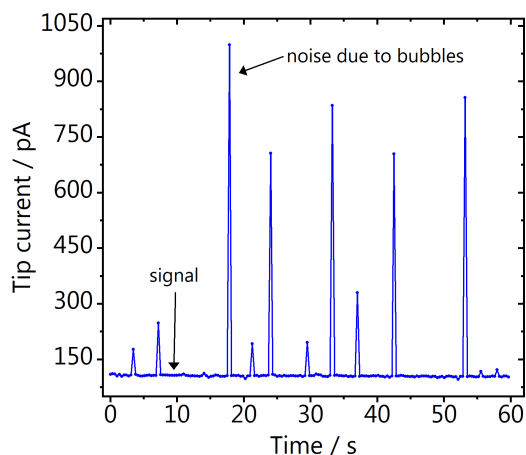
Fig. I.9. Raw tip current data recorded during a measurement where GDE-A was held at –1.15 V vs. Ag/AgCl.

The activity of GDE-A along the catalyst gradient is shown in Fig. I.10. The experiment was performed in 1 M KHCO$_3$ with a CO$_2$ pressure of 2 mbar.
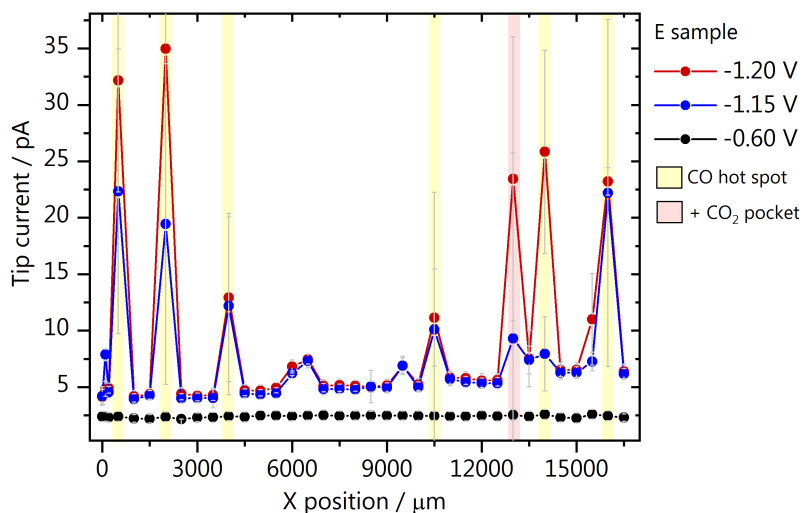

Fig. I.10. SECM array scan of GDE-A in 1 M KHCO$_3$ at a CO$_2$ pressure of 2 mbar. Potentials are reported versus Ag/AgCl.

Fig. I.11 shows the correlation between the sample height profile and the amount of CO detected along the gradient of GDE-B, at a CO_2 pressure of 0.7 mbar.
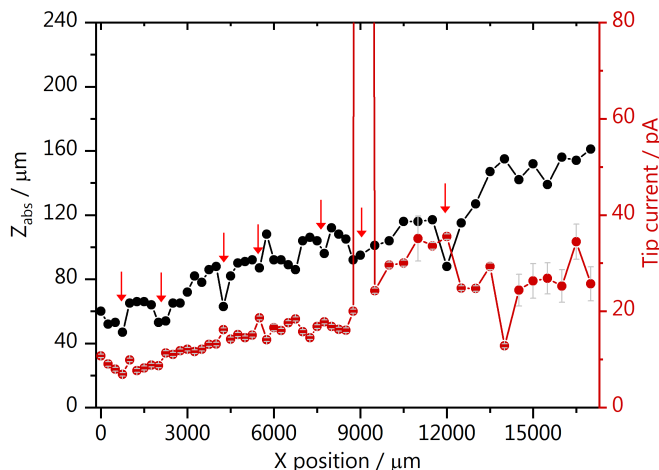

Fig. I.11. Absolute position of the shear force interaction region along the catalyst gradient of GDE-B, together with the CO activity.

Fig. I.12 presents the activity maps recorded in a 30 x 30 μm area of GDE-B (CO_2 pressure 0.7 mbar). Here, three different ways of visualizing the same data are presented for the three different substrate potentials applied. The top panel shows a realistic representation of the data measured, considering the diameter of the Au nanoelectrode, and the middle panel the same data but with the space filled. The interpolated data (using nearest neighbours) are shown in the lowest panel and allows for easier visualization and interpretation of the activity trends and is therefore shown in the main text.

After recording the activity maps, we have marked the substrate using a 1.2 mm probe at a distance of 1 mm of the scanned area, as shown in the SEM micrograph in Fig. I.13a. Although there is an uncertainty in the exact location of the map, Fig. I.13b shows that the mapped region likely has large variations in topography, i.e. deep pores and fibres at different levels. Taking this into consideration together with the results shown in Fig. I.11, we are confident that the mapped area is likely the region shown in Fig. I.13c.
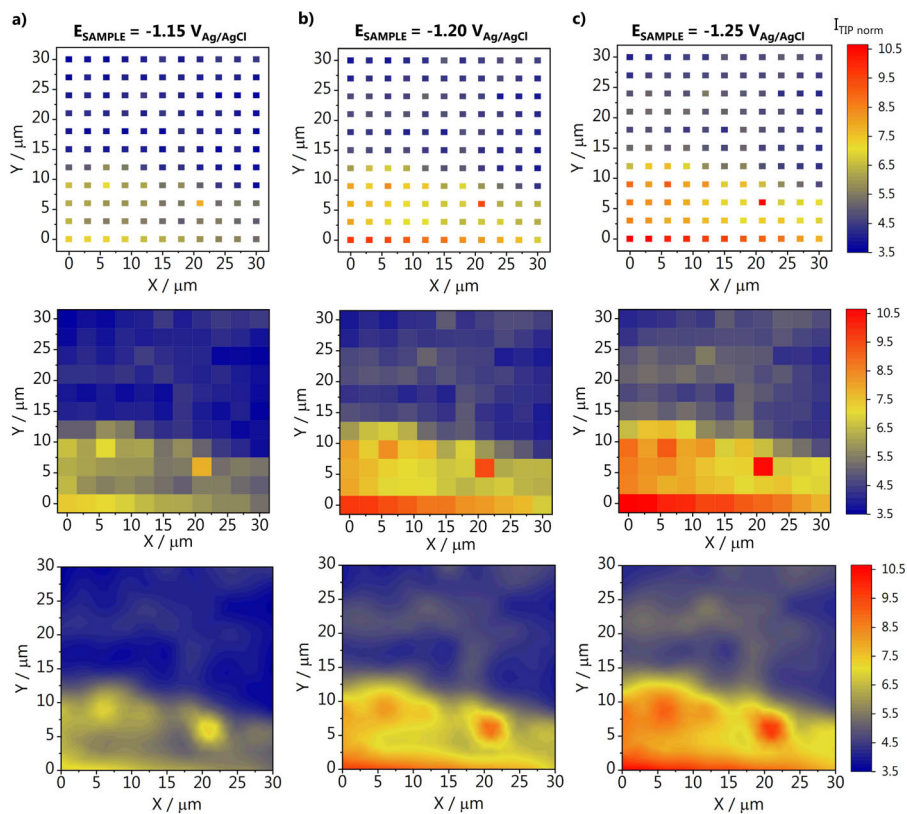
Fig. I.12. Activity map of GDE-B recorded at sample potential **a)** -1.15 V, **b)** -1.2 V and **c)** -1.25 V. Three different ways of visualizing the data are presented, namely by plotting the individual data points with and without space filling, and the interpolated data shown in the main text. Potentials are reported versus Ag/AgCl.
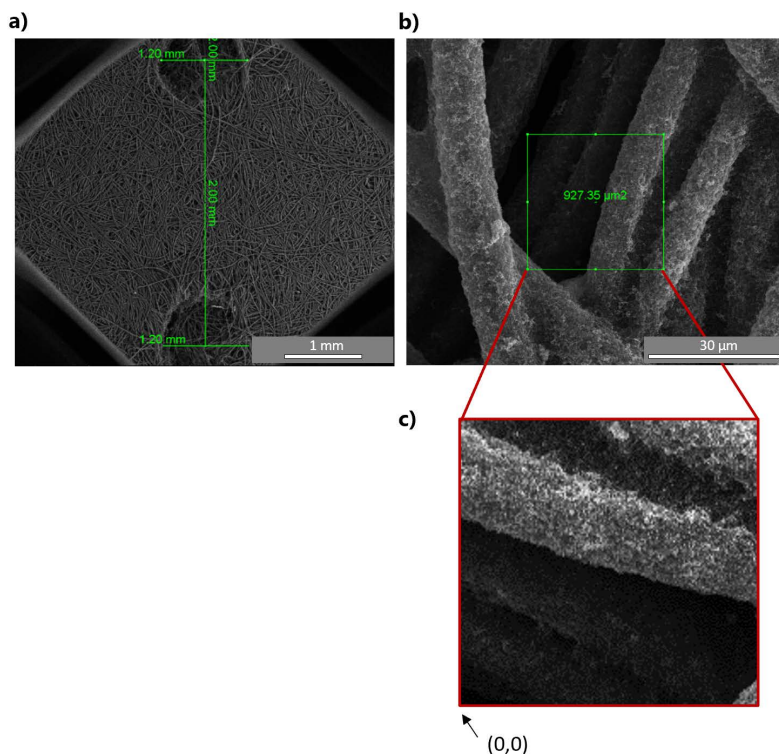
Fig. I.13. SEM micrographs of **a)** the marks made in GDE-B after the activity maps were recorded, **b)** the mapped region, within a confidence interval and **c)** a suggested topography of the mapped area.

References

(1)   Kimling, J.; Maier, M.; Okenve, B.; Kotaidis, V.; Ballot, H.; Plech, A. *J. Phys. Chem. B* 2006, *110* (32), 15700–15707.

(2)   Junqueira, J. R. C.; Bobrowski, T.; Krysiak, O. A.; Gutkowski, R.; Schuhmann, W. *ChemCatChem* 2019, *11* (24), 6417–6424.

(3)   Bobrowski, T.; Conzuelo, F.; Ruff, A.; Hartmann, V.; Frank, A.; Erichsen, T.; Nowaczyk, M. M.; Schuhmann, W. *Chempluschem* 2020, *85* (7), 1396–1400.

(4)   Nebel, M.; Eckhard, K.; Erichsen, T.; Schulte, A.; Schuhmann, W. *Anal. Chem.* 2010, *82* (18), 7842–7848.

(5)   Wuttig, A.; Surendranath, Y. *ACS Catal.* 2015, *5* (7), 4479–4484.

(6)   Monteiro, M. C. O.; Jacobse, L.; Koper, M. T. M. *J. Phys. Chem. Lett.* 2020, *11* (22), 9708–9713.